UiT
THE ARCTIC
UNIVERSITY
OF NORWAY

Faculty of Science and Technology
Department of Physics and Technology

In-situ Measurements of Mesospheric Aerosols

On the observable characteristics of nanoscale ice and meteoric smoke particles

—

Tarjei Antonsen

A dissertation for the degree of Philosophiae Doctor – October 2018

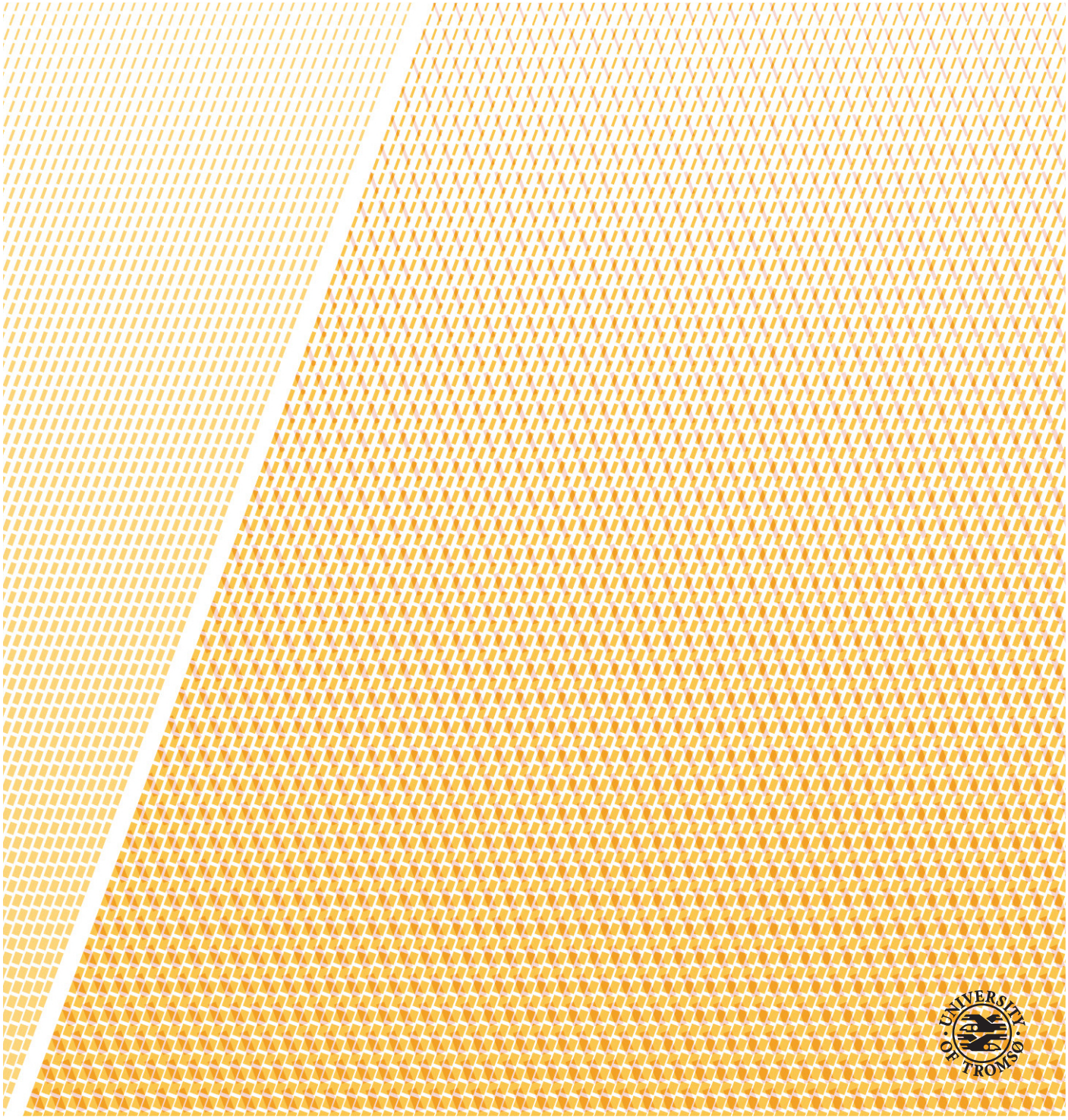

Abstract

Two sounding rocket payloads were launched from Andøya Space Centre (69.29°N, 16.02°E) during the summer of 2016 within the MAXIDUSTY campaign. Their payloads contained instrumentation aimed at investigating the characteristics of nanoscale aerosols in the upper summer mesosphere, and the role of these particles in phenomena like noctilucent clouds and polar mesospheric summer echoes (PMSE). The mesopause region, situated between $\sim$ 80 and 90 km, contain a variety of different particle types such as ice particles, meteoric smoke particles (MSPs) and hybrids of these. The role of such particles in a number of processes in the mesopause and further down in the atmosphere is not well understood. This work aims to close some of the gaps in our current understanding mainly by using aerosol detectors of the Faraday cup type. For this purpose, we have developed new observational techniques using such probes, which makes it possible to obtain information on intrinsic particle properties such as charge state, size and number density of both ice and MSPs. The configuration and technical capabilities of the probes on MAXIDUSTY also allows for observation of spatial structures in the dusty plasma down to scales of $\sim$ 10 cm. Notably, we are able to calculate the size distribution and charge state of ice particles on scales well below 1 metre. With the impact probe MUDD, we are able to infer the size distribution and volume content of MSPs embedded in larger ice particles. We moreover present the first observations of mesospheric clouds situated well below the summer mesopause, at altitudes between 66 and 78 km, which implies a significant updraft in this region. From a thorough investigation into spatial fluctuations on different length scales, we find that the aerosol-electron coupling is changing throughout a cloud system and not strictly anti-correlated. We also find that a simple relationship between PMSE and dusty plasma parameters is not possible to obtain from MAXIDUSTY measurements.

Sammendrag

To sonderaketter ble skutt opp fra Andøya Space Center (69.29˚N, 16.02˚E) under MAXIDUSTY-kampanjen sommeren 2016. Deres nyttelaster inneholdt instrumentering med mål om å undersøke karakteristika av nanoskala aerosoler i den øvre mesosfære, og rollen til disse partiklene i fenomener som nattlysende skyer og polare sommer-mesosfæriske ekko (PMSE). Mesopausen, lokalisert i høydeområdet $\sim$ 80 til 90 km, inneholder mange forskjellige partikkeltyper som ispartikler, meteoriske røykpartikler (MSP) og hybrider av disse. Rollen til slike partikler i mange prosesser i den øvre atmosfære er ikke godt forstått. Dette arbeidet sikter på å besvare noen av de ubesvarte spørsmål om mesosfæriske aerosoler ved å hovedsaklig bruke såkalte Faraday-bøtter. Vi har utviklet nye observasjonsteknikker for slike prober som gjør det mulig å få informasjon om egenskaper som ladning, størrelse og nummertetthet til både is og MSP. Konfigurasjonen og de tekniske egenskapene til probene på MAXIDUSTY-nyttelastene gjør det også mulig å måle romlige fluktuasjoner i støvplasmaet på skalaer ned til $\sim$ 10 cm. Spesielt nevnes at vi har målt størrelsesfordelingen og ladningstilstanden til ispartikler på skalaer vel under 1 meter. Med proben MUDD kan vi estimere strørrelsesfordelingen til MSPer som er innevokst i større ispartikler. Vi presenterer den første observasjonen av mesosfæriske skyer vel under mesopausehøyder i sommermesosfæren – mellom 66 og 78 km. Dette implisererer en signifikant oppdrift i denne regionen. Fra en undersøkelse av fluktuasjoner på forskjellige lengdeskalaer, finner vi at aerosol-elektron-koplingen endrer seg gjennom et skylag og ikke strengt anti-korrelert. Vi finner også at et enkelt forhold mellom PMSE og støvplasmaparametere ikke er mulig å finne fra målingene gjort under MAXIDUSTY.

Contents

Preface

It was during the time I wandered about and starved in Tromsø: Tromsø, this singular city, from which no man departs without carrying away the traces of his sojourn there.

As a fresh physics student in Paris of the North[1], my impression of the space related research conducted at the Univeristy was that radars were the big thing; Auroras, ionospheric processes and all that jazz. I remember reading about rocket experiments in an old brochure about UiT while I was in high school, and it was perhaps the main reason I chose to study space physics there. In spite of this, I knew little about the rocket related activities at UiT during my first three years in Tromsø.

In conjunction with a course in remote sensing on Andøya Rocket Range, I came in contact with Dr. Alexander Biebricher at NAROM. He was a former PhD fellow under Prof. Ove Havnes, working mainly with radar phenomena in the mesosphere. I told him about my fascination with rockets, and he brought me into contact with Prof. Havnes. At that time and as is still the case, the rocket group in Tromsø was small, with two engineers doing the work of ten men. The MAXIDUSTY project had started some time before, but a reasonable deal of work still remained: for example regarding the testing of instruments in vacuum. I was warmly welcomed into the group, and worked with vacuum testing under Prof. Åshild Fredriksen. I was lucky enough to continue some of the work I had started on during my Master's work in a PhD fellowship. The culmination was the MAXIDUSTY launch during the summer of 2016.

During the last four years I have been working with many different aspects of the MAXIDUSTY rocket campaign. This involvement, together with excellent follow-up and a good relationship with my supervisors, I feel have given me a wider set of skills than I could have hoped for going into the project; I now feel in some ways like a scientific mongrel, which is a good thing.

[1] As I am not a local, I agree this is an absurd name for Tromsø.

I do not really know what a good preface is, in fact, I just learned from my British colleague that I have been pronouncing it wrong for years. I would imagine such a text should have an underlying message or a good advice. I don't know if I can live up to that anticipation, but while I have your attention;

To the person who has stolen all my good pens the last three years: Please return them, those are expensive pens. I hope you have enjoyed pen heaven.

Overview of this thesis

Chapter 1 provides a brief history of sounding rockets, and how mesospheric rocket soundings have developed into how we currently carry out in-situ measurements of the upper mesosphere. It also describes the scientific motivation for the MAXIDUSTY project. Chapter 2 presents an introduction into the general characteristics of the mesosphere and nanoscale ice and meteoric smoke particles residing in the upper mesosphere. In Chapter 3 we introduce the theory behind modelling the movement of nanoparticles around rocket probes, and discuss the interaction of aerosols with rocket probes. Concepts such as secondary charging and adverse effects for detection are introduced. The MAXIDUSTY campaign and payloads are introduced in Chapter 4. Special emphasis is put on the probes built at UiT, which the author has worked with. The Faraday cups introduced there constitute the main framework for the included publications in the thesis. Chapter 5 presents the topic of sizes of mesospheric ice and meteoric smoke, as this is the main focus in Papers II and IV. In Chapter 6 we present the concept of multi-scale measurements of dusty plasma, and how it can be used to resolve certain open questions regarding mesospheric aerosols. A list of abbreviations is included as an appendix.

The thesis includes five papers, of which three are published in peer-reviewed journals and two are currently under revision in a peer-reviewed journal. The papers are shortly summarized in the following.

The developmental work and testing done during MAXIDUSTY constitutes a large part of the PhD work, which is not elaborated on in the thesis introduction. Chapter 6 includes a description of the ICON instrument, which represents a large part of the developmental efforts by the author.

Tarjei Antonsen, Tromsø, 2018

List of papers

This thesis consists of a subject introduction, an overview of the MAXIDUSTY campaign and the UiT instruments on the MAXIDUSTY payloads and the following peer-reviewed papers:

I Antonsen, T. and Havnes, O. (2015) *On the detection of mesospheric meteoric smoke particles embedded in noctilucent cloud particles with rocket-borne dust probes*, Review of Scientific Instruments, **86**(3), 033305, 1–12, March 2015.
doi: 10.1063/1.491439.

II Antonsen, T., Havnes, O. and Mann, I. (2017), *Estimates of the Size Distribution of Meteoric Smoke Particles From Rocket-Borne Impact Probes*, Journal of Geophysical Research: Atmospheres, **122**, 12353–12365, November 2017.
doi:10.1002/2017JD027220.

III Antonsen, T., Havnes, O. and Spicher, A. (2018), *Multi-scale Measurements of Mesospheric Aerosols and Electrons During the MAXIDUSTY Campaign*, Atmospheric Measurement Techniques, **In Review**, 1–12, June 2018.
doi:–.

IV Havnes, O., Antonsen, T., Baumgarten, G., Hartquist, T., Biebricher, A., Fredriksen, Å., Friedrich, M., and Hedin, J. (2018), *A new method to inference the size, number density, and charge of mesospheric dust from its in situ collection by the DUSTY probe*, Atmospheric Measurement Techniques, **In Review**, 1–12, June 2018.
doi:–.

V Havnes., O., Latteck, R., Hartquist, T., and Antonsen, T., (2018), *First simultaneous rocket and radar detections of rare low summer mesospheric clouds*, Geophysical Research Letters, **45**(11), 5727–5734, May 2018.
doi:10.1029/2018GL078218.

Short Summaries and Author Contributions

Paper I The paper presents the MUDD probe as it was launched on the PHOCUS payload (see also Havnes et al. (2014)), and finds that meteoric smoke particles (MSPs) which are embedded in mesospheric ice particles can be detected, and their size distribution inferred, with modified Faraday Cups. The paper, containing extensions and improvements of initial simulations done during work presented in Antonsens Master's Thesis "*On the internal physical conditions in dust probes: transport, heating and evaporation of fragmented dust particles*" (2013), was decisive in the process of the implementation of MUDD on MAXIDUSTY. Furthermore, the paper introduces a method to determine the dynamics of nanoscale particles in the vicinity of rocket probes which can be generalized to a number of different geometries, particle types and ambient conditions. A key result is that the current of fragments of large $\gtrsim$ 10 nm ice particles is probably dominated by pure MSPs, which implies that Faraday cups can measure the size distribution of these embedded particles. The theory was extended for use in mesospheric rocket studies by Antonsen and Havnes and the original MUDD design is by Havnes. All simulations were run by Antonsen, who also wrote the dust transport code. The manuscript was in its entirety prepared by Antonsen with contributions from Havnes.

Paper II This work presents an analysis of the measurements carried out by two triplets of MUDD probes on the MXD-1 and MXD-1B payloads launched in June and July of 2016, respectively. The data is analysed on the basis of the theoretical findings from Paper I and consists of MUDD data from 10 unique biased channels – from which one is able to infer 10-point energy distributions of dust fragments/MSPs. The main finding is that fragments of large ice particles, whos currents are presumably dominated by pure MSPs, follow an inverse power law which is slightly steeper than theoretical distributions (see e.g. Megner et al. (2006); Bardeen et al. (2008); Hunten et al. (1980)). Moreover, it is found that the meteoric content inside the ice is of the order of up to a few percent by volume, confirming earlier results (Hervig et al., 2012; Havnes et al., 2014). The manuscript was prepared in its entirety by Antonsen with contributions from co-authors.

Paper III In this work, we have analysed in-situ measurements of mesospheric aerosols and electrons during the MAXIDUSTY campaign, with special emphasis on the second flight, MXD-1B, where highly interesting features

were encountered. The in-situ data comes from the DUSTY and MUDD Faraday cups and the multi-Needle Langmuir Probe built by the University of Oslo. One key result is that two mechanically and electronically identical DUSTY probes with an interspacing of $\sim$ 10 cm detected very different currents through parts of a cloud system, which we attribute to aerodynamic modulation of small aerosols. We also conduct a spectral analysis, and discuss shortly the relationship between the frequency spectra of aerosol fluctuations and PMSE. From this discussion, we find it difficult to conclude with a simple relationship, and moreover find that a simple proxy from a linear combination of dusty plasma parameters is hard to obtain. The manuscript was prepared in its entirety by Antonsen with contributions from co-authors.

Paper IV In this study we present a new extended method of analyzing measurements of mesospheric dust made with DUSTY Faraday cup probes. With this method, the variation of fundamental dust parameters through a mesospheric cloud – such as size, charge state and number density – with an altitude resolution down to 10 cm or less can be obtained. We extend the analysis of DUSTY data by using the impact currents on its main grid and the bottom plate as in earlier works, in combination with a dust charging model and a secondary charge production model. The method is furthermore used on the MAXIDUSTY Faraday cup measurements and compared to remote (lidar) and in-situ (photometer) data. The conclusion is that the introduced method can be utilized as a powerful tool to determinine the size and charge state of dust particles, with good accuracy and high resolution. Havnes, Biebricher, Antonsen and Hartquist extended the theory for analyzing the rocket data. Havnes and Antonsen analyzed the rocket data. Baumgarten and Hedin collected and analyzed the optical data. Antonsen and Fredriksen tested the rocket instruments. Friedrich analyzed the Faraday data and provided the electron density data. Havnes prepared the manuscript with contributions from all co-authors.

Paper V This paper confirms that weak dust clouds at altitudes lower than the mesopause altitudes can occur and be sustained for longer times in the polar summer. Due to lack of observational evidence and holes in the theoretical understanding, such clouds were difficult to justify earlier. However, with more powerful radars (i.e. MAARSY close to the Andøya rocket range) and sensitive in-situ probes, the detection of very tenuous and low dust clouds is now confirmed to be possible. Paper V presents the first si-

multaneous rocket and radar observation of such low altitude dust clouds – observed between 66 and 78 km during the MAXIDUSTY campaign – which we have termed *Rare Low Summer Echoes*. The features were encountered during the MXD-1 flight, and we find that the presence of relatively large dust at low altitudes is consistent with smaller MSPs being swept out of the low mesospheric cloud region during the summer, while larger MSPs remain where their fall velocities equals the circulation updraught velocities. The rocket data was obtained and analysed by Havnes and Antonsen. Remote measurements were analysed by Latteck. The preparation of the manuscript was prepared by Havnes and Hartquist with contribution from the other authors.

In the text, these papers will be referred to by their Roman numerals.

Acknowledgements

This thesis was completed at UiT - The Arctic University of Norway under the supervision of Åshild Fredriksen (main supervisor), Ove Havnes and Björn Gustavsson. I am very grateful for their support, which have been impeccably great. I must also direct a sincere thank you to group leader Ingrid Mann, who have reviewed much of my work related to this thesis and its papers and moreover helped me through good discussions.

Ove Havnes deserves a special thank you for including me so selflessly and deeply into his work, even as a helpless Master's student. Thank you for the good conversations about physics and all other miscellaneous topics.

The MAXIDUSTY rocket campaign and the construction of the rocket instrumentation was supported by grants from the Norwegian Space Centre (VIT.04.14.7, VIT.02.14.1, VIT.03.15.7, VIT.03.16.7) and the Research Council of Norway (Grant no. 240065). I acknowledge the support of the people at Andøya Space Center during the integration and campaign work.

The engineers of the project, Sveinung Olsen and Yngve Eilertsen (alphabetic order by first name, no preference) deserves tremendous acknowledgement for their work. I want to personally thank them for the trips to Andøya Space Center and all the ferry rides we have shared.

Throughout the work with MAXIDUSTY I have met and cooperated with a large group of people. Amongst them I wish to thank Ralph Latteck, Gerd Baumgarten, Jan Ove Karlberg, Martin Friedrich, Tom Hartquist, John Plane, Jøran Moen and Espen Trondsen. All co-authors of papers are also thanked in their respective works. In addition, I direct a special thank you to Zoltan Sternovsky for helping with grant application and nice discussions during work with the MXD observations.

I have been fortunate enough to get to work with the student rocket G-Chaser as both a participant and supervisor. I want to thank all the participants on the

SPID team. I acknowledge intern Adrien Pineau for running simulations of dust movement in the SPID probe, some of which have been reproduced in this thesis.

To my fellow office confederates/comrades/accomplices in cahoots; Derek, Theresa and Andreas: Do not fear, we shall rise again. Also, thank you to my previous office partners Lindis, Njål, Jonas and Henry.

I wish to thank my friends and my family. I also wish I had the time to mention you all by name, but alas. Most of all I thank my closest friend Rikard and my partner Tove for their ever loving support.

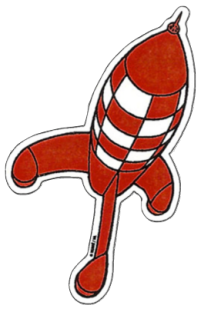

Hooray! Hooray! The end of the world has been postponed!

Hergé
The Shooting Star

Chapter 1

Introduction

This work describes the employment of different sounding rocket probes during the two launches comprising the MAXIDUSTY campaign in the summer of 2016. A main scientific goal of the project is to obtain a greater knowledge about the instrinsic properties of nanoscale aerosols in the upper mesosphere. The multi-scale dynamics of these particles and their interplay with electrons in the dusty plasma is another subject that is given particular attention. The thesis describes the theoretical background of ice particles and particles of meteoric origin in the upper mesosphere, and how these interact with and are detected in rocket probes. Special emphasis is put on the utilization of Faraday cups in determining the sizes, charge state and number density of ice particles and meteoric smoke particles (MSPs) presumed to reside inside them. This volume presents a general overview of the MAXIDUSTY projects and the instruments and a number of key questions connected to the physics of aerosols in mesospheric cloud layers.

A Brief History of Mesospheric Rockets

The *mesosphere* is the atmospheric layer situated between $\sim$ 50 km to $\sim$ 100 km. A thorough introduction is given in chapter 2. As mentioned later on, the first phenomena which where studied in this height region were the optical phenomena; noctilucent clouds were first reported on in the 1880s. In the first half of the 20^{th} century, remote measurements were the only means of investigating the near-Earth space. In 1923, Hermann Oberth introduced the concept of orbital launchers in his book *Rakete zu den Planetenräumen*. In the years around this publication, enthusiasts and military funded scientists set up societies with mission studies and carried out experimental tests of launch vehicles. The first spaceflight society was arguably the German *Verein für Raumschiffahrt*, estab-

lished in 1927.

Along with the second world war came rocket technology and launch vehicles capable of carrying payloads to the boarder of outer space. The V2-rocket desgined by von Braun was arguably the first rocket to be used as a sounding rocket, when it was launched on several occasions from March 1944 and onwards to carry out atmospheric measurements. The first instrumentation included UV spectrometers and barometers (Seibert and Battrick, 2006). The first purely scientific launches thus happened approximately 30 years after Oberth's first conception. After the first sounding rocket launches during WWII, the further development of launchers and rocket boosters gained considerable momentum due to the cold war technology race. After the peak of the cold war armament, large surplusses of solid rocket boosters gave scientists the opportunity to launch payloads to into near-Earth space relativly inexpensively.

The earliest studies of the upper mesosphere were meteorological inquiries. One early investigation technique was to use grenade launches to trace wind (Stroud et al., 1960). Temperature measurements were also among the parameters measured by the first sounding rockets, revealing perplexingly low temperaturs in the summer polar mesopause regions. Rocket observation of this height region soon shifted towards measurements of electrons and ionized species. Pedersen et al. (1970) first reported on the electron bite-out and Anderson (1971) used rockets to measure mesospheric OH. In the following years, electron measurements by Faraday rotation became a standard experiment on typical mesosphere rockets and bite-outs were commonly measured (see e.g Jacobsen and Friedrich (1979)). The mechanism behind the electron depletions and electron density gradients, which were thought to be involved in PMSE, was not known. Havnes et al. (1996) presented a confirmation of the presence of charged particles in the Earth's mesosphere, and confirmed the hypothesis that aerosols could remove electrons by attachment. These measurements were done by the DUSTY instrument – the same design was flown on the MAXIDUSTY payloads. Shortly after the first DUSTY launches, Gelinas et al. (1998) reported on the measurement of $\mathcal{O}(1)$ nanometre particles in the tropical mesosphere; also with a Faraday cup type probe. Since then, Faraday cups have become a common instrument on mesosheric rocket payloads.

Throughout the last decades, the diversity of mesospheric rocket experiments have become greater and instruments have become more capable; among several feats, the unambiguous detection of particles smaller than a few nanometers have become possible. We now have exellent profiles of temperature and neutral

densities in the mesosphere due to a series of falling sphere experiments done in the 1990s (Lübken et al., 1994; Lübken, 1999). Around the same time, several sounding rocket projects had shared interests in the aerosol distribution, charge state and turbulence and wave activity in mesopause cloud systems – with special focus on the summer mesosphere. Collaborating projects such as DROPPS, mini-DUSTY and MIDAS/MaCWAVE gave important insights into such subjects (Goldberg et al., 2001).

In more recent years, a considerable portion of the attention of in-situ studies of the mesosphere have been directed towards the elusive meteoric smoke particles. These coagulates of ablation vapours have sizes up to a few nanometres and are notoriously difficult to probe, due to aerodynamic effects in a payload shock front (Horányi et al., 1999; Hedin et al., 2007; Antonsen and Havnes, 2015; Asmus et al., 2017). Schulte and Arnold (1992) launched an ion quadrupole spectrometre with the capability of characterizing the chemistry of particles related to meteoric ablation and remained the only publication on the topic for some time, before other authors followed (see e.g. Rapp et al. (2007a) for an overview). It has since been found that products of meteoric ablation probably have important roles in the upper atmosphere chemistry. Processes involving sulphur-compounds in the stratosphere and even fertilization of the oceans have been reported on; these are only a couple of interesting processes meteoric smoke are thought to be involved in – see e.g. Bardeen et al. (2008); Megner et al. (2008); Hervig et al. (2017); Plane (2012) and references therein. Due to this, most of the recent mesosperic sounding rocket campaigns have included instrumentation aiming for a better understanding of MSPs. Among others, we mention the ECOMA project (Rapp et al., 2011), the PHOCUS sounding rocket (Hedin et al., 2014) and MAXIDUSTY as some of the more recent endevours looking into meteoric smoke to a certain degree. At the time of writing, measurements from the PMWE-payloads built by IAP and DLR are being processed; the payloads carried several instruments which are aimed towards studying MSPs.

Chapter 2

Nanoparticles In The Terrestrial Mesosphere

The current thesis has its main focus on observations of nanoscale aerosols in the mesosphere during the MAXIDUSTY campaign. The campaign, with principal investigator Ove Havnes of the University of Tromsø, was run with simultaneous support of PMSE and NLC measurements by the MAARSY radar and ALOMAR RMR lidar. In addition to observing large scale structures of mesospheric ice, the two launched payloads had instrumentation aimed towards characterizing intrinsic properties such as size, charge state and chemical content of both ice and meteoric particle species in the upper summer mesosphere. In this chapter, we thus present a thorough introduction to the general characteristics of the region of interest for this project. We discuss the two basic types of particles encountered in mesospheric rocket soundings: ice particles and meteoric smoke particles. We also give a brief introduction to radar measurements of the mesosphere and radar operation during MAXIDUSTY.

2.1 Introduction

The Earth's mesosphere ranges from an altitude of $\sim$ 50 km to $\sim$ 100 km, where it culminates in a region of minimum temperature between 80 and 90 km, called the mesopause. The mesosphere can be considered the uppermost part of the *conventional* atmosphere, as the degree of ionization is low, and turbulence keeps the mixing ratios of the major constituents constant up to altitudes of around 100 km. This latter altitude is also the Kármán definition of outer space. The upper part of the mesosphere is the ambient framework for a number of physical and chemical processes connecting Earth to space.

The meteoric influx to this region and inherent water vapour provides the necessary prerequisites to house a plethora of nanoscale particles. These particles can get ionized by photons from the sun and free electrons and ions, and they subsequently become a part of the *dusty* or *complex* plasma in the upper mesosphere. As table 2.1 shows, in the region immediately below and above the mesopause, the mean free path of neutral gas particles changes from millimetre to centrimetre-scale. For the experimentalist designing instruments for in-situ measurements, this means that ordering parameters such as mean free path, the plasma Debye-length and probe dimensions must be carefully taken into account to make sure an efficient detection of a certain species is made.

Table 2.1: Selected absolute neutral densities obtained by a series of in-situ measurements in the upper mesosphere for winter and summer conditions, as presented in Rapp et al. (2001). The units of densities are m^{-3}.

Altitude (km)	January - March	July - August	Mean Free Path (mm)
71	$9.88 \cdot 10^{20}$	$2.10 \cdot 10^{21}$	2.3/1.1
75	$6.03 \cdot 10^{20}$	$1.27 \cdot 10^{21}$	3.8/1.8
80	$2.82 \cdot 10^{20}$	$5.85 \cdot 10^{20}$	8.2/4.0
85	$1.33 \cdot 10^{20}$	$2.19 \cdot 10^{20}$	17.5/10.6
90	$6.11 \cdot 10^{19}$	$5.86 \cdot 10^{19}$	38.0/39.7

2.2 Thermal Structure and General Characteristics of the Mesosphere

The thermal structure of the upper mesoshere is highly complex with variations on the short time scales as those of gravity waves, to diurnal variations, to the timescales of the long-term trends which are also observed in lower parts of the atmosphere. The temperature is dependent on latitude, and the arctic summer mesopause with a mean temperature of $\lesssim$ 150 K is the coldest part of the entire atmosphere (Lübken, 1999). Due to the relatively high neutral density, the electrons and ions thermalize with the neutrals during undisturbed conditions; $T = T_e = T_i$. With forcing from gravity waves breaking in the mesopause, the temperature can in some rare cases approach 100 K. The winter mesosphere is, somewhat counter intuitive, warmer than the summer mesosphere, and the arctic mesopause region generally have a temperature of above 200 K (Lübken et al., 2006). The reason for the difference in temperature between the summer and winter mesopause must be expained in the framework of large scale

transport and fluid mechanics; Upward propagating gravity waves grow in amplitude as they move to higher altitudes due to decreasing ambient density – i.e. energy conservation. As they reach the mesopause region they can break and deposit momentum which counteracts the radiatively driven winds and reverse the global circulation at 80-90 km. The net effect is a pole to pole circulation, which due to continuity implies a compression of the winter mesopause and expansion of the summer mesosphere. Consequently the summer mesopause is $\sim$ 70 K colder than it would be if only a radiative equilibrium is considered. The winter mesopause is conversely $\sim$ 20 K warmer than this equilibrium (see e.g. Meriwether and Gerrard (2004) and references therein). Figure 2.1, from Lübken et al. (2009), gives a description of the temperature of the upper mesosphere throughout the year, based on lidar measurements. The summer-winter difference is clearly apparent here.

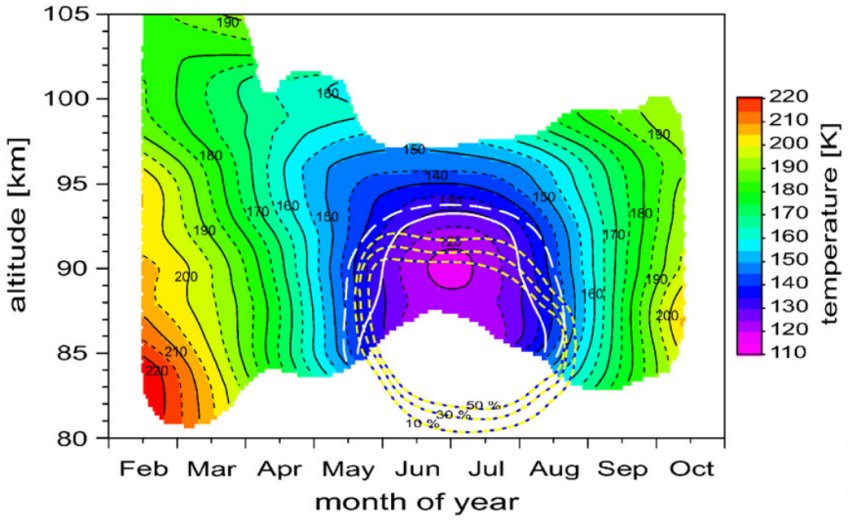

Figure 2.1: Monthly mean temperature values in the mesopause region derived by lidar observations between 2001 and 2003. The white lines indicate supersaturated regions, and the yellow contours show different occurence frequencies of PMSE in the same time period. Reprinted from Lübken et al. (2009) ©Elsevier.

Regarding long term temperature trends in the upper mesosphere, the main mechanism is strongly connected to the same atmospheric constituent which induces warming at lower altitudes, namely CO_2. The upper mesosphere is not in radiative equilibrium, and emission from CO_2 at 15μm (Fomichev et al., 1998) – commonly termed *radiative cooling* – reduces the neutral temperature. Ozone (O_3) is another key component in the energy balance of the mesosphere and is in fact the main driver of the year-to-year variability in the upper mesosphere temperature since the CO_2 concentration has little variance – it has been steadily

increasing since the start of the industrial era. In a modelling study, Lübken et al. (2013) found the radiative cooling of carbon dioxide and long term reduction in O_3 to yield a net cooling of $\approx$ 1.8 K/decade at an altitude of 70 km. In an overview of temperature trends at 70 km in the mesosphere obtained after year 2003, Beig (2011) found the general trend to be negative: The mesopause temperature, where earlier reports have cloncluded with almost no trend, was found to decrease weakly.

The prediction of long term trends in the upper mesosphere temperature is complicated by the complex interplay between constituents such as CO_2, CH_4 and O_3 and aerosols. Solar forcing can also affect the temperature in the upper mesosphere (Austin et al., 2008). To parameterize minor constituents in Whole Atmosphere Models correctly, in-situ measurements are important.

As presented below, the decreasing temperature in the upper mesosphere yields an increase in the occurence of clouds consisting of icy nanoparticles. In the following, we introduce the role of nanoscale aerosols in the upper mesosphere in depth. The focus is put on the types of particles (and intrinsic properties of these) which are relevant for the MAXIDUSTY project.

2.3 Mesospheric Nanoscale Particles

Aerosols in the mesosphere, sometimes referred to as dust in their charged state, are abundant throughout the entire height region from $\sim$ 50 to 100 km. In this altitude region they can obtain charge by electron attachment, radiation-driven detachment and other ionization mechanisms and constitute a so-called "dusty" or "complex" plasma. Throughout the last few decades, a variety of aerosol types have been identified in the upper mesosphere; ice particles, meteoric smoke particles (MSPs) from re-condensation of ablation vapours, metallic layers from differential ablation and hybrid particles of ice and meteoric remnants. All of these particle types can interact with each other and influence the mesospheric chemistry to varying degrees. The present work focuses on the detection and characteristics of nanoscale particles of ice, MSPs and the hybrid of these – sometimes referred to as *dirty ice*. The aerosols types of main interest for MAXIDUSTY are described below.

Due to the inaccessibility of the mesosphere – too low pressure for even the most sophisticated balloons, too high neutral drag for satellites to keep their orbit for extended periods – the only means of in-situ observation is by sounding rock-

ets. Nanoscale particles can in many cases be observed remotely by radar, lidar or spaceborne instrumentation, however, direct probing and sampling is needed for determination of instrinsic properties like charge state and composition. The complicated detection of mesospheric aerosols is a reason for that the role of these particles in a number of physical and chemical processes are poorly understood. A motivation for the work carried out in the current project is that mesospheric aerosols are thought to be involved in processes further down in the atmosphere. Gravitational sedimentation transports the particles down to the stratosphere where they subsequently can be effective sinks for ozone and act as cloud nuclei is especially important (Voigt et al., 2005; Murad et al., 1981; Solomon, 1999).

Mesospheric Ice Particles

Mesospheric ice particles are one of the more readily observed phenomena in the mesosphere. Ice particles of sizes above $\sim$ 10 nm can manifest themselves in noctilucent clouds (NLC) during twilight. This phenomenon typically occurs in the lower parts of the mesopause at altitudes from $\sim$ 80 to 84 km during the polar summer months. Ice particles of similar sizes moreover have an important role in the radar phenomenon Polar Mesospheric Summer Echoes (PMSE). The strong dependence of radius in the optical backscatter intensity ($\beta \propto r_d^6$) makes it difficult for optical methods such as lidar and CCDs to observe a collection of particles with sizes below $\sim$ 10 nm. The increasing occurence frequency of NLCs have in several work been connected to climate change, and, if nothing else, be a clear indicator of changing ambient parameters (Thomas and Olivero, 2001; Zahn, 2003; Kirkwood et al., 2008). As shown in figure 2.2, the water concentration in the summer mesopause region is around 5-10 ppmv at the lower edge of the mesopause, and the consequence of this for nucleation of large scale ice particles is discussed in more detail below. The concentration of water vapour has been steadily increasing from around 4 ppmv at the start of the industrial era, and the general consensus is that this is the main controlling factor of NLC occurence frequency. In fact, no NLCs were reported on before 1885; this was only two years after the Krakatoa volcano eruption, and some authors have speculated that the increase in water vapour is due to this eruption. Another explanation is that water created in methane oxidation, which has increased with the release of methane from polar ice with increasing ice melting is the main driver of the increase in mesospheric water, and that the concentration before 1885 was simply not high enough to produce an observable NLC

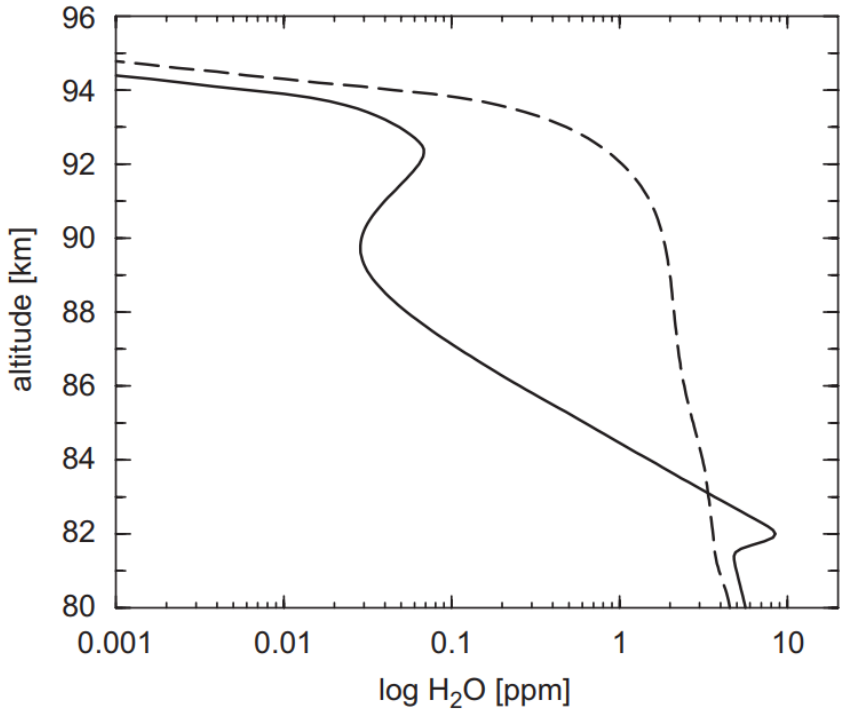

Figure 2.2: Modelled water vapor concentrations mid-summer at 78° N with (solid) and without (dashed) the effect of freeze-drying. Data from Von Zahn and Berger (2003), plot adopted from Lübken et al. (2009) ©Elsevier.

albedo (Thomas et al., 1989). The chemical process lies in the hydrogen balance; $[H] \rightleftharpoons [H_2O] + 2[CH_4] + [H_2]$. As no considerable sources or sinks of hydrogen exist in the upper stratosphere and mesosphere, the balance implies that roughly two water molecules are produces for every destroyed methane molecule. This has been confirmed by satellite observations (Jones et al., 1986).

In the following we address shortly the two possible nucleation mechanisms for mesospheric ice. This concept is important to understand which particle types the Faraday cups on MAXIDUSTY can encounter. First, let us recall Ostwald's rule which states that a thermodynamical state of a nucleation product does not need to be the most stable one, but only the one with the smallest associated free energy. This is to say that supersaturated vapour does not form hexagonal ice structures directly, and in fact for a large range of parameters forms an intermediate amorphus state without crystaline stucture. As pointed out by Zasetsky et al. (2009) and Murray and Jensen (2010), a homogeneous nucleation of ice (water bonding with water) can occur for very steep negative temperature gradients and still satisfy Ostwald's rule. However, in most cases it is more feasible that a third body – a dust grain or more specifically an MSP particle or a smaller dirty ice particle – lowers the energy barrier and promotes a much faster growth

rate than a homogeneous one. This process is called heterogeneous nuclation, which supported by the general finding that large ice particle contain MSPs up to the order of percents by volume. This is also the basis of out model of a typical ice particle, which is used consistently throughout this work. The homogeneous nucleation rate have the following porportionality to free energy (Evans, 1993):

$$R_{\mathrm{Hom}} \propto \left[r_d^{\dagger}\right]^2 \cdot \exp\left[-\frac{\Delta G_i^{\dagger}}{k_B T}\right] \tag{2.1}$$

where $r_d^{\dagger}$ is the critical grain radius and $\Delta G_i^{\dagger}$ is the Gibb's energy for adding an i^{th} molecule to the grain at thermal energy $k_B T$. The result of a third body lowering this latter term implies a faster growth.

In this thesis, Paper III and IV are mainly focussed on the observation of ice particles of sizes $\gtrsim 5$ nm and their characteristics and bulk properties.

Meteoric Smoke Particles

Cosmic dust enters the terrestrial atmosphere with meteoric ablation concentrated in the region from 70 to 110 km. The vapours of refractory elements are believed to re-condense into nanometre-sized dust particles called meteoric smoke particles (MSP) (Hunten et al., 1980; Bardeen et al., 2008; Megner et al., 2006). Despite several attempts, the composition of these particles has not been unambiguously determined, and they are often elusive to in-situ detectors deployed rockets due to their small mass/size. The detection process is elaborated on in chapter 3. Moreover, atomic metal layers in the topside mesosphere are deposited through differential ablation – a process, in which the most volatile (Na, K) elements ablate first, and the less volatile chondritic elements (Fe, Mg, Si) ablate further down (Plane, 2012). To study the role of these metallic layers and MSPs in atmospheric processes, an accurate estimate of the global influx of meteoric material is the most basic parameter. The total Interplanetary Dust Particle input (IDP), has been estimated by several methods; iron sediments in ice cores, zodiacal dust cloud observation and modelling, remote measurements by lidar and radar, and modelling of metallic layer; see Plane (2012) and references therein for a detailed review. Estimates of the IDP from these methods span two orders of magnitude, from 5 to 300 tonnes per day. As illustrated in figure 2.3, the global daily iron input – which is a proxy of the IDP – is found to vary significantly between estimation methods. As an example, sediment collection from ice cores yields higher estimates than other methods by up to two

orders of magnitude. Meteor radar measurements, the most sensitive of which is performed by the Arecibo 430 MHZ radar, give estimates in the lower end of the range (Mathews et al., 2001). On the basis of this, it is clear that the most valuable characteristics still to determine is the true meteor vapor density and true size distribution of meteoric smoke particles. The latter problem is probably best met with in-situ observation.

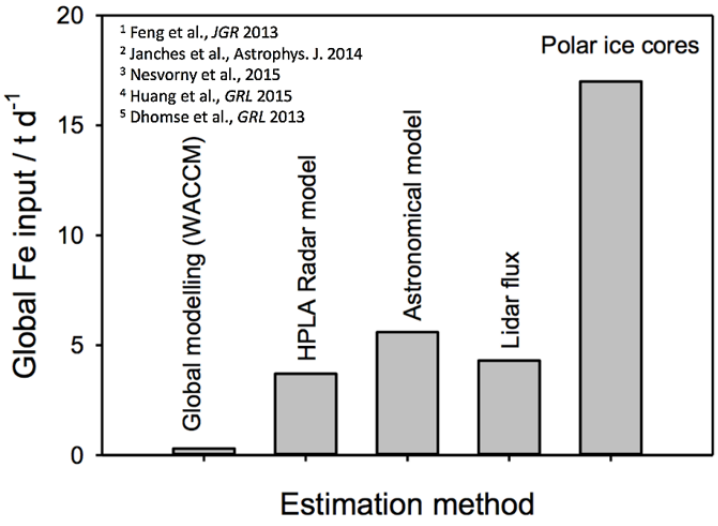

Figure 2.3: Estimation of daily iron input to the atmosphere – a proxy for meteoric influx – based on different models and measurement techniques. The data is adapted from the listed works. Courtesy of Dr. Zoltan Sternovsky, LASP.

It is our current understanding that the primary particles – vapours of nanoscale molecular and particulate matter – formed in the ablation of incoming meteorites, coagulate into particles of sizes ranging from the order of 1 Ångstrøm to a few nanometres (Rosinski and Snow, 1961; Hunten et al., 1980; Kalashnikova et al., 2000). Figure 2.4 shows a sketch of the processes a meteoroid undergoes upon entering the Earth's atmosphere, from initial ablation to the final sedimentation and large scale bulk transport of re-codensed smoke particles. The majority of incoming meteoroids have masses in the range $\sim 10^{-3} - 10^{-6}$ g which corresponds to sizes from a few tens to a few hundred microns. These bodies account for the clear majority of ablated material. Meteorites that do not completely ablate are unlikely to be of great interest due to their small contribution to the total IDP (Hunten et al., 1980). The initial re-condensation of ablation vapours takes place at the topside mesosphere, while gravitational sedimentation provides additional growth. Upwards transport of MSPs due to updraft and circulation of particles is also possible, as indicated in the principle sketch.

No successful retrievals and subsequent mass spectrum analysis of mesospheric

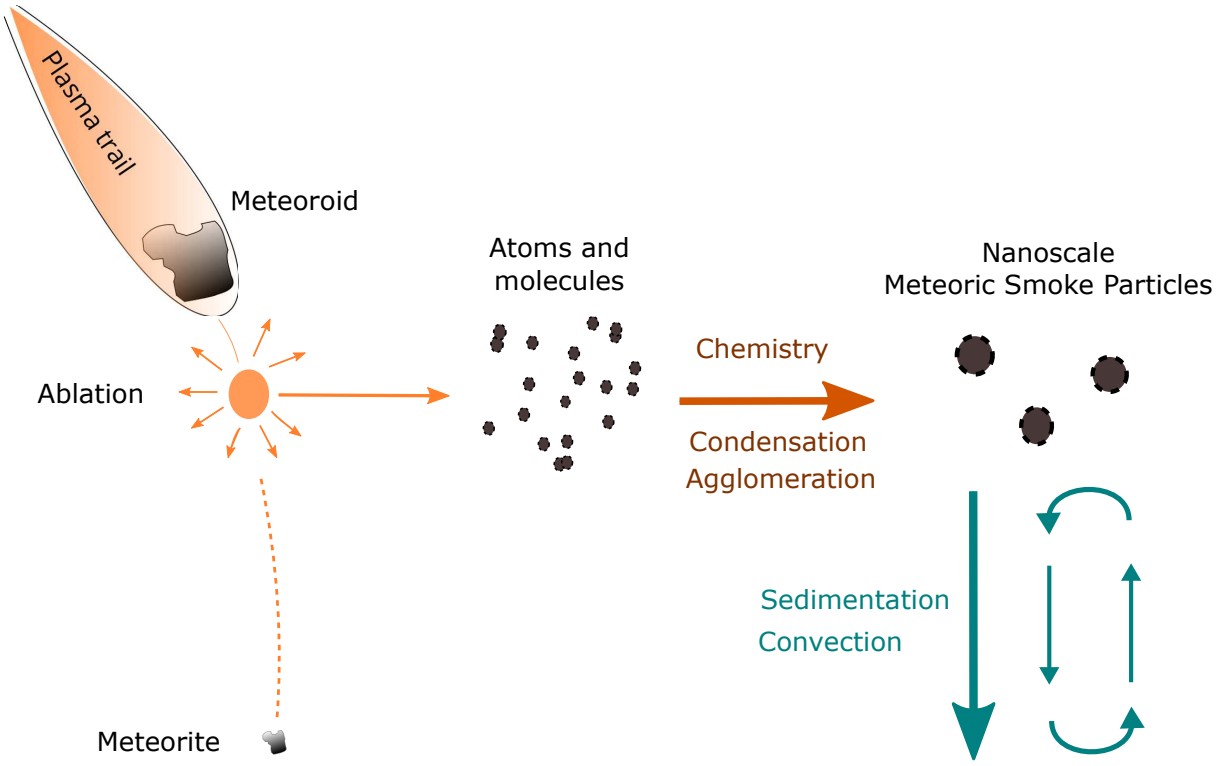

Figure 2.4: Simplified schematic of the process of MSP formation in the altitude range 70-110 km, based on an original illustration from Megner et al. (2006).

MSPs have been done at the time of writing. In the laboratory and through molecular dynamics simulations, it has been found, with the premise that ablation of olivine material injects equal amounts of Mg, Fe and Si in the upper mesosphere, that likely candidates for initial condensation nuclei and small MSPs are metal silicates and metal oxides (Saunders and Plane, 2006; Plane, 2011). The molecular dynamics calculations from these works also verified that such molecular condensation nuclei, having large dipole moments, thermodynamically favor the addition of up to 8 H_2O-molecules on molecules of certain compositions compared to homogeneous nucleation. Using Mie theory, Hervig et al. (2012) reported that the occulation spectra from polar mesospheric clouds matched particles containing up to $\sim$ 3% of either carbon, wüstite (FeO) or a non-stochiometric combination of olivine constituents.

In the present work, one of the main goals have been to design, refine and utilize new experimental methods to resolve the size distribution of MSPs inside large ice particles around the mesopause. Paper I and II along with the work by Havnes et al. (2014) are the contributions to this topic in this dissertation. The general finding, which is introduced in chapter 5, is that MSPs inside large ice

particles probably have a steeper inverse power law than that one of available model predictions. The effect of updraft on MSP growth is one of the discussion topics in Paper V. As it turns out, such transport can probably lead to dust structures and detectable radar echoes on altitudes as low as $\sim$ 70 km in the summer mesosphere – a novel feature termed *Rare Low Summer Mesospheric Clouds* first reported on in Paper V from the MAXIDUSTY campaign.

Charge state of Mesospheric Nanoparticles

The variation in the charge state of free aerosols in the upper mesosphere is mainly controlled by grain composition, size, energetic precipitation and solar irradiation. The grain composition and size controls how effective photoelectric charging, i.e. the ejection of an electron from a grain surface due do incoming photons with energies comparable or larger than the surface work function ($\sim$ a few electron Volts), is compared to collisional charging. Metals more easily yield electrons under solar irradiation compared to ice particles, and as it turns out, smaller particles have a higher affinity for photoemission than larger particles and for mesospheric ice particles larger than 10 nm, photoemission becomes negligible (Havnes and Kassa, 2009; Rapp, 2009). The charge distribution of mesospheric nanoscale particles is sensitive to several factors, that will be introduced below. This thesis deals with a charging model for aerosols in Paper IV, and the following discussion serves as a more in-depth theoretical background. Contact Charging of aerosols upon impact with rocket probes is discussed in Chapter 3.

In general, if a neutral dust grain larger than a few nanometres is placed in the plasma around the mesopause, it will become negatively charged in a matter of seconds to minutes due to electron attachment, for a plausible range of electron densities (Draine and Sutin, 1987)[1]. For the lower range of sizes, the competition between electron attachment and emission and detachment becomes important. As an illustration of the variability in the charge state, we below calculate the distribution of charges on a range of mesospeheric nanoparticles. For plasma particle attachment rates, we use the expressions by Draine and Sutin (1987) and include polarization effects (image charges). The temporal evolution of the dust density at charge state Z, denoted by $N_d(Z)$, can be stated as (Biebricher and

[1]This work discusses interstellar grains, but the attachment current terms can be generalized for mesospheric conditions

Havnes, 2012):

$$\begin{aligned}\frac{\partial N_d(Z)}{\partial t} &= J_d^i(Z-1)N_d(Z-1) - J_d^e(Z)N_d(Z) \\ &- J_d^i(Z)N_d(Z) + J_d^e(Z+1)N_d(Z+1) \\ &- J_d^{\Phi}(Z)N_d(Z) + J_d^{\Phi}(Z-1)N_d(Z-1) \\ &- J_d^{\mathrm{Det}}(Z)N_d(Z) + J_d^{\mathrm{Det}}(Z-1)N_d(Z-1) \end{aligned} \tag{2.2}$$

where $J_d^s(Z) = \tilde{J}_d^s n_s \xi \pi r_d^2 \bar{v}_{th}^s$ is the plasma attachment rates of species s for mean thermal velocity and electron attachement rate ξ from Draine and Sutin (1987). The factor $\tilde{J}_d^s$ contains the polarization contribution. Furthermore, J^{Φ} denotes the photoelectric currents and J_d^{Det} the photodetachment currents to the grain.

If we now normalize the plasma and grain potential such that $\hat{V} = eV/k_BT$ and $\hat{U} = eU/k_BT$ respectively, it can be shown that for Boltzmann distributed plasma particles – i.e. when electric forces balance plasma pressure gradients – that the quasi-neutrality for a thermalized plasma with $T_e = T_i = T$ becomes (Havnes, 2004):

$$\exp\left(\hat{V}\right) - \exp\left(-\hat{V}\right) - P\hat{U} = 0 \tag{2.3}$$

where $P = 0.695 \cdot n_d r_d T_i / n_0$ is the dusty plasma ordering parameter often referred to as the Havnes-parameter (Huba (2018), *NRL Plasma Formulary*). In many cases for the mesopause region, it turns out that quasi-neutrality can be difficult to satisfy, and Poisson's equation must be solved accordingly. However, in cases with little disturbance, e.g. updraft and gravity wave breaking, quasi-neutrality is a good approximation. Havnes et al. (1984) showed that this is valid for dust structures with length spatial scales considerably larger than the Debye-length and plasma temperatures from 150 to 3000 K. In figure 2.5 we show the equilibrium solutions from an iteration of eq. (2.3) with an initial guess of $\hat{V}$ and 12 charge states for ice particles of three different sizes, and with electron and aerosol densities representable for the summer mesopause. In this calculation the electron attachment term dominates, and particles with sizes up to ~ 10 nm are predominantly in charge state $Z = -1$. For the smallest particles photoionization becomes important, and a small portion of 5 nm ice particles (top panel) remain neutral. Large particles with radii $\gtrsim 20$ nm can reach charge state $Z = -3$ and lower for low P-values; i.e. there is an excess of available electrons for an effective collisional charging.

If we now consider the charge state of meteoric smoke particles, we note that there will be a considerable difference in charging efficiency from attachment

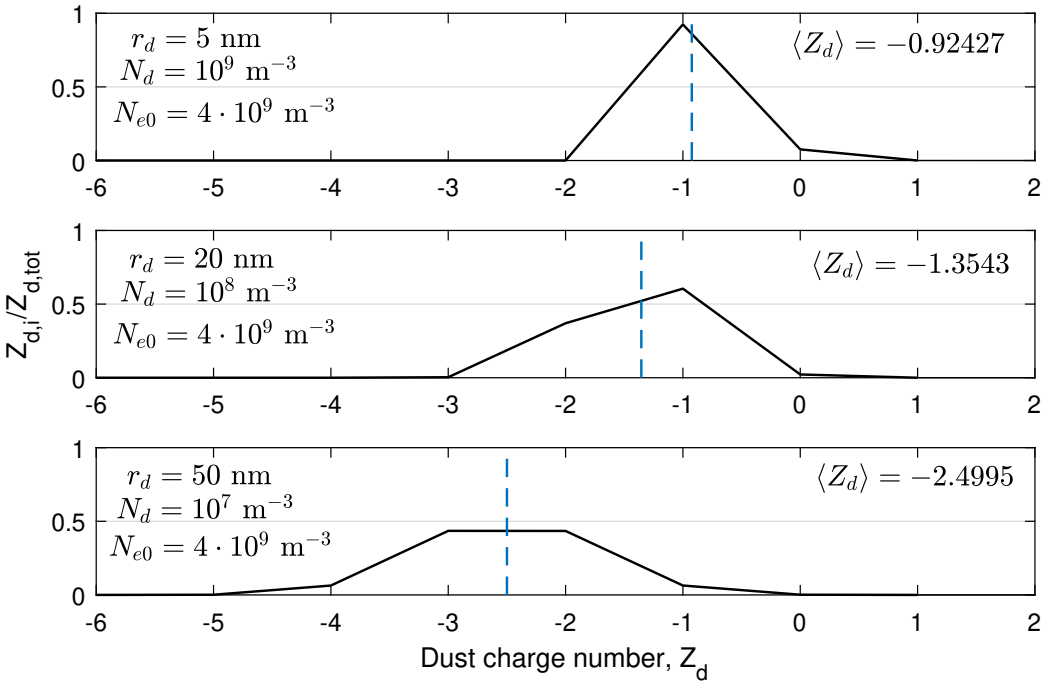

Figure 2.5: Calculated charge distributions for monodisperse mesospherice dust particles for low P-values. The size dependent photodetachment rate and image charge potential is taken into account. The electron attachment coefficient is set to 0.5, in accordance with Draine and Sutin (1987). The values in the brackets denote the average charge.

due to the smaller sizes. The composition of the particles, presumably common meteoric materials such as Fe, Mg, Si and Na, makes the MSPs more susceptible to photoionization compared to ice. In figure 2.6 we present the results of two iterations of eq. (2.3); one run *without* photodetachment (solid lines) and one run *with* photodetachment (dashed lines). The difference is striking for the particles in the lower end of the size spectrum, with photo detachment effectively neutralizing particles smaller than $\sim$ 1 nm. The main takeaway from these simple calculations is that a significant portion of MSPs tend to be neutral and even positive during sunlit (daytime) conditions. Knappmiller et al. (2011) and Asmus et al. (2015) have done thorough investigations into dust charge states when including MSPs and photoionization, and gave similar conclusions – importantly about the presence of positive MSPs in the mesosphere.

Simplified calculations like the charge state calculation presented here yield good estimates of charge distributions of mesospheric nanoparticles which can furthermore be used in discussions of remote and in-situ mesurements. A drawback of such calculations is that there are a number of dusty plasma parameters

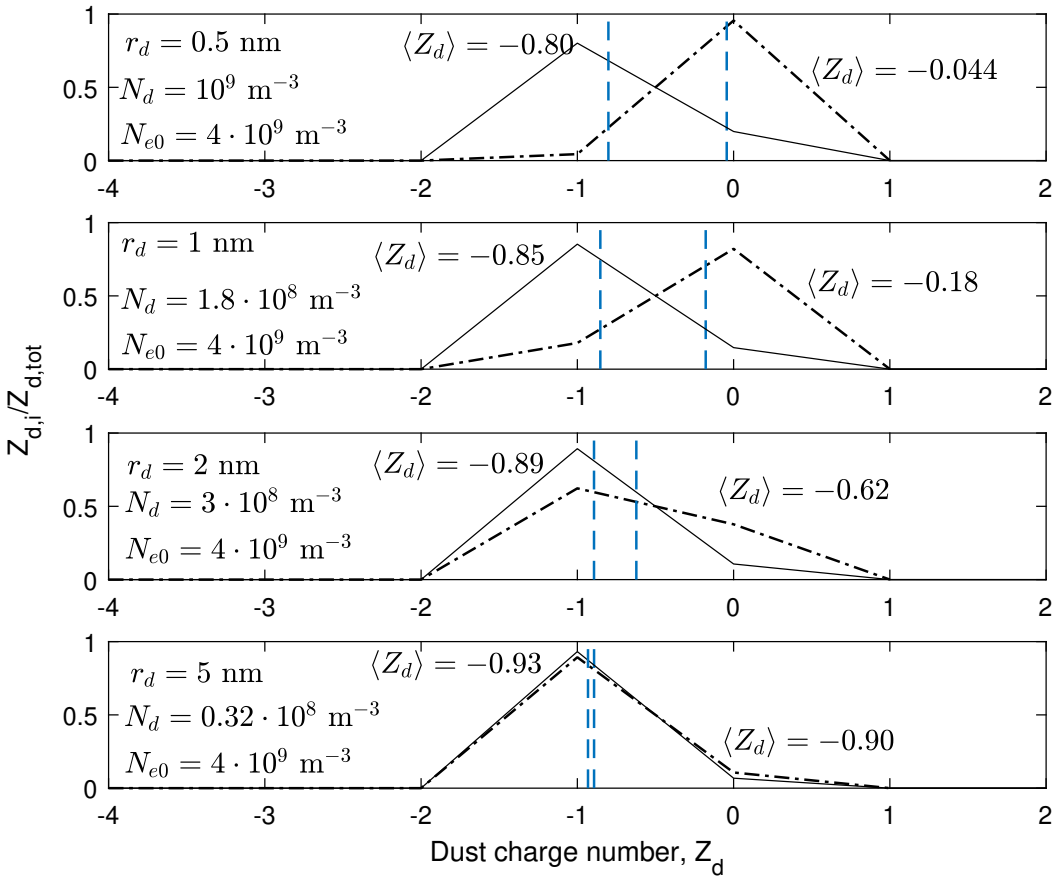

Figure 2.6: Calculated charge distributions for monodisperse MSPs of different sizes. Here, the relative MSP number density between panels follows an inverse power law of $N_{MSP} \propto r^{-2.5}$. The dashed lines show the charge distributions for sunlit conditions with size dependent photodetachment rates of $\{.05, .03, .01, .005\}$ for the four panels (top to bottom). The solid lines show the cases for *no* photodetachment. Image charge potential is taken into account for all cases.

which vary up to orders of magnitude in value throughout a cloud system around the mesopause.

In the current work, one of the main goals have been to eliminate some of the uncertainty connected to these simplified calculation of charge and size distributions by solving for particle charge, size and dust density simultaneously. The results, introduced in section 5.2 and published in Paper IV, is a new method to infer those fundamental dusty plasma properties from Faraday cup data, with high altitude resolution. With the method introduced in that paper, a more correct charging model will directly lower the uncertainty size estimates.

2.4 Remote and In-situ Observation of Mesospheric Clouds

The earliest reports of cloud-like structures at altitudes between 80 and 90 km were reported by several authors in the mid-1880s (Jesse, 1885; Leslie, 1885). It has been speculated that the 1883 eruption of Krakatoa was responsible for depositing volcanic particles at those altitudes, as no NLCs were observed before 1885 (Schröder, 1999). Wegener (1912) suggested that ice particles were abundant in NLCs. The presence of water at such high altitudes were suggested to be a consequence of the global methane (CH_4) increase due to pollution from industry. It was known that methane could oxidize to water in the stratosphere, thus increased water content in the upper atmosphere would eventually lead to condensation of the present vapour. An interesting aspect is that until the first radar observations of the same height region, clouds in the mesopause region was observed both from satellites and by astronauts in orbit (Cho and Röttger, 1997).

The rapid development of Mesosphere-Stratosphere-Troposphere (MST) radars in the 1970s (see e.g. Woodman and Guillen (1974)) provided a remote measurement technique which eventually would be used interferometrically. These radars could also obtain three-dimensional flow velocity vectors. The first observations of coherent radar echoes, polar mesospheric summer echoes (PMSE), were made at VHF frequencies around 1980. The echoes were found to be almost coincident with NLCs and related to subvisible ice particles (see Rapp and Lübken (2004) for a review).

Developments in laser technology made lidar (which was theorized as early as 1930 by Synge) more readily available throughout the 1980s and 1990s. Measurements of particles which scatter light efficiently can be used to estimate particle radii, and Fe-lidars can be used to measure temperature. For MAXIDUSTY, the RMR (Von Zahn et al., 2000) and Fe-lidars at ALOMAR were operated.

During the MAXIDUSTY campaign, the MAARSY MST radar was operated to support the rocket payloads with simultaneous common volume measurements. MAARSY (69.30° N 16.04° N) is a monostatic phased array VHF radar at 53.5 MHz with capabilities to split and steer separate beams. The system therefore allows for continuous 3D monitoring of more than one region separated in space. A feature that is highly valuable for rocket launches is that MAARSY can direct one beam in the payload trajectory direction and other beams outside that vol-

ume. In figure 2.7 we show vertical and horizontal slices of a beam directed along the payload trajectory during MXD-1 in the height range between 80 and 90 km. The PMSE was broad, layered and dynamic.

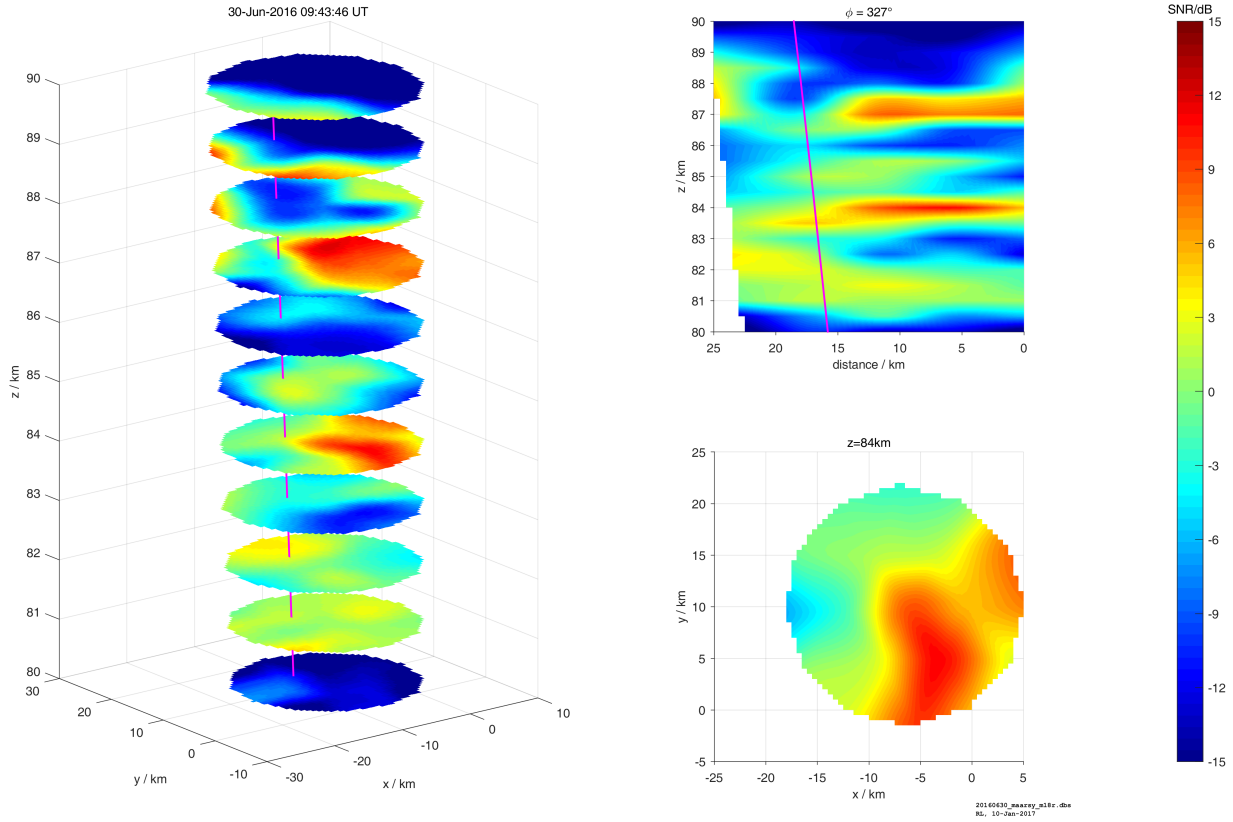

Figure 2.7: PMSE recorded at the time of launch of MXD-1 with the 53.5 MHz MAARSY radar. The radar made measurements in the same volume as the rocket, and the trajectory is indicated as a purple solid line. Courtesy of Dr. Ralph Latteck, IAP.

With the discovery of PMSE, the hypothesis quickly arose that aerosols would be effective sinks for free electrons in this height region. As mentioned in the introduction, Faraday cups were employed to solve the question of such bite-outs. Throughout the last decades, simultaneous measurements by radar and rocket have become most valuable for the investigation of dynamics in a cloud layer; also for the MAXIDUSTY campagin. In figure 2.8 we show a comparison between dust charge number density derived from DUSTY, electron density derived by mNLP and MAARSY SNR. We note, as is discussed in Paper III, that the absolute value of the electron density is probably overestimated, but the relative fluctuations are correctly presented. A clear bite-out is seen between $\sim$ 82 and 87 km. The PMSE does not appear to have a simple connection to the first or-

der plasma parameters, and spans over a larger height region than the depletion. This connection is also discussed in Paper III.

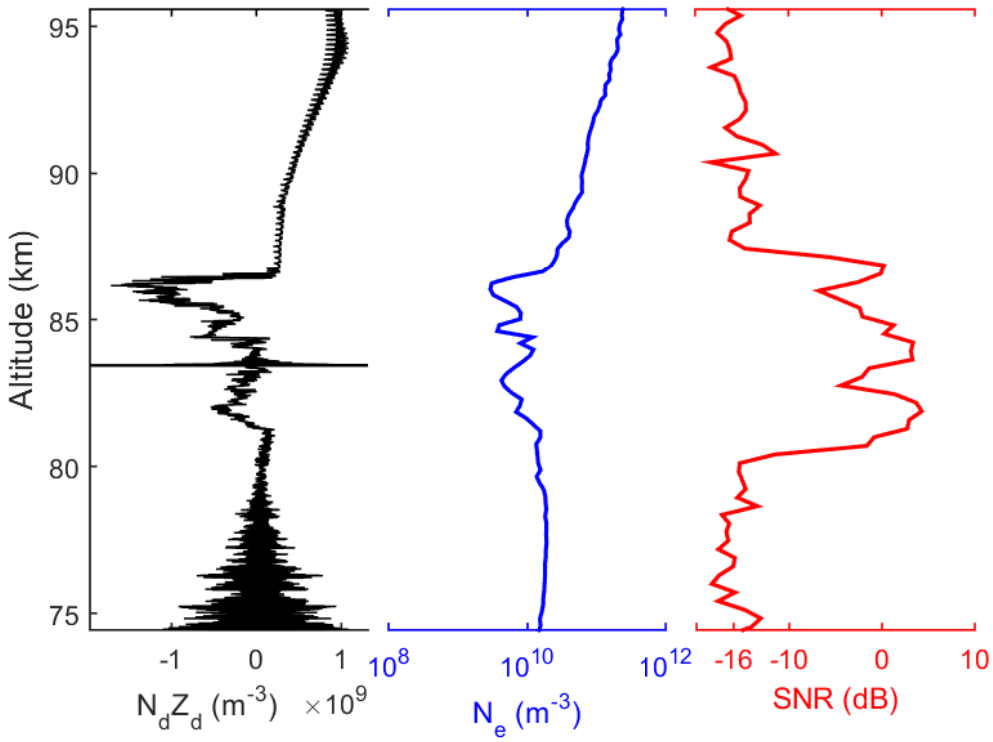

Figure 2.8: Comparison of aerosol charge number density derived from DUSTY currents, electron density from the mNLP-probes and PMSE SNR for MXD-1. A bite-out in the electron population coincides well with the aerosol measurements and SNR, however, the edge profile of the PMSE cannot easily be directly related to first order dusty plasma parameters.

Chapter 3

In-situ Detection of Mesospheric Nanoparticles

The experimental framework for the current thesis is the MAXIDUSTY sounding rocket campaign. In this chapter we introduce the theory behind the prediction of the movement of aerosols around and inside rocket probes. We put special emphasis on Faraday cups as employed on the MAXIDUSTY payload. This theory is used in the accompanying papers to estimate sizes of incoming particles, and is instrumental for correct interpretation of Faraday cup data. Impact charging and secondary charging effects, which is important in the interpretation of Faraday cup currents, is introduced. Moreover, we present a discussion on adverse effects typical for mesospheric in-situ measurements.

3.1 Dynamics of Nanoparticles in the Vicinity of Rocket Probes

There are two main factors controlling, or rather obstructing and interfering, the detection of nanoscale mesospheric particles. These are *flow fields* in the neutral gas which affect particles through collisions, and *electric fields* which interact through electric forces with charged grains. The kinetic energy of a nanoparticle of size 1 nm with a density from 1 to 10 gcm^{-3} at a rocket speed of $\sim$ 1 kms^{-1} – relevant for mesospheric rocket studies, is $\mathcal{O}(10-100)$ eV. These energies are comparable to or much larger than the electrostatic barriers of typical biased probes ($\sim$ a few eV) for grains charged with up to a few elementary charges; be it Langmuir probes or Faraday cups. A takeaway from this is that for the 'large' ice partices involved in NLCs and PMSEs, the electrostatic barrier will not affect recorded currents in DUSTY and MUDD probes significantly.

To analyse the evolution of NLCs and PMSEs, distinction between nucleation mechanisms and a number of phenomena involving the interplay between MSPs and ice particles, one needs to be able to observe particles of sizes $\lesssim$ 1 nm (Horányi et al., 1999). For these smaller particles, the aerodynamical envrionment can completely define the detection efficiency. The task to calculate this detection efficiency require subtantial simulation efforts, and since such considerations are important in many of the studies presented in this dissertation, we should discuss a few of the most important factors of nanoparticle dynamics. Antonsen and Havnes (2015) (Paper I) deals with transport of particles in the framework of MUDD. The reader is also referred to the works of Hedin et al. (2007) and Asmus et al. (2017) which have recently offered new insight on central topics regarding the detection of particles in the lower end of the size spectrum.

Pressure regime

To calculate the trajectory of a nanoparticle in the vicinity of a rocket probe, detailed knowledge about the neutral flowfield is required. As shown in table 2.1, the mean free path of neutrals traverses values from $\sim$ 1 mm to $\sim$ 40 mm in the altitude region from 70 to 90 km. In many rocket instruments, these scales can be longer than several or all characteristic length scales of a rocket robe – i.e. probe radius, length or longest internal clear path. This offers a big problem, as fluid mechanical calculations cannot be used; the explanation boils down to an undefined collision derivative in the Boltzmann transport equation. An arduous solution to this can in some cases be the Chapman-Enskog expansion – i.e. expansion of the collision term in Navier-Stokes through the parameter $\mathrm{Kn} = \lambda/L_p$, where λ is the mean free path and L_p is a characteristic system length (Boyd, 2003). A correction term for the probability that a given nanoparticle misses or *slips* a collision within a characteristic length can also be used (Cunningham slip factor; see e.g. Moshfegh et al. (2010)). However, in most cases it is easier to utilize Monte Carlo simulations of the movement of a large amount of test particles to yield a statistically probable flow field (Bird, 2005). In figure 3.1 we show a velocity field extracted from such a simulation, for the MUDD Faraday cup MUDD, which was flown on both MXD payloads. The fields can furthermore be used as input in calculation of nanoparticle trajectories. It should be noted that this example simulation is for an isolated probe, and that effects due to neighboring probes is not included. Throughout this thesis, the DSMC software for two- and three-dimension flows written by G. Bird is utilized.

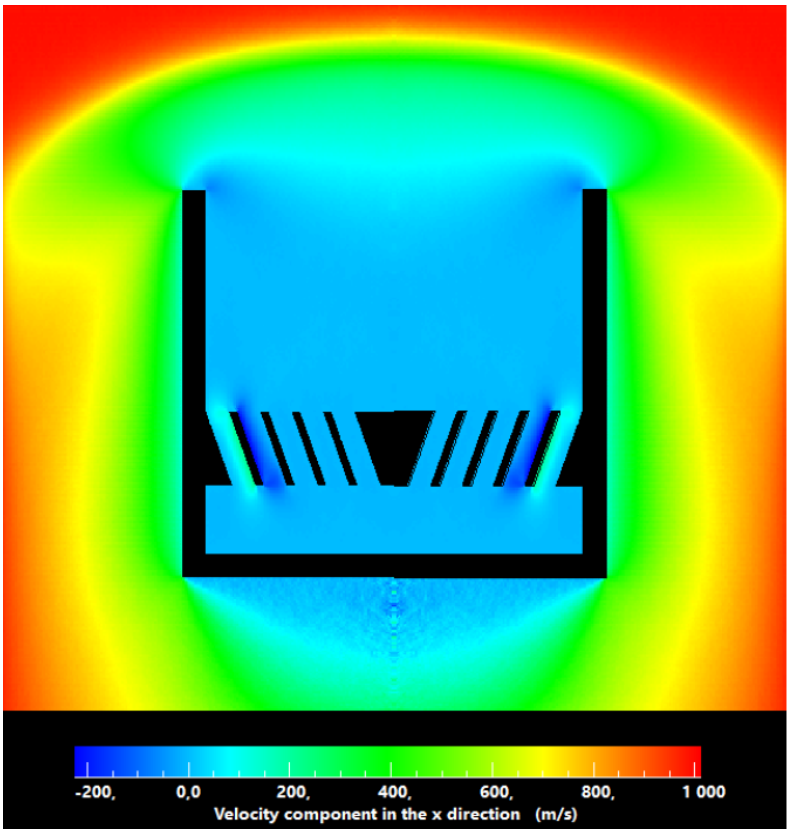

Figure 3.1: Flow speed at 70 km in the direction along the rocket payload (here termed 'x') extracted from a Monte Carlo-simulation of a rotationally symmetric flow for the MUDD Faraday cup. The thin grid wires above the impact grids were not included here.

Particle characteristics

For rocket studies, a payload can traverse orders of magnitude of characteristic length scales. The probe dimension compared to characteristic lengths such as the Debye length (λ_D) and mean free path (λ), determines the collection cross-section of a probe. However, even if one carefully use the correct probe theory and take all non-continuum flow effects into account, a significant error can still lie in the *assumptions of intrinsic parameters* of the observed particles.

In Paper I we present list of probable values of densities, surface energies, specific heats and latent heats of vaporization for smoke and ice particles, as well as their respective references. These values can differ by a factor up to a few, and certain parameters can moreover be temperature dependent. The uncertainty is lower for ice particles, as ice in all its normal forms (amorphous to hexagonal) have relatively similar characteristics. Although there is much research on meteoric analogues, there is still a large uncertainty in the MSP characteristica as their composition has not been determined unambiguously at the time of writing. The

problem is thus choosing the correct values. Consequently the thermodynamic calculations of meteoric dust have significant uncertainties.

Moreover, particles smaller than a few tens of nanometers have peculiar radiative properties. Thermal radiation peaks in the infrared part of the spectrum, at wavelengths much larger than typical grain sizes. Thus thermal re-radiation tend to deviate from Stefan-Boltzmann's law and sub-nanometer grains effectively do not radiate away heat (Rizk et al., 1991). Therefore, the size-dependent emissivity must be considered. Another factor which must be taken into account is the shape of the grains; certain molecular compositions are more probable to condense into long chain-like agglomerates, whiles other form spherical grains. The grain shape, as demonstrated below, can be parameterized as a factor in the drag force term. DeCarlo et al. (2004) and Saunders et al. (2010) found that this term varies from 1 to $\sim$ 1.6 for shapes typical for agglomerates and condensates. For the particles in the lower end of the size spectrum, the *nano-Kelvin effect* must also be considered, i.e. the curvature dependence of vapour pressure (Evans, 1993).

Modified equations for drag force and energy balance

If all intrinsic parameters of the nanoparticles were known with certainty, there is still an issue of understanding the collision process between neutrals and a grain. In practice, this means finding a good expression for the drag coefficient. The reason why this is non-trivial is that a typical grain is much smaller than the mean free path, but not necessarily small enough for Brownian effects to be important. As reviewed in Zuppardi et al. (2015), there are several models which can estimate the drag coefficient in such rarefied flows, however, there are many challenges with assigning corrections to continuum equations. Accordingly, the authors find that different existing models can in many cases disagree. There are also problems connected to surface interacations of both neutrals and aerosols with the rocket payload, which is discussed below.

For the calculation of the neutral drag on an aerosol in the works compiled in the present dissertation, we have utilized a collision model which assumes that neutral molecules interact specularly with a nanoparticle; i.e. they are reflected with the same angle as the incident. We have also assumed that a single dust particle cannot modify the density or velocity distribution of neutrals, and take the neutral velocity distribution to be Maxwellian. We also assume that the aerosol mass is much greater than 29 atomic mass units (AMU) which is the mean neu-

tral mass. The combination of these assumptions yields a model which is mathematically similar to those of Baines et al. (1965) and Smirnov et al. (2007); the latter work used the same model for neutral-dust interaction in calculations of the movement of nanodust in a fusion device.

We highlight the important physical considerations connected to our neutral drag term in the following (in spherical coordinates; (r, θ, ϕ)). We let the neutral thermal speed be defined by $v_{th}^2 = 2k_B T_N/m_N$, where m_N is the molecular mass of the neutral gas. The probability of a neutral molecule having a speed exactly within $v + \mathrm{d}v$ along the direction perpendicular to the polar direction is then, from Maxwell-Boltzmann's distribution:

$$p(v, v + \mathrm{d}v) = \frac{1}{v_{th}\sqrt{\pi}} \exp\left[\left(-\frac{v}{v_{th}}\right)^2\right] \mathrm{d}v \tag{3.1}$$

If we furthermore let $\mathbf{u}$, with $||\mathbf{u}|| = u$ be the velocity of the nanoparticle (assumed to be spherical), the momentum transferred to a surface element $\mathrm{d}A$ per unit time due to neutrals with speed v can easily be calculated as:

$$2m_N n_N \frac{1}{v_{th}\sqrt{\pi}} (v + u\cos\theta)^2 \exp\left[\left(-\frac{v}{v_{th}}\right)^2\right] \mathrm{d}v\mathrm{d}A \tag{3.2}$$

The drag force can then be obtained by integrating this contribution for all molecular speeds and all angles θ. The result is an expression which is valid for rarefied flows in both sub- and supersonic flow regimes (the latter is not covered by the normal Stokes' equation), and can be stated as:

$$\mathbf{F}_D = \chi\pi r_d^2 m_N n_N v_{th}(\mathbf{v}-\mathbf{u})\frac{1}{S}\left\{\frac{1}{\sqrt{\pi}}\left(S + \frac{1}{2S}\right)\exp(-S^2) + \left(1 + S^2 - \frac{1}{4S^2}\right)\mathrm{erf}(S)\right\} \tag{3.3}$$

where χ is the shape factor defined as the ratio between the drag of a volume equivalent sphere of a non-spherical particle and a spherical particle. The parameter $S = ||\mathbf{v} - \mathbf{u}||/v_{th}$ contains the relative speed, and $\mathrm{erf}(S)$ denotes the error function of the relative speed. This expression for the drag force self-consistently contains the drag coefficient, and the expression in the bracket is accordingly $2\sqrt{(\pi)}C_D$ for specular reflection (where C_D is the drag coefficient).

For the *energy balance*, we add to the assumptions that molecules leaving the dust grain surface does so diffusively, i.e. they have a three dimensional velocity distribution. Fundamentally, the energy balance – here used as analogous to the

heat balance – is the temporal evolution of the dust grain enthalpy, H_d. In terms of intrinsic properties of the grain we have:

$$\frac{\mathrm{d}H_d}{\mathrm{d}t} = P_H - P_C = m_d c_p \frac{\mathrm{d}T_d}{\mathrm{d}t} + L_d \frac{\mathrm{d}m_d}{\mathrm{d}t} \tag{3.4}$$

where m_d, T_d and L_d are the mass, temperature and latent heat of evaporation (no melting and grain deformation due to large temperature gradients) of the grain. The specific heat is denoted by c_p. P_H and P_C are the heating and cooling powers of the grain, respectively. We furthermore make the assumption that a nanoscale grain re-radiates poorly in the infrared part of the spectrum, thus grain cooling will only happen through surface molecules being emitted (Rizk et al., 1991). The temperature difference between a mesospheric aerosol and neutrals have been found to increase with grain size (Grams and Fiocco, 1977; Eidhammer and Havnes, 2001). The heating power will be dominated by the neutral-grain collisions. To find the contribution from this series of binary interactions, we average the flux of kinetic energy of neutrals to the grain, over their velocity distribution. If we assume that the neutral molecules have a Maxwellian velocity distribution, it can be shown that the heating power becomes (Allen et al. (2000); Smirnov et al. (2007)):

$$P_H = \pi r_d^2 n_N v_{th} k_B T_N \left\{ \frac{1}{2\sqrt{\pi}} \left[5 + 2S^2\right] \exp(-S^2) + \frac{1}{4S} \left[3 + 12S^2 + 4S^4\right] \mathrm{erf}(S) \right\} \tag{3.5}$$

where T_N is the neutral temperature. In our calculations we solve the simultaneous equations for energy balance and temporal evolution of grain radius and temperature. Example simulations for an open and a closed Faraday cup are shown below.

Adverse and poorly understood effects

In most codes for Monte Carlo simulation of rarefied gas flows, the default assumption is that surface interactions are fully diffusive; without a specular bias. According to Zuppardi et al. (2015) and references therein, this assumption is not valid in all cases. If a smooth surface has been exposed to ultra-high vacuum for a long time, the surface has a high temperature compared to its surroundings, the probe material has significantly higher molecular mass than the neutral gas or the translational energy of the neutral molecule is larger than several eV, the assumption must be reviewed. For rocket soundings, a large variety in parameters such as impact energy of the impinging molecules, surface temperature, material

and roughness of the surface can be encountered. Thus, some caution should be taken when using neutral gas flow simulations inside and around rocket instruments.

There is also some uncertainty connected to the interaction of the mesospheric aerosols with probe surfaces. In Papers I and II of this dissertation, the argumentation is used that for certain geometries and parameters, larger ice particles tend to fragment and what is recorded on the bottom detector plate is dominated by MSPs. However, particles of different materials may interact differently with the surfaces inside probes and uncertainties are naturally connected to this. A large part of this uncertainty is connected to the secondary charge production mechanism inside probes, which is not properly understood. This concept is discussed in section 3.2. As is presented there, one can control for secondary charge production by comparing the currents of the impact Faraday cup MUDD and classical Faraday cup DUSTY.

In addition to the complex aerodynamical environment around a rocket probe and the challenges arising in the characterization of it, one must also consider the electric potential structure around the payload. Aerosols readily become charged, and particles with low energy can easily be dictated by potentials as low as on the order of 1 V. A payload can be charged by direct collection of plasma, but also secondarily charged by dust grains rubbing off electron from the metal chassis of the payload body. The payload can then become positive. There are however few reliable methods to measure the payload potential, and the calibration process in such a measurement can be complicated. One method which have been shown to be reliable at altitudes above 90 km, is using the needle Langmuir probes (mNLP, University of Oslo) which were flown on both MXD payloads. Figure 3.2 shows the floating potential of the payload derived from the mNLP experiment. Above 90 km, the floating potential was situated at around -2.5 V on the upleg and around -3 V on the downleg. This indicates that the lowest biased probe (at 3 V) was likely not in the saturation region, and the absolute values of electron density derived inside the cloud layer are not reliable. The mNLP theory uses OML theory (see e.g. Jacobsen et al. (2010)) to calculate n_e, and therefore assumes a collisionless sheath, which is probably not the case at altitudes below 90 km for MXD, where the mean free path of neutrals is relatively short. Moreover, the strong positive values at altitudues below $\sim$ 90 km can also be overestimated (Priv. Comm. Andres Spicher).

From this brief discussion, it is evident that a thorough characterization of the aerodynamical and electrostatic environment outside and inside rocket probes

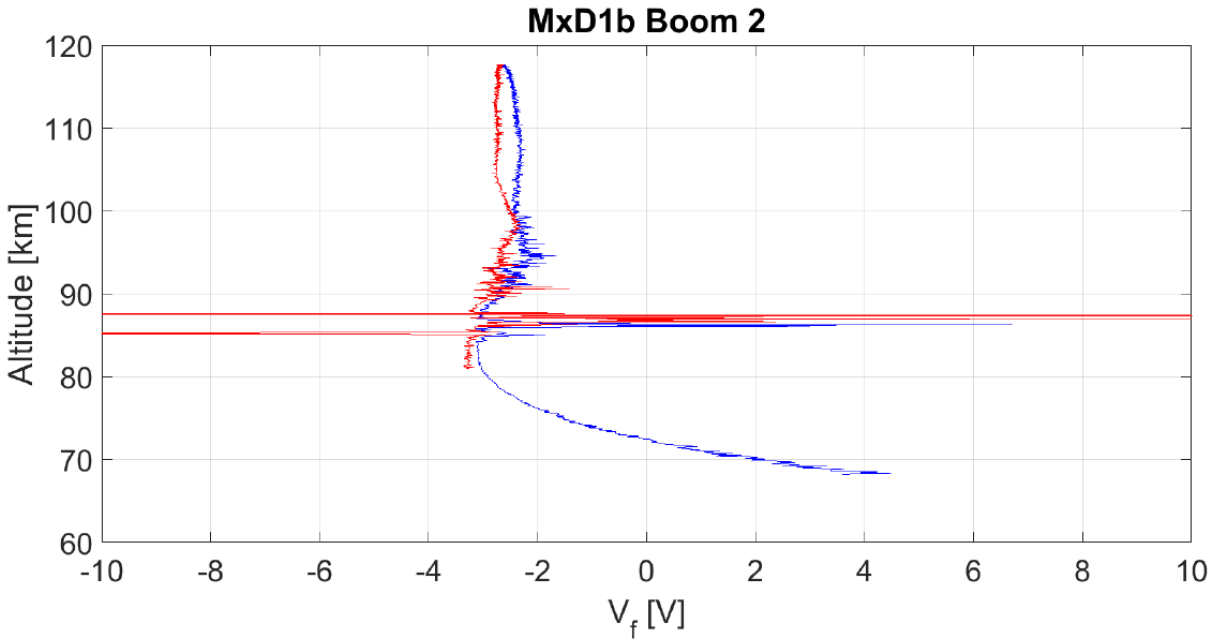

Figure 3.2: Floating potential of the MXD-1B payload derived from measurements by the multi-Needle Langmuir Probe experiment (University of Oslo). Courtesy of Andres Spicher, UiO.

must be done in order to correctly interpret the recorded signals. Paper III points on a special case during MXD-1B in which such considerations become highly important.

3.2 Interaction Between Aerosols and Rocket Probe Surfaces

Due to the probable plethora of different compositions and structures of mesospheric nanoparticles, the assumption that all particles are detected at equal rates is a questionable. The most important separation is between particles mainly consisting of ice and particles of meteoric material. Different work functions and affinity for charge transfer, among other intrinsic differences, makes the detection of these two particle types almost fundamentally different – even though the charge transfer mechanism may the same.

Impact Charging

Some of the main results of the present work is dependent on an understanding, or thorough characterization of, the charging process that takes place during a collision between a mesospheric aerosol and the surfaces of a probe. The word *during* here is key, as the collision cannot be generalized into an impulsive binary interaction. Amorphous aerosols generally have a certain degree of plasticity, and particles deform and fragment during a collision. It is difficult to generalize simple results to nanoscale particle-surface interaction.

The impact charging of micrometeorites and micrometre-sized dust grains have been studied in laboratories since the 1960s. For several years, the charge production was thought to not change significantly within a large range of velocities and particle masses, however, this is found to not be the case for collisions of either very high or very low interaction energy (Friichtenicht, 1964; Adams and Smith, 1971; John et al., 1980). In figure 3.3 we show the results from a laboratory experiment where iron particles were accelerated towards an iridium target with a large range of initial speeds. It can clearly be decided that the q/m vs. speed-relationship is non-linear. Importantly, the bouncing charge transfer mechanism for low velocity/small particle collisions ($< 1000\ \mathrm{ms}^{-1}$, $\lesssim 10$ nm) is not well understood, and few experiments have the capability to inquire about the particle energies relevant for mesospheric aerosols (Kuuluvainen et al., 2013). In energetic collisions, a cloud of plasma is formed upon interaction and charges are recollected partially or completely by the surface. The charging mechanism relevant for a typical mesospheric aerosol grazing a surface on the inside of a rocket probe is poorly represented by such a picture; it is rather likely a nanoscale analogue to triboelectric charging. To our knowledge, the triboelectic effect has only

been investigated in-depth for large – on the order of several micrometres – particles with low impact energies (Kuuluvainen et al., 2016).

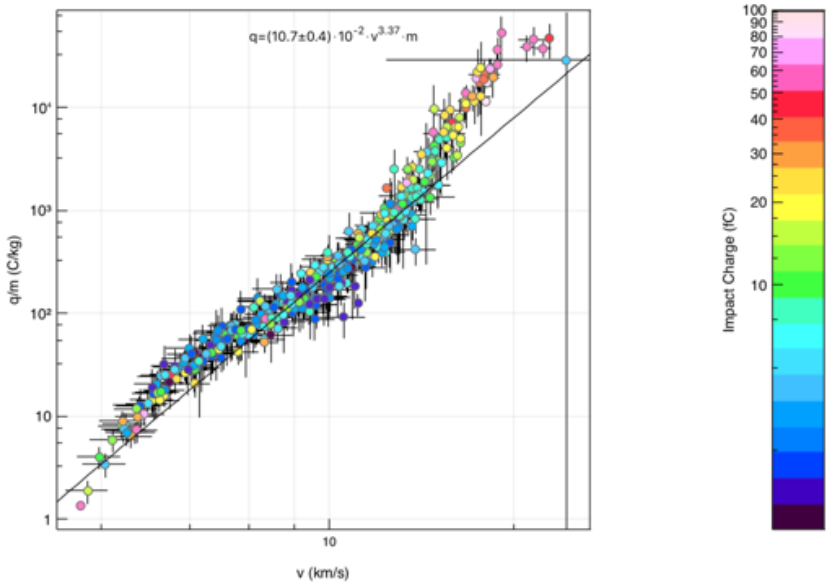

Figure 3.3: Log-Log presentation of laboratory measurements from dust accelerator experiments of iron particles on an iridium target (common for probe calibration) showing generated charge per mass compared to impact velocity. The relationship is clearly not linear. Courtesy of Dr. Zoltan Sternovsky, LASP.

John et al. (1980) derived a simple model for contact charging between a spherical grain and a smooth surface. It was later pointed out by Bailey (1984) that the grazing happening in inclined collisions affected the efficiency of the charge transfer. The general result for a particle of some elasticity, contact area A, "effective" separation between surface and particle d, and electrical capacity $C = \epsilon_0 A d$ the charge generated on contact can be written

$$Q_c = CV_c\left(1 - \mathrm{e}^{-\Delta t/\tau}\right) \tag{3.6}$$

$$= \frac{\epsilon_0 V_c}{d}\left[\frac{5}{4}\pi^2\rho_d v^2(k + k_s)\right]^{\frac{2}{5}} r_d^2\left((1 - \mathrm{e}^{-\Delta t/\tau}\right) \tag{3.7}$$

where V_c is the contact potential between the surface and particle and Δt and τ are the contact and relaxation times respectively. The expression in the square brackets describes the elastic response of the particle. For a conducting particle, $\Delta t/\tau \to 0$, and the relaxing term will vanish:

$$Q_c = \frac{\epsilon_0 V_c}{d}\left[\frac{5}{4}\pi^2\rho_d(k + k_s)\right]^{\frac{2}{5}} v^{4/5} r_d^2 \tag{3.8}$$

that is a charging probability proportional to particle cross-section. For insulating particles, the interaction time is much smaller than the relaxation, and thus $\tau/\Delta t \to 0$. It follows that the contact charge approaches $Q_c = CV_c\Delta t/\tau$. Since the relaxation time is given as the product of the permittivity times the resistivity of the material, $\tau = \epsilon\rho_R$ in which $[\rho_R] = \Omega \times m$, it can be shown dimensionally that the contact charging for insulating materials must become proportional to the particle volume:

$$Q_c \propto v^{3/5} r_d^3. \tag{3.9}$$

One immediate questions arise regarding the applicability of the results above: Is the ideal model for contact charging representable for rocket probes? This question provides motivation for the next section.

Secondary Charging Effects in Rocket Probes

The answer to the question posted above is probably not a straight yes or no. The equations presented are valid for homogeneous particles of sizes orders of magnitude larger than a typical mesospheric nanoparticle, which is arguably too ideal of a description for mesospheric aerosols. The lack of large scale crystalinity (amorphous state) and size dependent emissivity and dielectric properties may influence the affinity of a particle to absorb or release an electron.

Throughout this work, we use the term *secondary charge* when describing certain signatures in rocket probe currents. Contrary to primary charge, which is the charge delivered directly to a detector by charged aerosols (or unshielded electrons and ions), the secondary charge can be understood as the transfer of electrons *from* payload surfaces or inner parts of a probe to aerosols or fragments of aerosols. In a fragmentation process, the secondary yield per particle can be as large as 100 elementary charges, which will heavily affect or even dominate probe currents (Havnes and Næsheim, 2007; Amyx et al., 2008; Havnes et al., 2009; Kassa et al., 2012).

There is currently no consensus on what the exact mechanism and connection to classical contact charging is. The main candidate is that aerosols grazing on metal surfaces get charged in a triboelectric fashion which involves adheshion on the nanoscale. In a series of experiments with ice particles of sizes down to a few nanometres, it was found that particles colliding with gold and graphite surfaces fragmented at impact speeds comparable to those of sounding rockets (Andersson et al., 1997; Markovic et al., 1999; Tomsic et al., 2000, 2001). Tomsic et al. (2003) reported that pure ice particle of sizes larger than 6-7 nm had

a certain probability of carrying away a charge of $-1e$ for grazing impacts. The probability was found to be strongly dependent on impact angle, with a maximum around 80°. The charging for nanoscale ice was found to be proportional to r_{ice}^2 – which is not consistent with the contact charging results above. From earlier measurement, Vostrikov and Dubov (1991) had already found that approximately 1 in 10000 ice clusters of radius $\sim$ 2 nm were charged in impact at relatively low speeds. There are few similar experiments which go into the same depth as the ice experiments for nanoscale metal particles impacting at low speeds. The charging probability is therefore still an open question; In Paper II we utilized $Q \propto r_d^2$ and $Q \propto r_d^3$ when calculating the size distribution of collision fragments.

Although the theoretical aspects of the nano-triboelectric effect in rocket probes are somewhat unclear, there are empirical results which can be used to obtain a heuristic understanding of the process. Havnes and Næsheim (2007) was the first to recognize the importance of secondary charging effects in rocket probes. They concluded that the presence of MSPs inside mesospheric ice would alter the impact charging properties. Later works corroborated on that the secondary effect could be utilized to inquire about intrinsic properties of mesospheric aerosols – i.e. the effect is not necessarily only adverse (Havnes et al., 2009; Kassa et al., 2012). In Paper IV, the imperically obtained secondary charge yield is used to estimate the sizes of aerosols measured in DUSTY. As discussed in section 4.1, the MUDD probe is designed in such a way that it maximizes the secondary charge yield. This allows for detection of MSPs embedded in ice particles and can furthermore be used as a control of DUSTY measurements.

Chapter 4

The MAXIDUSTY Sounding Rocket Project

The MAXIDUSTY sounding rocket project (MXD) was initiated in 2012 by principal investigator Ove Havnes, with the aim to make detailed in-situ measurements of the Earth's polar mesosphere. The project comprised two sounding rocket launches, from hereon referred to as MXD-1 and MXD-1B. The two rockets had identical core payloads, based on dust detectors from UiT and accompanying electron density probes from the University of Oslo and TU Graz. MXD-1 and MXD-1B were launched from Andøya Space Center (69.29°N, 16.02°E) at 09:43 UT on 30 June 2016 and 13:01 UT on 8 July 2016, respectively. In Table 4.1, we present an overview of all instruments included on the MXD payloads. The UiT instruments, all relying on direct influx of dusty plasma, occupied the majority of the top deck of which the geometry is described in detail below. Apart from the 4D Space Module, which suffered from a malfunction during accerelation phase, all instruments returned data. Moreover, the main detector plate of the miniMass dust spectrometer was influenced by photoelectrons, and unambiguous results are difficult to extract from the data. The campagin ran with continuous radar support from the 53.5 MHz MAARSY radar (PI Ralph Latteck, IAP Kühlungsborn; see Latteck et al. (2012)) and the RMR-lidar at the ALOMAR observatory (see e.g. Von Zahn et al. (2000); Baumgarten et al. (2010); Fiedler et al. (2017)). These remote measurements were instrumental in the pre-launch phase for the launch decision.

The top deck geometry of the second payload, MXD-1B, is shown in Figure 4.1. The layout on the 1B-payload was almost identical to that of MXD-1, apart from the CU Boulder dust mass spectrometer miniMASS replacing DUSTY-2 (which is labelled in the sketch). Acronyms for the instruments are listed in Table 4.1, where the SRADS (Sounding Rocket Attitude Detection System) sun sensors cor-

Table 4.1: Instruments launched during the MAXIDUSTY campaign. The listed references present the instrument designs and/or theory applied to derive the corresponding plasma parameter.

	Instrument	Measured Parameter(s)	Owner†	Concept Reference
MXD-1	1 x DUSTY	Dust charge number density	UiT	Havnes et al. (1996)
	3 x Multiple Dust Detector (MUDD)	Primary/secondary ice/MSP current	UiT	Antonsen and Havnes (2015)
	Identification of the Content of NLC particles (ICON)	Neutral mass spectra of aerosol vapour	UiT	Havnes et al. (2015)
	Multiple Needle Langmuir Probes (mNLP)	Electron density	UiO	Jacobsen et al. (2010)
	Faraday Wave Propagation	Electron density	TUG	Jacobsen and Friedrich (1979)
	Positive Ion Probe (PIP)	Ion density	TUG	Blix et al. (1990)
	Capacitance Probe (CP)	Relative electron density	TUG	
	Attitude Monitoring (SRADS)	Attitude	UiO	Bekkeng (2007)
	Mesospheric Aerosol Sampling Spectrometer (miniMASS)	Aerosol/Ion mass spectra	CUB	Robertson et al. (2009)
	Side-looking NLC photometer	Optical scattering at 220 nm	SU	Gumbel and Witt (2001)
MXD-1B	2 x DUSTY	”	”	”
	3 x Multiple Dust Detector (MUDD)	”	”	”
	Identification of the Content of NLC particles (ICON)	„	”	”
	Multiple Needle Langmuir Probes (mNLP)	„	”	”
	Faraday Wave Propagation	”	”	”
	Positive Ion Probe (PIP)	”	”	”
	Capacitance Probe (CP)	”	”	”
	Attitude Monitoring (SRADS)	”	”	”
	Mini Fluxgate Magnetometer (MFM)	Magnetic field strength/orientation	UA	Miles et al. (2016)
	4D Module – Daughter Payloads	Electron density, magnetic field	ASC/UiO	

† UiO – University of Oslo, TUG – Techical University Graz, CUB – University of Colorado Boulder/LASP, SU – Stockholm University/MISU, UA – University of Alberta, ASC – Andøya Space Center

responds to 'DSS' shown in the figure. The MXD top deck layout presents a few important 'firsts' in the field of in-situ studies of the mesopause;

MXD-1B has two mechanically and electrically identically DUSTY Faraday buckets with an interspacing of $\sim$ 10 cm centre to centre. This is shorter than the characteristic dimension of the payload ram pressure bow shock, which is proportional to the top ram direction cross section diameter – $\propto d_{ram} \sim 35$ cm. This allows for rapid measurement of horizontal scales shorter than what to our knowledge has been done earlier. These measurements have the potential to reveal much information about the orientation of the smallest dust structures, comparable in size to the Bragg-scales of UHF coherent echoes. In addition, the small-scale horizontal measurements are extremely useful in quantifying the importance of adverse aerodynamic flow effects for direct influx dust probes. Preliminary results from MXD-1B show that the recorded currents of incoming dust was strongly varying between the two probes. This can probably be interpreted in that way, that aerodynamic adverse effects play a more important role than expected, at heights close to the mesopause. Moreover, it shows that aerodynamic effects can cause virtual horizontal density variations which can be, and probably have been in the past, interpreted as real 'transient' dusty plasma structures. This point forms the basis of Paper III, and is furthermore introduced in greater detail in section 6.

The MXD payloads also included the first high resolution sweeping neutral mass spectrometer (ICON) to probe the Earth's upper atmosphere. The ICON instrument is presented in section 4.1.

The triplet of MUDD Faraday impact cups on the two payloads allowed for the first measurement of the mesospheric ice particle fragment size distribution. As argued in in Paper I and Paper II, the fragment size distribution is probably directly related to the size distribution of MSPs embedded in ice particles. MSPs are also found in the latter of these two papers to be abundant inside ice particles as predicted by Havnes and Næsheim (2007).

A render of the assembled MXD-1 payload is shown in figure 4.2, below. A photo of the flight ready MXD-1B top deck is also shown in figure 4.3.

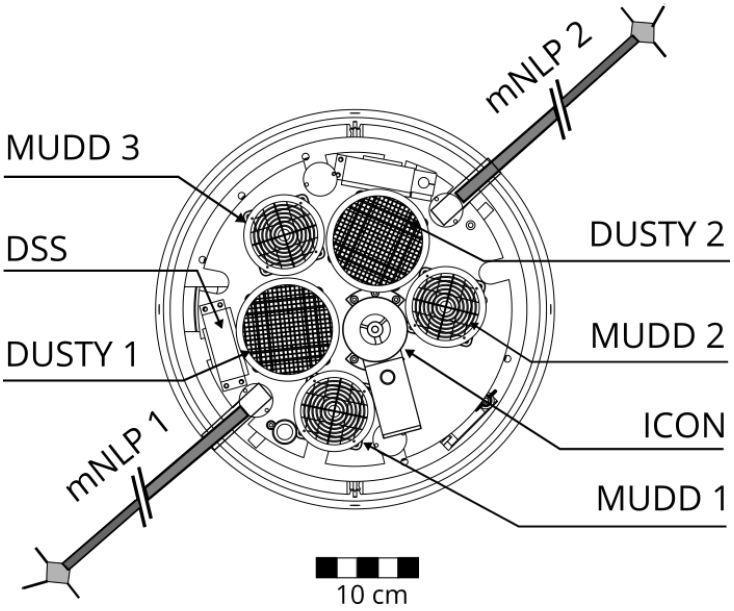

Figure 4.1: Top deck layout on the second MAXIDUSTY payload. The MUDD and DUSTY probes are the Faraday buckets from UiT. The first payload was mechanically similar but with one of the DUSTY probes replaced with the UC Boulder miniMASS. Reproduced from Antonsen et al. 2018 (Paper III), ©Copernicus.

Figure 4.2: Photorender of the MXD-1 payload with all instruments mounted. The additional yellow antennae are the Faraday rotation expertiment, while the spherical probe booms are PIP and capacitance probes.

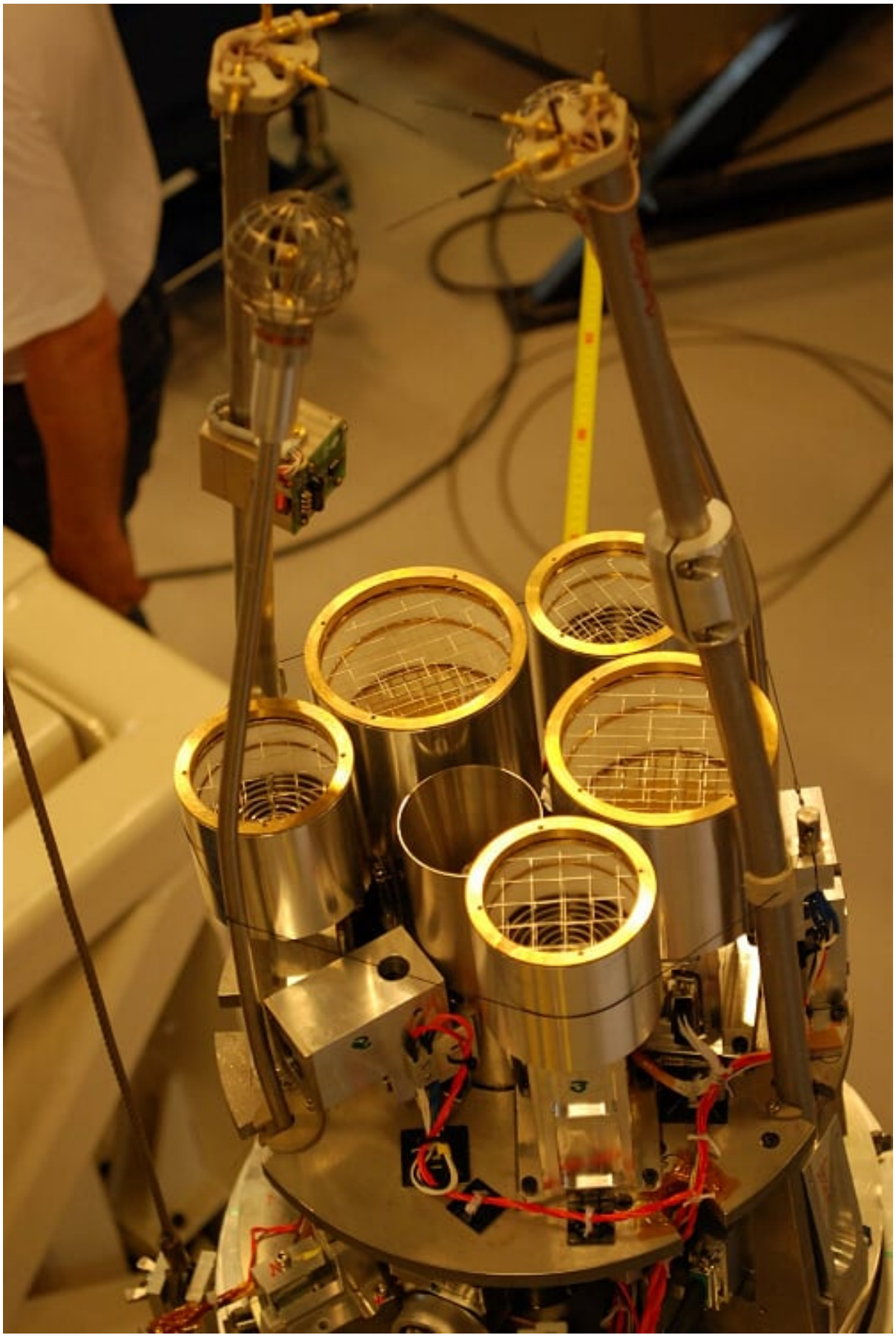

Figure 4.3: Photo of the MXD-1B topdeck displaying all Faraday cups, ICON, mNLP booms, PIP and Capacitance booms and Faraday antennae. Courtesy of Sveinung Olsen, UiT.

4.1 Instrument Principles, Design and Development

DUSTY

The DUSTY probe is fundamentally a Faraday cup – traditionally used to detect free ions and electrons in a vacuum. By choosing suitable biases on a set of detector and deflector grids, the probe can be made to detect particles in a certain energy range. By altering the grid biases, one alters the detection limits, and the probe essentially becomes a spectrometer since high biases will shield particles with low energy and vice versa. Introduced by Havnes et al. (1996), the DUSTY probe produced the first in-situ measurements of charged dust in the Earth's mesosphere. The design has through many sounding rocket flights through the last couple of decades proven to be a reliable way to measure the number charge density of dust, and the basic design has changed relatively little throughout this time.

A cross-section of the DUSTY probe with its grid biases is shown in Fig. 4.4. We show the principle of current generation in DUSTY in figure 4.5. The top grid is biased at the payload potential in order to shield neighboring probes from internal electric fields. The grid G1 is biased at +6.2 V, such that ambient ions (of energies on the order of ~ 0.01 eV) will not be able to penetrate. Ambient thermal electrons will be absorbed. The G1-potential is such that even with a few volts of payload charge due to secondary charging during upleg, ambient plasma particles are shielded effectively. The G2-grid was originally intended to absorb secondary electrons ejected from the bottomplate (BP), to correct for this loss in the derivation of the dust charge number density (Havnes et al., 1996; Havnes and Næsheim, 2007). From the first observations and theoretical considerations, however, the secondary production at G2 was found to be the dominating secondary charge source and no detectable secondary charge production takes place at BP. As it turns out, this finding facilitates the utilization of DUSTY to measure dust sizes and absolute number densities of dust particles; which is the main topic of Paper IV.

As discussed in the previous chapter, both pure ice and meteoric particles of sizes $\lesssim 1-2$ nm are influenced by air flow around the probe (see e.g. Hedin et al. (2007); Antonsen and Havnes (2015); Asmus et al. (2017) for recent works discussing this). For the DUSTY measurements on MAXIDUSTY, we have therefore assumed that these particles contribute little to the total dust number density.

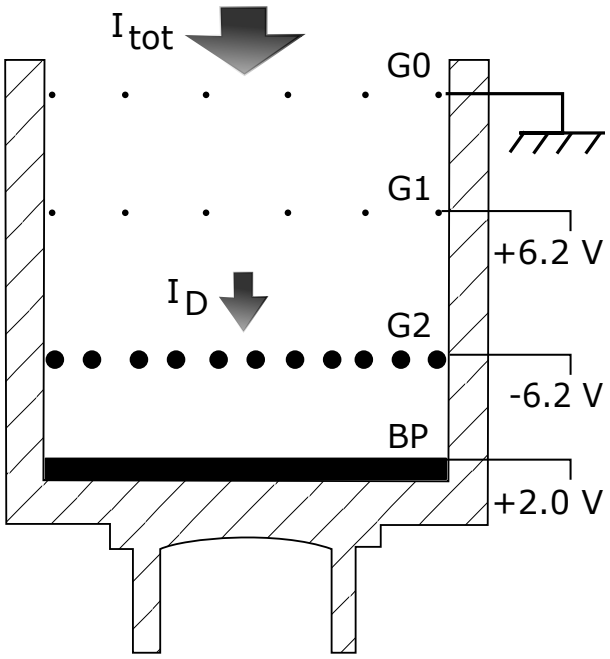

Figure 4.4: Cross section of the DUSTY probe as launched on the MXD payloads. The upper grid is payload ground intended to shield neighboring probes from internal electric fields. The Grids G1 and G2 and the bottom plate (BP) have potentials optimized to shield ambient plasma and detect mesospheric dust and ice particles.The wire thickness is exaggerated there for convenience, and we also note that the G2 wires are thicker that the G1 and shielding grid wires.

This assumption is also justified by the notion that very small particles can be neutralized effectively by photodetachment during sunlit conditions, as demonstrated in the calculations in chapter 2.3. Including the secondary current (I_{sec}, in the following), the currents to grid G2 and BP due to dust particles can be expressed as:

$$I_{G2} = \sigma I_D + I_{\text{sec}} \tag{4.1}$$
$$I_{BP} = (1 - \sigma) I_D - I_{\text{sec}} \tag{4.2}$$

where I_D is the current between G1 and G2 as shown in Fig. 4.4, and $\sigma = 0.235$ is the effective area factor of G2. We can furthermore express I_D in terms of the dust charge density $N_d Z_d$ accordingly:

$$I_D = (1 - \alpha) N_d Z_d e v_R \pi R_p^2 \cos\gamma \tag{4.3}$$

where v_R is the rocket speed, e the elementary charge, R_p is the probe radius, γ is

the coning angle and $\alpha = 0.08$ is the fraction of the probe area covered/shadowed by G1 and G0. Here we have neglected any secondary production of charge at G1, which is justified by that the effective area of G1 is only 4.6 %, which gives a secondary production area of 1.3 % of the total area; around five times smaller than that of G2. We note however, that the iteration procedure introduced in Paper IV takes into account the G1 secondary production. It has been found from laboratory measurements that the contribution of secondary currents to G2 is positive during the first few minutes of exposure to ice particles, meaning that dust particles rub off electrons from grid wires in a triboelectric fashion (Tomsic, 2001). This effect requires a grazing angle of around 80 to 85 degrees to be maximized, if the particles are pure ice (Tomsic, 2001). Note also, that combining equations (4.1) and (4.2) yields $I_D = I_{G2} + I_{BP}$, as expected.

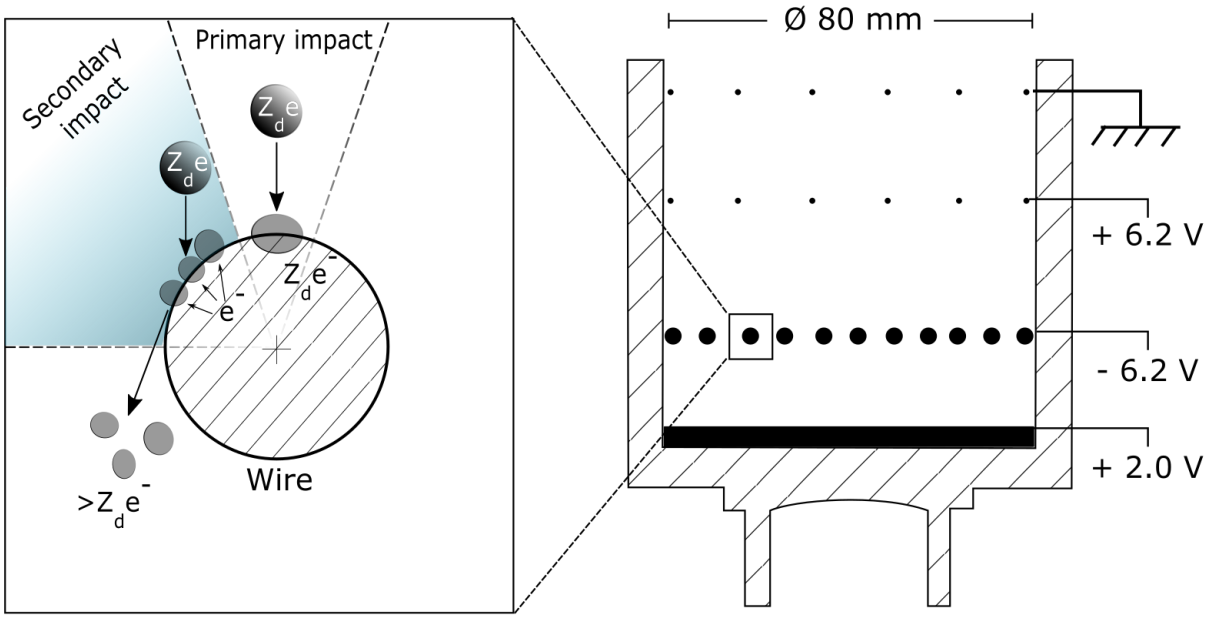

Figure 4.5: Principle sketch of large, order of 10 nm, particles entering DUSTY as launched on the MAXIDUSTY payloads. The mechanism can be described as follows: (1) A large particle deposits its charge in a primary impact and is partly fragmented, (2) If the impact is grazing, fragments can steal electrons from the grid wire. For large particles, the fragments tend to take away more electrons from the wires than the incoming charge and the net current to G2 becomes positive. For small particles, the primary charge is usually larger than the fragment current, and the net current to G2 thus becomes negative. In both cases, the bottom plate current becomes negative. We note that the secondary impact area region is exaggerated here; the true secondary charge producing area is $\gtrsim 20\%$. Adapted from Paper III, Copyright © Copernicus.

MUDD

The *MUltiple Dust Detector* – MUDD – is an impact Faraday cup with two grids biased at stationary voltages and a bottom plate detector stepping between different voltage biases sequentially. The term *impact* here refers to the mechanism which takes place on a special impact grid (G2), which is constructed in such a way that all incoming aerosols will collide with it. A sketch of MUDD with grid labelling is shown in figure 4.6.

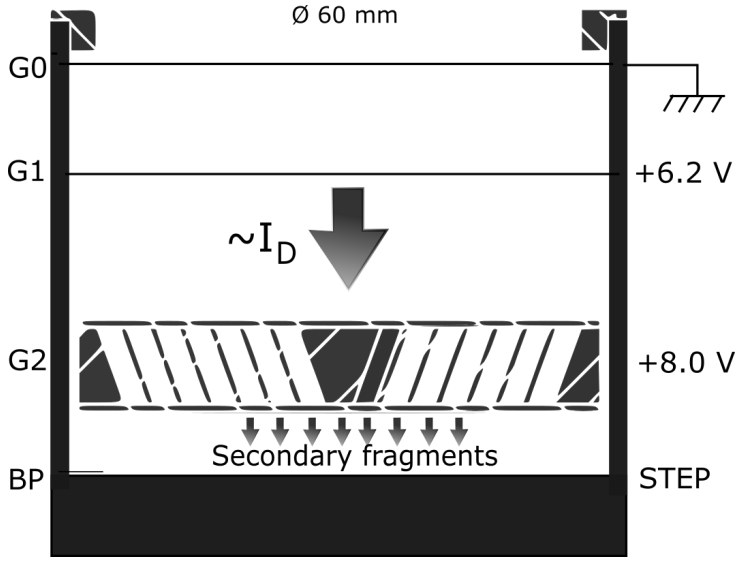

Figure 4.6: Cross section of the MUDD probe as launched during MXD. The current above G2 is analogous to the current I_D in Fig. 4.4, only with a difference due to different collecting areas. The G2 grid consist of overlapping concentric rings which implies that all primary particles hit a surface there. The G0, G1, and G2 grids have constant biases, while BP steps between different voltages every 192 samples ($F_s = 8680$ Hz) to produce the retarding potentials for detection of particles of different sizes. A single MUDD probe has three unique voltage modes and one mode that overlaps with one of the other probes for comparison and calibration. A triplet of three MUDD probes can produce a 10-point size distribution of fragments/MSPs with a height resolution of $\sim$ 100 m.

For MUDD on the MXD payloads, the G0 and G1 grids were constructed from .25 mm silver wire; in total 10 wires with five and five crossing each other perpendicularly, constituded one grid. The cross-section of these uppermost grids was 0.046 times the full cross-section of the probe. As illustrated in the principle sketch, G0 only acts as a shielding grid and is connected to payload ground and current to it is not recorded. G1 was biased at +6.2 V to shield ambient plasma. Currents were measured at G1, G2 and BP, with a noise level on the order of 1 pA for G2 and BP and an order of magnitude higher for G1 (due to amplification).

The G2 grid is what separates MUDD from a traditional Faraday cup, and the

reason why the probe is referred to as *an impact Faraday cup*. It is constructed from a number of concentric stainless steel rings with an interspacing such that no free through flux can occur[1]. The conclusion from experimental studies of nanoscale ice particles colliding on graphite and gold surfaces, is that large particles partly fragment even at low speed impacts with metal surfaces (see e.g. the works compiled in Tomsic (2001)). At an inclination of $\sim 75-85^{\circ}$, the secondary charge transfer – likely a triboelectric transfer of electrons from the grid to a ice particle fragment – is found to have a maximum. Ice particles of size 50 nm have been found from rocket measurements to produce on average $\sim 50-100$ charged fragments upon impact with the grids in Faraday cups (Havnes and Næsheim, 2007; Havnes et al., 2014; Antonsen et al., 2017). MUDD is designed to maximize, or rather guarantee, this secondary amplification of the particle current.

The bottom plate detector (BP) steps between four different voltages in order to separate fragments/particles of certain energies. On MXD-1 and MXD-1B, we combined three MUDDs with in total 10 unique BP voltages. In fact, we utilized 12 voltages of which two were overlapping in order to calibrate the probes respectively to each other in-flight. On MUDD-1 and MUDD-3, this overlapping channel had a positive bias two volts lower than that of G2, such that all particles, including possible leakage currents, were recorded. These channels are throughout the dissertation assumed to measure the total current of all incoming fragments. The stepping of the BP voltage was done every 192 samples, which with a 8680 Hz sampling rate implies that a 10-point (relative) size distribution of fragments and particles produced at G2 can be obtained at a height resolution on the order of ~ 10 m. A sketch of how the potentials step on each of the three MUDD probes flow on MXD-1 and 1B is shown in figure 4.7. As shown in Paper II, with filtering and processing, the final height distribution of fragments has a resolution of ~ 100 m.

Verification of the MUDD Secondary Currents

The secondary charging effect in MUDD can be utilized to obtain information about the volume content of MSPs inside larger ice particles – as was one of the main intentions of the design. To justify this claim, a disucssion of both theoretical and experimental inquiries is necessary. The conclusion from extended discussions on this reasoning in Paper I and II, is that the MUDD BP currents *are* indeed dominated by pure MSPs, and can furthermore be used to obtain the

[1] Very small particles *can* indeed in some cases follow the airflow and avoid direct collision with G2, but this is rarely applicable for the cases of interest in this dissertation

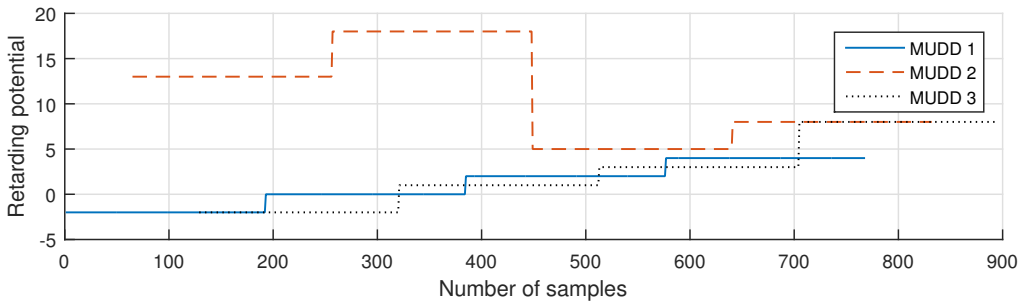

Figure 4.7: Stepping scheme of the different retarding potential modes for all MUDD probes. Note that the modes are slightly shifted in time relative to each other and the overlap between probes at retarding potentials −2 V and 8 V. The sampling frequency is 8,680 Hz, implying that a group of four steps, or 768 samples, takes ∼ 0.09 s to complete. From Paper I.

volume content. The key controlling parameter of the estimate of the volume content is the dependence of particle radius in the impactor charging probability. As shown in Paper II, the charging probability of pure MSPs is probably proportional to r_d^{-k} for k between 2 and 3, i.e. a proportionality between the cross-section and mass of the particle.

Above we claimed that a 50 nm dirty ice particle produces around 50 to 100 elementary charges at G2 which are subsequently recorded at BP. Another claim was that the charging probability, or rather the affinity to produce current, was propotional to the cross-section or mass of a particle. With the new method to derive sizes and densities of ice particles with Faraday cups presented in Paper IV, we can control these claims. We use the aerosol neutral density, N_d, and the ice particle radii, R_d, from the iteration of DUSTY data. The current produced at a grid, which is to say the effective collecting area is the probe cross-section, is as usual calculated as:

$$I = eN_d \pi R_P^2 v_R \eta_{50} \left(\frac{R_d}{50} \right)^{\alpha_C} \cdot \frac{1}{10^{-9}} \tag{4.4}$$

where e is the elementary charge, R_P is the probe radius, η_{50} is the reference number of elementary charges produced for a 50 nm particle and α_C is the proportionality exponent of the charging probability (i.e. $\alpha_C = 2$ for cross-section). To compare the secondary current in DUSTY to the true secondary current observed by MUDD, we let η_{50} be 50 elementary charges and α_C be 2. The densities and radii are estimated from DUSTY as shown in Paper IV. The resulting current is shown as a solid blue line in figure 4.8 while the true secondary currents are shown in red (MUDD 1) and orange (MUDD 3). The striking similarity reveals

a few important things: (1) The collision mechanisms producing secondary current is very similar in MUDD and DUSTY, (2) The method presented in Paper IV is justified, and (3) The assumed charging probability and reference secondary production factor fits well for the data shown here. As the critical reader will point out, there will be other (infinitely many) combinations of parameters which can produce the same plot. However, the present calculation should be regarded as highly plausible as it is based on the present knowledge about nanoscale ice particles and the reliable DUSTY probe.

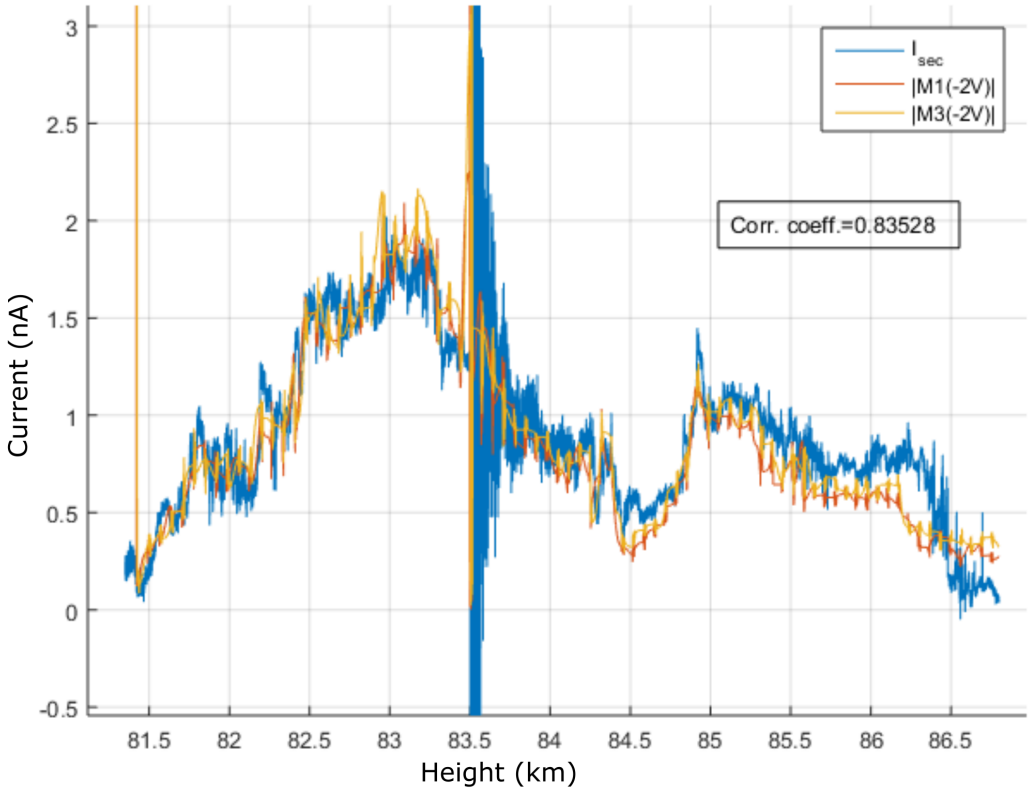

Figure 4.8: Test of the assumption that the secondary charging from ice particles at G2 in MUDD is proportional to cross-section, and that a 50 nm particle produces on average 50 elementary charges. The correlation is striking everywhere but at the very top of the cloud system.

Simulations of Particle Trajectories Around MUDD

Utilizing the theory outlined in section 3.1, we have developed a code which can be modified to calculate the trajectory of aerosols in any geometry in two or three dimensions. The code was used in Paper I to find the detection limits in MUDD and in Paper II to estimate the sizes of the particles producing current

to the bottom plate in MUDD. In the top panel of figure 4.9 we show an example simulation for a rotationally symmetric flow with zero instrument coning at an altitude of 70 km. The reason for this low altitude (lower than summer mesospheric clouds) is to study the possibility of detecting free aerosols (MSPs) with sizes below one nanometre with Faraday cups. As also mentioned in chapter 7 regarding future work, by using a modified *open* version of the MUDD, it is possible to detect free MSPs. In the example simulation shown below, all particles of sizes 0.5 nm are stopped in the upper part of the probe. For an open version of the probe (SPID = Smoke Particle Impact Detector), the detection efficiency improves dramatically.

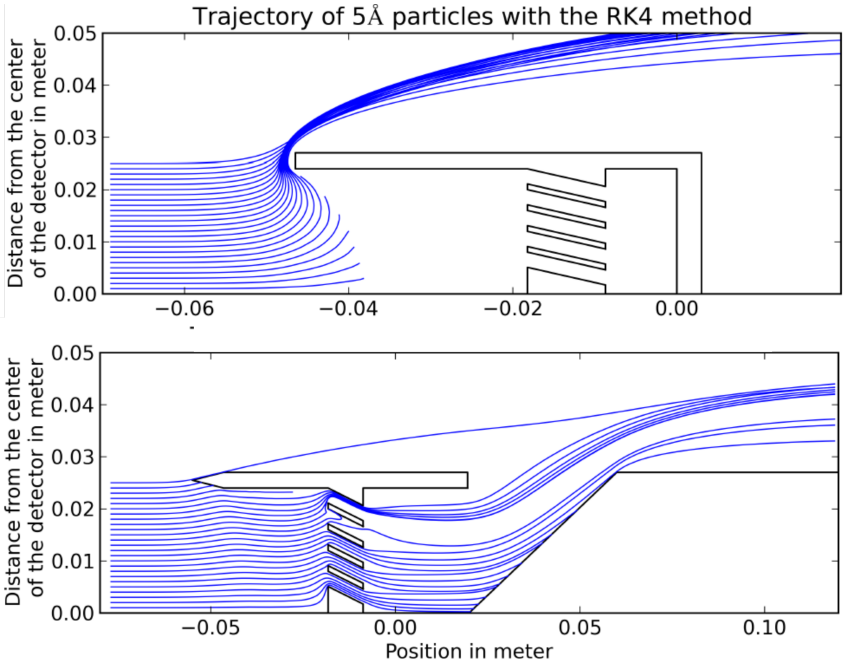

Figure 4.9: Comparison of particle flux to the closed MUDD probe (top panel) and open SPID probe (bottom panel) of 0.5 nm free neutral MSPs in the winter mesosphere at an altitude of 70 km.

ICON

As established above and proven by independent means of measurement, ice particles constituting noctilucent clouds contain meteoric smoke. In addition to molecules from smoke particles, metals such as Na, K and Fe from differential ablation of meteors are also present in their atomic form inside ice particles (Lübken and Höffner, 2004; Plane, 2004; She et al., 2006). In order to investigate whether or not the chemical composition of such atomic species and MSPs embedded in ice particles could be analyzed in-situ, the Tromsø-group have developed the Identification of the COntent of NLC particles probe (ICON); see e.g. Havnes et al. (2015). The ICON probe is the first instrument to employ a neutral quadrupole mass spectrometer for investigation of mesospheric aerosols.

Figure 4.10 shows a render and working principle of ICON. The funnel is utilized to focus and concentrate the inflowing NLC particles which are subsequently gathered and evaporated in front of the pinhole. The pinhole has an aperture of 75 micron and is kept shut by a springloaded valve until the payload is inside a cloud. A residual gas analyser (RGA) inside the ICON chamber has a mass resolution of 0.1 AMU, and can be operated in both sweeping mode and for single AMU measurement. During MAXIDUSTY, ICON was launched on both the MXD-1 and the MXD-1B payloads. On these flights, both probes were operated in a sweeping mode. ICON-1 was swept from 15 to 73 AMU in $\sim$ 4.3 seconds, and ICON-1B was swept from 15 to 56 AMU in $\sim$ 3.0 seconds. For both flights, the focusing potential was set to -15 V, while the ionizing source was calibrated to water at 70 eV and 2.0 mA current. An electron multiplier at 1.01 kV was used for amplification. With these operating parameters and a chamber pressure on the order of $10^{-7} - 10^{-5}$ mBar, the detection limit of a single AMU in terms of partial pressure was between 10^{-11} and 10^{-12} mBar. With these settings, the aim is to measure the water vapour from NLC particles and traces of meteoric material.

The ICON is a UHV system, and carefully balancing the operating parameters is necessary in order to detect the vanishingly low concentrations of atoms from meteoric ablation. For the RGA to function with best possible dection limit, the pressure must be low, however not too low as that would render the meteoric atoms and molecules undetectable. For ICON, the ideal stand-by pressure is $\sim 10^{-7}$ mBar. Traditionally, ion spectrometers have been combined with cryogenic pumps to keep low enough background pressure (see e.g. Schulte and Arnold (1992)), but as such systems are complicated to maintain and run and relatively expensive ICON uses an ion getter pump. The ion pumps require high voltage on

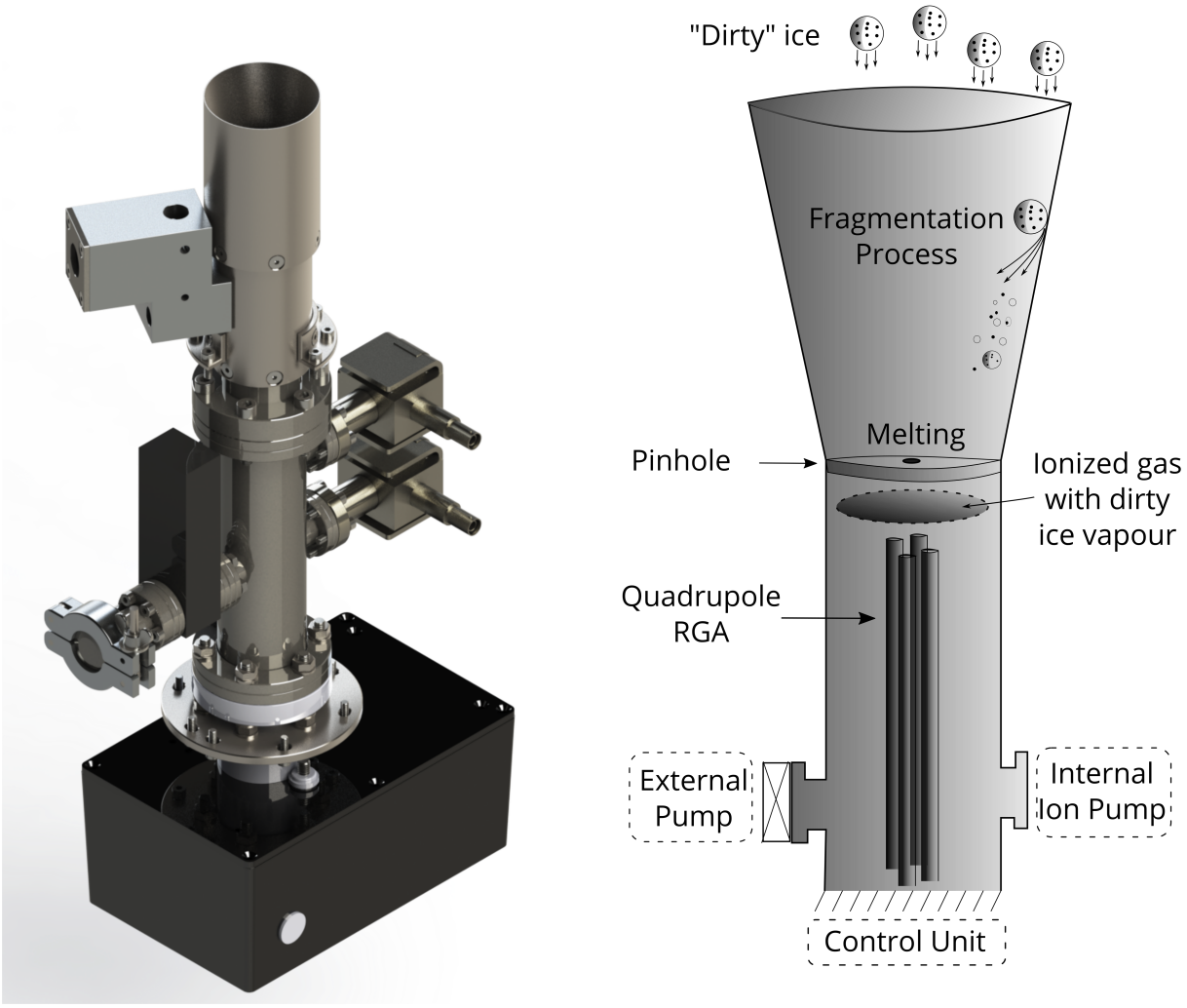

Figure 4.10: Principle sketch and rendered image of the ICON probe as flown during the MXD campaign. Due to the RGA requiring a low working pressure of $\lesssim 10^{-3}$ mBar, the probe has both internal and external pumping ports. All flanges utilize copper gaskets, except the mounting flange for the funnel, where Viton gaskets were used. Despite this, the ultimate pressure of the system was on the order of 10^{-7} mBar.

the order of 1000 V, but are small and easy to install. Moreover, ion pumps can measure the pressure of a chamber as their current is directly proportional to the number density of neutrals. In figure 4.11 we show a comparison of the pressure profiles measured with a Pirani gauge at different ambient pressures, simulating the pressure in front of the ICON pinhole at different altitudes. Combining these profiles yield a detailed picture of how the background pressure inside ICON develops during operation which is necessary for later analysis of MXD data. Importantly, the pressure remains well below a level where the collisional length becomes too short. Note that for these tests, the initial pressure *inside* ICON is not very defining for the characteristic rise time of the pressure due to the logarithmic scaling.

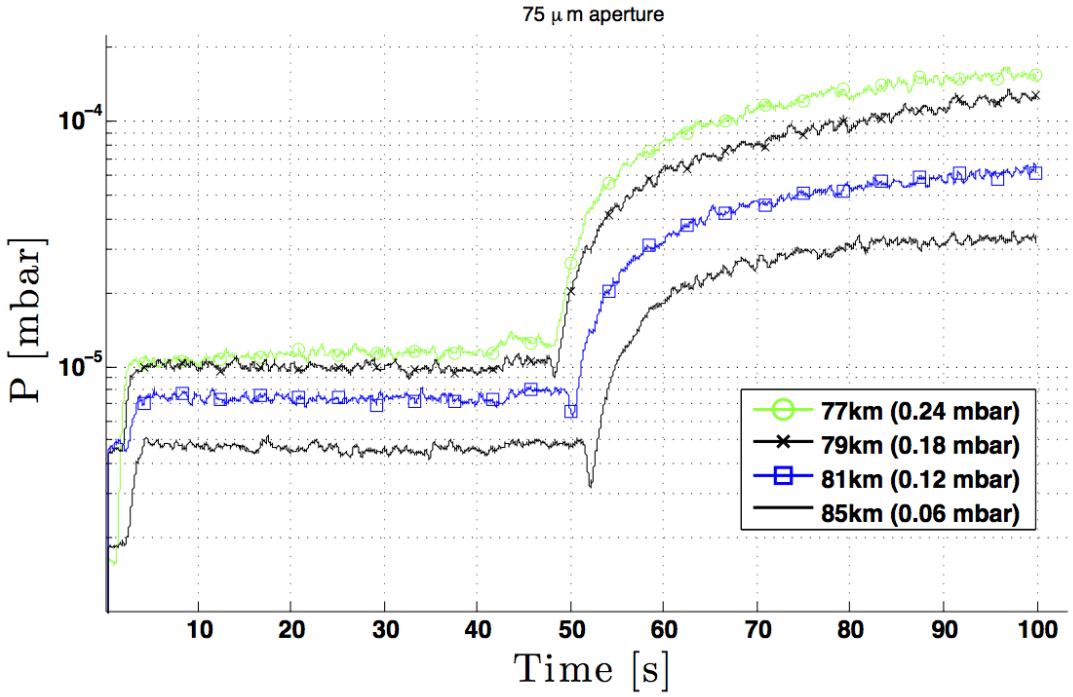

Figure 4.11: Laboratory measurements of pressure increase inside ICON chamber at different ambient pressures for an aperture diameter of 75 μm.

In figure 4.12 we show a reference sweep from ICON in both sweep and trend mode. The seemingly periodic variation over groups of $10-15$ AMU are probably contamination from pump oil or hydrocarbons deposited on the stainless steel walls during bakeout.

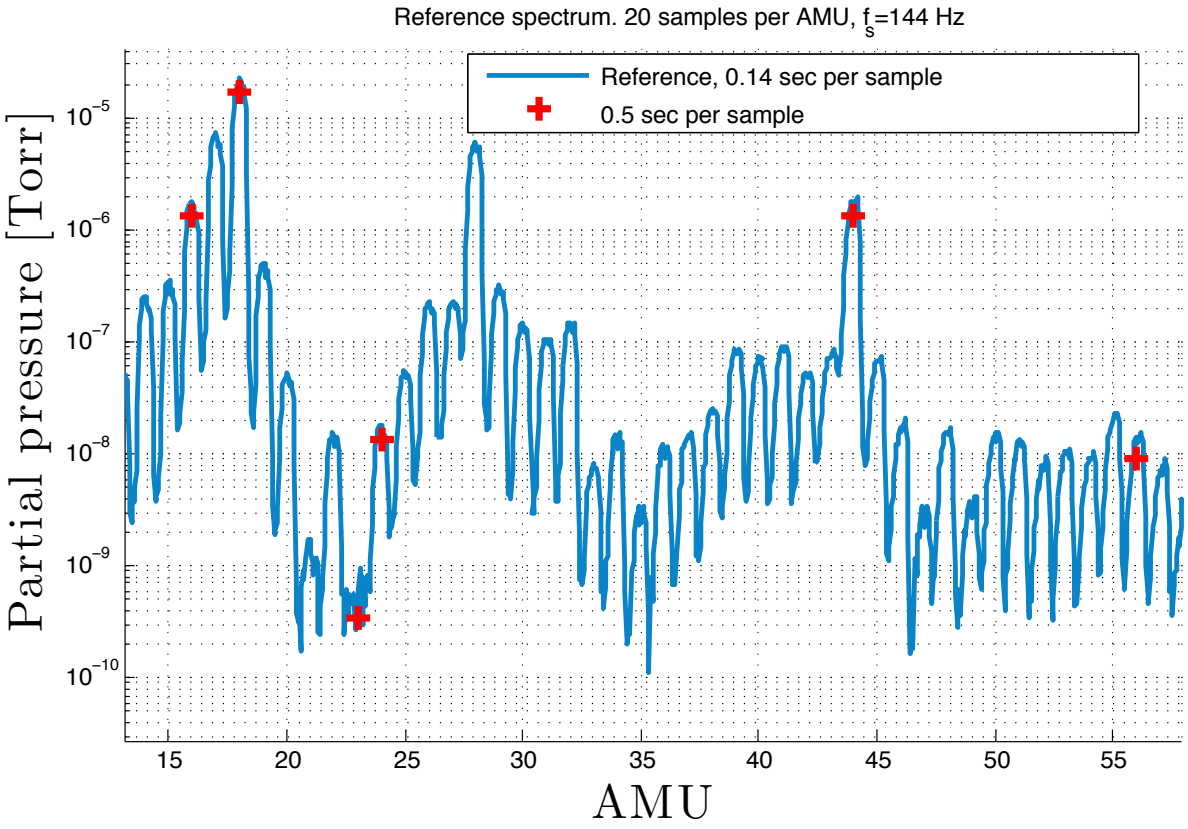

Figure 4.12: Reference spectrum of the first 56 AMUs in the ICON-I prototype comparing sweep and trend settings. The trend setting have much longer integration time and normally offers higher accuracy. In this plot it may be an artifact that there is an underlying variation with period 10-15 AMU; this can normally be attributed to hydrocarbons from pumping oils or bake-out of the stainless steel chamber. 1 Torr here is approximately 1 mBar/1.33. The electron multiplier was turned off in this test.

Chapter 5

Size Distribution of Mesospheric Dust Particles

One of the main developments included in the present thesis is the estimation of sizes of mesospheric aerosols with Faraday type cups. In Paper II we estimated the sizes of collision fragments of ice particles with the MUDD probe, which is argued to be representative for the size distribution of MSPs. In Paper IV we introduced a method to calculate the sizes and neutral density of mesospheric ice particles, by means of solving coupled equations for the dusty plasma with number charge density derived from DUSTY. This method has an advantage from optical methods in that it yields currently unmatched height resolution on the order of 10 cm. The methods are fundamentally different, and the extended DUSTY method from Paper IV yields mean absolute values of particle radii and density while the analysis in Paper II yields a relative size distribution. In this chapter we give a short introduction of sizes of mesospheric nanoparticles and the theoretical justification for the two methods used to derive particle sizes from data obtained during the MAXIDUSTY campaign.

5.1 Sizes and Growth of MSPs

Re-condensation of meteoric vapours have been considered in a handfull of works since the initial postulation by Rosinski and Snow (1961), that atomic metal from ablation can be oxidized by ambient O_2 and the metal oxides subsequently coagulate into nanoscale particles – or as they are addressed here *meteoric smoke particles*. Due to the low vapour pressures of many metal oxides in the upper mesosphere, where the temperature is very low, two colliding molecules can combine without an energy barrier. Hunten et al. (1980) presented the most well knowm coupled calculation of ablation profiles and MSP sizes; their pro-

duction rates are readily used, even today. In recent years, whole atmosphere models like WACCM have been coupled with microphysical models and a more complete parameterization of the transport of aerosols, like CARMA (see e.g. Megner et al. (2006) and Bardeen et al. (2008)). Surprisingly, the size distributions obtained by the most recent methods are very close to the original work by Hunten et al. for the low end of the size spectrum. Figure 5.1 shows a comparison of the two mentioned simulations using the CARMA model, where the discrepancy is found to grow with particle size. Such a discrepancy is mainly due to how large scale transport and turbulence is parameterized. In the following, we introduce the theory of MSP growth and size distributions from the simplest principles, i.e. no parametrization of complex transport patterns and gravity wave breaking. Subsequently we discuss how the sizes of MSPs inside larger ice particles can be obtained using MUDD.

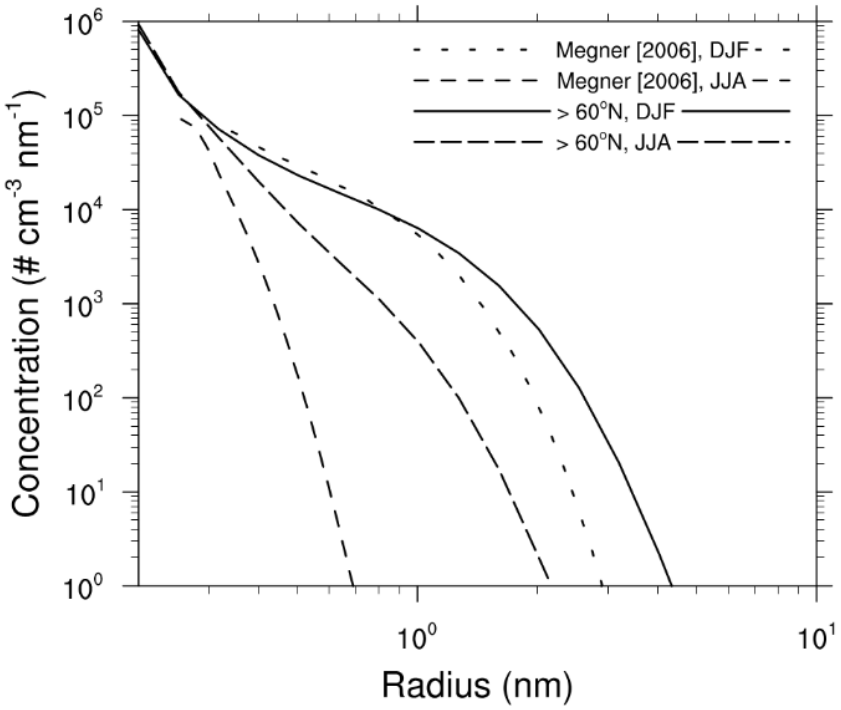

Figure 5.1: Comparison of the mean MSP size distributions obtained by two-dimensional Megner et al. (2006) and three-dimensional(Bardeen et al., 2008) whole atmosphere simulation of meteoric smoke with the CARMA code for altitudes between 80 and 90 km. The results of these simulations gave similar inverse power laws (in order of magnitude) as the original work by Hunten et al. (1980); $N_{MSP} \propto r_{MSP}^{-2.5}$. Adapted from Bardeen et al. (2008) © Wiley.

It can be assumed for a range of probable constituents of meteoric smoke particles, that they must to a large degree have been nucleated homogeneously. One simple justification of this, is that metal oxides and non-stoichiometric molecules

from ablation of olivine can be expected to have a relatively large dipole moment. Thus, homogeneous nucleation can take place without an energy barrier; three-body reactions with the other species can also take place. In the following, we examine the theoretical size distribution arising from homogeneous nucleation from a finite reservoir of ablation gas.

The rate at which atoms or molecules strike the surface of a dust grain can be calculated by calculating the first order moment of the distribution function. We let n_γ denote the density of the ablation gas, and n_d the density of the dust (smoke) particles. Allowing for a specified sticking probability, ξ_d, we have:

$$\begin{aligned} \Gamma &= \xi_d \pi r_d^2 n_\gamma \int_0^\infty \mathrm{d}v \cdot v' f(v') \\ &= 4\pi r_d^2 n_\gamma \xi_d \left(\frac{k_B T_\gamma}{2\pi M_\gamma} \right)^{\frac{1}{2}} \end{aligned} \tag{5.1}$$

where M_γ and T_γ are the molecular mass and temperature of the ablation gas species, respectively. This rate is also the rate at which ablation gas molecules are removed. If we furthermore let $n_d(r_d, t)$ be the time-dependent number of grains of radius r_d, we can express the number of removed molecules of the ablation gas per time as:

$$\frac{\partial n_\gamma}{\partial t} = -4\pi r_d^2(t) n_\gamma(t) n_d(r_d, t) \xi_d \left(\frac{k_B T_\gamma}{2\pi M_\gamma} \right)^{\frac{1}{2}} \tag{5.2}$$

where we have emphasized the time dependency of the grain radius. The rate of mass increase is simply calculated from eq. (5.1) as $\dot{m}_d = \Gamma M_\gamma$. Given that a grain grows uniformly and spherically, we can also express the mass increase in terms of the radius increase as:

$$\dot{m}_d = 4\pi r_d^2 \rho_d \dot{r}_d \tag{5.3}$$

where ρ_d is the grain material mass density. Combining equations (5.1) and (5.3) we obtain an expression for the radius rate-of-change:

$$\dot{r} = \frac{n_\gamma \xi_d}{4\pi^2 \rho_d} \left(k_B T_\gamma M_\gamma \right)^{\frac{1}{2}} . \tag{5.4}$$

If we now formalize the above manipulations into a set of coupled PDEs we have,

for the simplest case with no additional sources or sinks:

$$\frac{\partial n_\gamma}{\partial t} = -4\pi r_d^2(t) n_\gamma(t) n_d(r_d, t) \xi_d \left(\frac{k_B T_\gamma}{2\pi M_\gamma} \right)^{\frac{1}{2}} \tag{5.5}$$

$$\frac{\partial r_d}{\partial t} = \frac{n_\gamma \xi_d}{\rho_d} M_\gamma \left(\frac{k_B T_\gamma}{2\pi M_\gamma} \right)^{\frac{1}{2}} \tag{5.6}$$

This can be solved numerically, but it is possible to find an analytical approximation of the final size distribution. Differentiating (5.6) and substituting for $\partial n_\gamma / \partial t$ we obtain

$$\ddot{r}_d = \frac{\partial^2 r_d}{\partial t^2} = -4\pi r_d^2 \bar{v}_\gamma \xi_d n_d \dot{r}_d = \dot{r}_d \frac{\partial \dot{r}_d}{\partial r_d}. \tag{5.7}$$

Solving this equation yields

$$\dot{r}_d = \frac{4\pi \bar{v}_\gamma \xi_d n_d}{3} \left(r_{d,\infty}^3 - r_d^3 \right) \tag{5.8}$$

where $r_{d,\infty}$ is the final size distribution of the grains and $\bar{v}_\gamma$ is the mean thermal speed of the ablation gass molecules. Assuming $r_{d,\infty} \gg r_{d,0}$ gives that the initial growth rate can be estimated as $\dot{r}(0) \approx 4\pi \bar{v}_\gamma \xi_d n_d r_{d,\infty}^3 / 3$. At this point in time, we can assume that the gas reservoir is not significantly depleted, such that the growth rate according to eq. (5.6) can be estimated to be

$$\dot{r}_d = \frac{n_\gamma \xi_d}{\rho_d} \left(\frac{k_B T_\gamma M_\gamma}{2\pi} \right)^{\frac{1}{2}}. \tag{5.9}$$

Equating the two yields an estimate of the final size distibution is terms of the initial density of ablation molecules, $n_{\gamma,0}$:

$$n_d(r_d)_\infty \simeq \frac{3 M_\gamma n_{\gamma,0}}{4\pi \rho_d} r_{d,\infty}^{-3} \tag{5.10}$$

demonstrating an inverse power law relationship. This inverse power law is steeper than the simulation results mentioned above which indicate a proportionality close to $n_d \simeq r_d^{-2.5}$ at 90 km. This levelling can happen due to a number of mechanisms, but is probably mainly due to the parameterization of eddies and updraft in the more complex models.

Sizes of MSPs derived from MUDD measurements

The justification for why sizes of MSPs can be estimated using MUDD is given in Paper II, and we will not go into depth on that here. The conlusion is that due to sticking of small ice particles to metal surfaces, increased evaporation and smaller affinity for triboelectric charge transfer, MSPs is likely to dominate the bottom plate current in MUDD.

As specified in chapter 4.1, a triplet of MUDD (as launched on MXD) has the capability of sweeping through all 10 potential potentials in a height range of some tens of metres. On such short spatial scales, there may be large natural variations in the dusty plasma. Noise and other adverse effects might also influence the currents. Therefore, to minimize error it is preferrable to integrate the MUDD currents over relatively calm regions. By doing so, however, there is some loss of information as the size distribution can change significantly at altidudes between $\sim$ 80 and 90 km.

Figure 5.2 shows the MUDD currents integrated over an arbitrary calm part of a cloud layer and subsequently normalized. Note especially, that there is one channel with 'retarding potential' of -2V, which means that it is attractive for negative particles, and therefore presumable collects all charged fragments. This channel is also taken as the total current channel, where all charged fragments are measured. The general trend is that channels of higher retarding potential records lower currents, as expected from the theorized distributions.

A size distribution cannot be derived directly from figure 5.2 due to the following: (1) Fragments detected in the most energetic channels will also be detected in channels of lower retarding potential, and (2) The secondary impact charging occuring at G2 varies with particle size. The solution to the first problem is simple; for a given channel, we extract the current in the channel with the immediate higher retarding potential. The second issue is far more complicated to overcome. It is probable, as discussed in Paper II, that the charging probability of fragments/MSPs produced in MUDD should have a proportionality to radius somewhere between r_d^2 and r_d^3. In figure 5.3 we present the estimate of the size distibution of collision fragments calculated using the two limiting values of charging probability. The slope of the upper confidence boundaries are close to the slope of the model predictions, but we find generally steeper power laws regardless of charging probability.

Above, we provided justification for that coagulation of a depleting reservoir of ablation gas resulted in an inverse power law size distribution proportional to

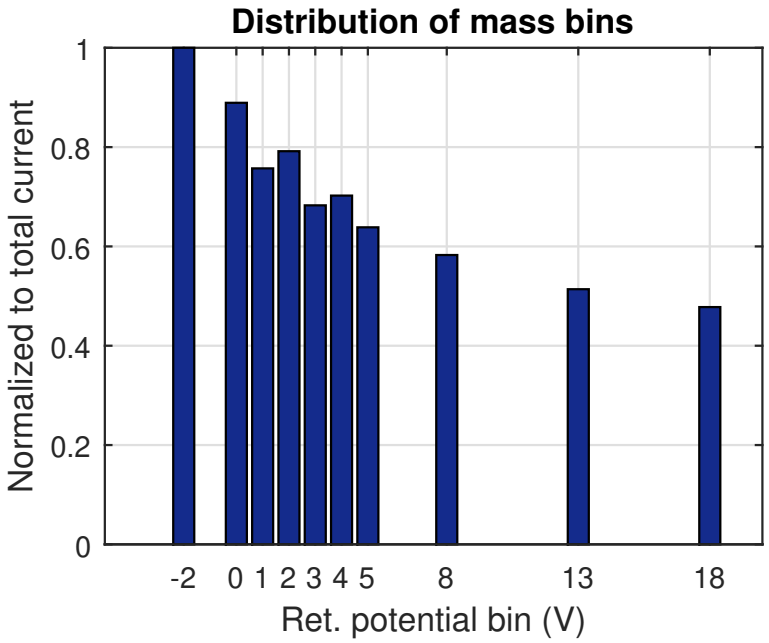

Figure 5.2: The accumulated and normalized currents for all channels (retarding potentials) on three MUDD probes in an arbitrary region of the cloud layer. This example is from the MXD-1 flight in a region with little observed variation and turbulence.

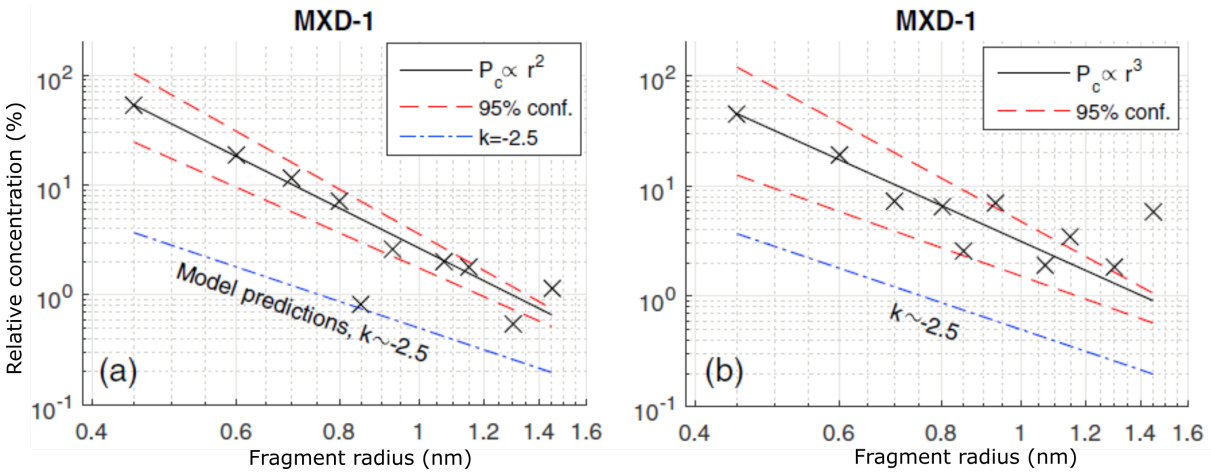

Figure 5.3: Final size distributions of collision fragments (MSPs inside ice particles) for the MXD-1 flight. The two panels show the case for two limiting values of charging probability (P_c) – either proportional to particles cross-section (panel a) or volume (panel b). The obtained distributions are plotted as solid black lines, and the red dashed lines provide the 95% confidence bounds. The blue dash-dotted lines shows a fit of modeled size distributions of free MSPs at 90 km based on Bardeen et al. (2008), Hunten et al. (1980), and Megner et al. (2006). Note that these are presented in relative terms and that the model prediciton line has been shifted down by approximately one order of magnitude for clarity.

r_d^{-3}, which is close to the values found with MUDD. We must also note however that certain collision mechanisms can yield the same proportionality, however, due to the thermodynamic and charging properties of nanoscale ice we maintain that the observed signature is due to embedded MSPs.

5.2 Sizes and Growth of Ice Particles

Due to the multiple phases of H_2O-clusters and high sensitivity to changes in temperature and saturation ratio, the nucleation and growth of ice particles is somewhat more complicated and more difficult to generalize than nucleation of meteoric smoke particles. A short introduction to nucleation theory is not adequate to give the physical insight needed to really comprehend the complex nature of mesospheric ice particles. There are, however, a few important concepts which should be introduced in order to understand how MSPs affect ice growth.

At this point, we should recall Ostwald's rule which paraphrased states that "[...] an unstable system prefers to transform into a state which is accompanied by the smallest loss of free energy, rather than to the most thermodynamically stable one" (Ostwald, 1897). This is to say that hexagonal ice – the most themodynamically stable state of H_2O-clusters – is not the most probable form under all conditions. It is possible to show that this is consistent with classical nucleation theory. The Gibbs free energy of forming a grain of i for a saturation ratio $S = p_{H_2O}/p_{amb}$ can be stated as (Pruppacher and Klett, 1997):

$$\Delta G = -\frac{4\pi\rho r_i^3}{3M} k_b T \ln S + 4\pi r_i^2 \gamma \tag{5.11}$$

where the first term on the r.h.s. is the free energy of forming internal bonds between water molecules. The last term on the r.h.s. is the free enregy connected to forming an interface, which is always positive (and therefore unfavourable). The molecular mass and initial state density is denoted by M and ρ respectively, and the energy interfacial energy is denoted by γ.

The critical radius of a grain, where effective growth can take place, is defined at the point where there is no change Gibbs energy when adding another molecule to the initial gain or cluster, i.e. $\mathrm{d}\Delta G/\mathrm{d}r_i = 0$. The critical radius is therefore

$$r^\dagger = \frac{2\gamma M}{k_B T \rho \ln S} \tag{5.12}$$

which finally yields the expression for the Gibbs energy of a critical cluster

$$\Delta G^{\dagger} = \frac{16\pi\gamma^3 M^2}{6\rho^2 k_B^2 T^2 \ln S}. \tag{5.13}$$

From this expression it is evident that that there is a strong dependence on interfacial energy. This shows, as argued by Zasetsky et al. (2009) and Murray and Jensen (2010), that Ostwald's rule applies since an amorphous state of water has a lower interfacial energy and thus a lower nucleation barrier than hexagonal ice. The consequence is that for homogeneous nucleation of ice, i.e. water nucleating with water, amorphous solid water have a more rapid growth than hexagonal ice if the water vapour is abundant.

The latter two cited works make the case for homogeneous nucleation of ice, but as pointed out by Murray and Jensen (2010) this is only possible at either very low temperatures, high saturation ratios and/or during periods of steep negative temperature gradients. Homogeneous nucleation happen to a certain degree during normal summer mesosphere conditions, and the question is whether or not (or when) homogeneous nucleation of ice can compete with heterogeneous nucleation with other mesospheric constituents. For a long time, molecules and agglomerates from meteoric ablation have been the most likely candidates for condensation nuclei of mesospheric ice (see e.g. Rapp and Thomas (2006)). The reason is that such particles can lower the nucleation barrier to virtually zero (Gumbel and Megner, 2009). As a matter of fact, there are now a few independent observations of meteoric smoke embedded in ice. Observations from the SOFIE mission on the AIM spacecraft estimated the meteoric smoke content to be up to 3% by volume (Hervig et al., 2012), while Havnes et al. (2014) and Paper II in the current work find similar volume contents. The two latter papers also point out that there is a strong dependence on charging efficiency of ice particle fragments; this is a process which MSPs can affect. Asmus et al. (2014), which provides a thorough introduction to growth of dirty ice, calculated the growth rates of ice with embedded smoke particles of different composition. Their finding was that MSP tend to cause larger but fewer grains, and the growth is strongly dependent on iron content in the smoke. Based on the discussion above, we take as a model of the typical mesospheric ice particle: a grain with embedded MSPs where the ice is not necessarily crystalline in structure.

The mean radius and size distribution of mesospheric ice is controlled by the abundance of water vapour, temperature and large scale transport of the involved species. The estimation of particle radius is complicated by the fact that meso-

spheric ice particles are generally non-spherical. Remote mesurements by satellite (Hervig et al., 2009) and ground-based lidar (Rapp et al., 2007b), have yielded axial ratios – the ratio between grain equatorial and rotational axes – of either $\sim 0.2 - 0.5$ (needle-like) or $\sim 2 - 5$ (plate-like). To which degree ambient parameters can affect the shape of the particles, is still an open question. In any case, the simplest growth models which yields spherical particles probably do not reflect reality well for the majority of mesospheric clouds.

The proportionality to radius in the optical cross-section ($\propto r_d^6$) means that optical methods such as lidar and photometers are insensitive to the smallest particles. Such instruments can only observe sizes above several nanometres; thus losing a large part of the size distribution. For the interpretation of lidar measurements, it is commonly assumed that the distribution of sizes is monomodal Gaussian. This has also been backed up by simulations (Rapp and Thomas, 2006; Baumgarten et al., 2010). Using this assumption, the mean size of particles producing NLC have been reported to be $\sim 30 - 70$ nm, with a typical width of ~ 10 nm (see e.g. Von Cossart et al. (1999); Rapp and Thomas (2006); Baumgarten et al. (2010); Megner et al. (2009)). The mean peak backscatter height as recorded by lidar is ~ 83 km, and this is found to increase on the order of ~ 80 m per decade (Fiedler et al., 2017). Particles of sizes below a few nanometres are more elusive, and their size distribution have not been investigated thoroughly. Measurements of solar occultaion by ice from satellite suggest an inverse proportionality between concentration and radius at altitudes of peak occultation (Hervig et al., 2009). The same observations also yield a broader range of mean sizes and a higher variance in the distribution width compared to lidar measurements. The variance in optical observations and poor sensitivity to the smallest sizes calls for an alternative way to obtain the key parameters of mesospheric ice.

In the following we will outline the theory of how ice particle sizes can be derived by the use of the DUSTY Faraday cups, obtaining a much better altitude resolution and theoretical size range than remote methods.

Sizes of Ice Particles derived from DUSTY measurements

We recall that the DUSTY probe, as introduced in Ch. 4, has three grids G0, G1 and G2 at respectively 0 V, + 6.2 V and - 6.2 V. The bottomplate detector has a bias of + 2 V. The cross-section of the two uppermost grids is $\sigma_0 = \sigma_1 = 0.046$ times the probe cross-section. G2 has thicker wires to increase the secondary charging effects, with $\sigma_2 = 0.235$. We recall from eqs. (4.1) and (4.2), that

the current recorded on grid 2 must be $I_{G2} = \sigma_2 I_D + I_{sec}$, where I_D is the current in front of the grid. Consequently, the bottom plate current becomes $I_{BP} = (1 - \sigma_2) I_D - I_{sec}$. The electrons which are rubbed off from G2 will produce a positive current I_{sec} to G2, which will furthermore be deposited on BP and create a negative current $-I_{sec}$ there. We can eliminate the secondary current to express I_D in terms of measured currents as

$$I_D = I_{G2} + I_{BP} \tag{5.14}$$

where the secondary production from G1 and G0 is neglected, as the small fragments will be stopped by air friction and heavy evaporation (Antonsen and Havnes, 2015). The total current into the probe is given by eq. (4.3), and amounts to $\approx 1.1 I_D$ when adjusted for σ_0 and σ_1.

In earlier papers on DUSTY, the ratio between the currents to G2 and BP have been used to extract information on how effective the secondary charging current is. In terms of previously defined terms we have

$$R = \frac{I_{G2}}{I_{BP}} = \frac{\sigma_2 I_D + I_{sec}}{(1 - \sigma_2) I_D - I_{sec}} \tag{5.15}$$

which for the limit $I_{sec} \to 0$ becomes $R = 0.31$, and in the limit $I_{sec} \gg I_D$ becomes $R = -1$. The charging of mesospheric ice by plasma scales roughly with particle radius. Thus in general, when the secondary current dominates, it can be expected that the ice particles are large – on the order of tens of nanometers (Havnes and Næsheim, 2007; Havnes et al., 2009). When the ratio is weakly positive we expect smaller particles. This is in accordance with the assumptions used in the analysis of MUDD data, that the impact charging of the particles scales with their cross-section or volume. The secondary current in DUSTY can be stated as:

$$I_{sec} = e n_d v_R A_{sec} \eta(r_d) \tag{5.16}$$

where $A_{sec} = \sigma_s \sigma_2 \sigma \approx 7\%$ is the effective area for secondary current production. The parameter σ_s describes how large portion of a grid that can produce secondary charge, and was calculated by Havnes and Næsheim (2007) to be 0.28. The secondary charging factor, $\eta(r_d)$, is here taken to be dependent on radius, and is found from earlier flights of DUSTY to be between 50 to 100 for a large reference particle. If we assume the ice particles have a charging probability proportional to cross-section and inserting for the secondary current as defined above, we obtain

$$\left(\frac{r_d}{r_{ref}} \right)^2 = \frac{(1 - \sigma_2) I_{G2} - \sigma_2 I_{BP}}{A_{sec} \eta_{ref} e n_d v_R} \tag{5.17}$$

where η_{ref} is the number of secondary charges produced for a particle of size r_{ref}. Usually, this reference value is taken to be 50 for a radius of 50 nm.

We note that the only unknown parameter in eq.(5.17) is the number density n_d. If we include a charging model, we can therefore solve self-consistently for particle radius, since DUSTY can measure the dust charge number density, $n_d Z_d$, directly. In Paper IV, we calculate the equilibrium charge by assuming quasi-neutrality and that electron collisional charging is the most significant mechanism; photo-ionization is neglected in the following. The electron density is measured by probes on the payload. The coupled system of equations can then be iterated, and only requires an initial guess of average charge number (for which a good guess is $\bar{Z}_d = -1$). In figure 5.4 we show the result of such an iteration based on from the MXD-1 flight compared to sizes estimated by RMR lidar and an in-situ photometer. The lidar generally yields smaller sizes than the iteration, which may be due to several reasons; e.g. the large difference in sampling volume or assumptions of particle intrinsic parameters. There is also some uncertainty connected to how the very smallest particles, below a few nanometres, affect the total and secondary current in DUSTY.

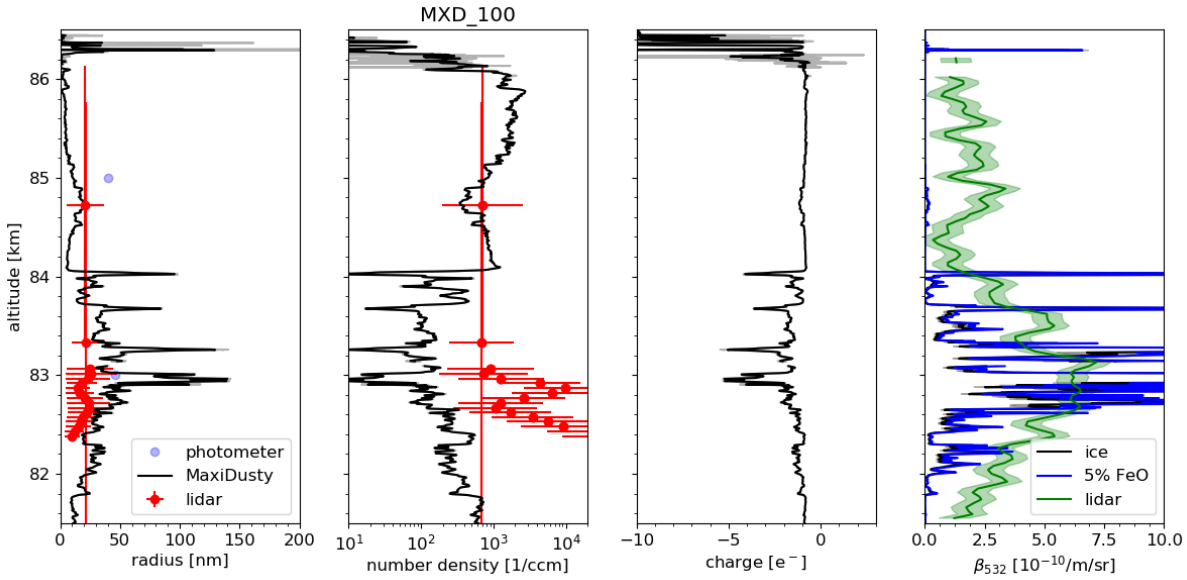

Figure 5.4: Results from iteration of equation (5.17) with a charging model. The solid black curves in panels 1, 2 and 3 show the calculated radius, number density and average charge number respectivly. The red dots represent estimated mean size (Panel 1) and density (Panel 2) from RMR lidar measurements. The rightmost panel show estimates of the optical backscatter ar 532 nm using the iteration results. Adapted from Paper IV, Copyright © Copernicus.

Chapter 6

Multi-scale Variations in the Mesospheric Dusty Plasma

The endorsement of in-situ observation of dusty plasmas or neutrals in the mesosphere, is commonly motivated by the superior height resolution of sounding rocket probes. Also, their very localized sampling normally result in a larger variance in observed parameters than integrating methods such remote radars and lidar. Rocket soundings are not, however, the only means of investigating the mesopause at very small scales. PMSEs, introduced in chapter 3, have been observed with UHF radars at frequencies as high as 1.29 GHz (Cho et al., 1992). Since PMSEs are coherent structures in the dusty plasma at the radar Bragg-scale. For UHF-radars this scale is $\sim$ 10 cm. Nevertheless, the integration in height and time makes it difficult for utilizing radars to monitor phenomena such as density variations and flow shears on the smallest scales.

Even though sounding rockets provide a most suitable platform to investigate fluctuations in the dusty plasma on the smallest spatial scales, few studies have utilized this capability. The works of Rapp et al. (2003a) and Lie-Svendsen et al. (2003) which respectively presented observations and modelling of the interconnection between aerosols and electrons on the smallest scales, are in fact some of the most recent works in this sub-field. Strelnikov et al. (2009) studied neutral fluctuation at small spatial scales, which is important to the understanding of PMSE formation.

In simultaneous measurements of PMSE and in-situ soundings, there are always differences. Some of these differences, but probably not all, are connected to the difference in sampling volume. In order to explain these, one must have a good despcription of the interconnection between aerosols and electrons for a range of ambient parameters and on a range of length scales. The ultimate reward for

such inquiries, is that the relationship between PMSE and aerosols can be better understood.

The MXD payloads were equipped with the DUSTY and MUDD probes to measure aerosols and multi-Needle Langmuir probes to measure the electron density on scales down to $\sim$ 10 cm. On MXD-1B, we launched two mechanically and electronically identical DUSTY probes with an interspacing of $\sim$ 10 cm in order to characterize horizontal differences in the charged aerosol population. The results, as presented in Paper III, show a highly complex interplay between the dusty plasma species. The flow around the payload is also found to affect recorded currents. Moreover, it is difficult to find a simple relationship (or *proxy*) between dusty plasma parameters and PMSE. In the following, we elaborate on this.

6.1 Fluctuations on the Small Scales

For particles of sizes larger than several nanometres, the neutral drag is not enough to to deflect them in the payload shock front and they will typically reach the bottom plate of DUSTY with a velocity close to that of the payload. Ideally then, with a top deck geometry as MXD-1B with two identical DUSTY probes with small interspacing, the probes would record the same current if large horizontal variations in the dusty plasma on the same scales as the interspacing are not present. Figure 6.1 shows a situation which is close to such an "ideal" scenario. From the bottom panel, we see that the ratio between DUSTY 1 and 2 currents fluctuates with the spin frequency; such oscillations are seldomly not present in mesospheric rocket soundings, and are often either left untreated or spin components are filtered. The reason these oscillations occur, as discussed in Paper III, is probably due to the smallest particles being more prone to aerodynamic modulation. Other adverse effects such as payload charging and secondary sprays of particles from other parts of the top deck may also be plausible (Kassa et al., 2012).

One motivation to look into these unwanted effects, is that similar signatures are easier to overlook when only looking at a single probe – which is typically the case. Although a spin-polluted signal is simple to correct for, it is seldomly emphasized that there may be large horizontal differences even between probes on the same deck. The threshold for wrongly interpreting observations can in such cases be significantly lowered. In figure 6.2 we show a comparison between the DUSTY probes on MXD-1B in a region with a sharp onset to strongly spin

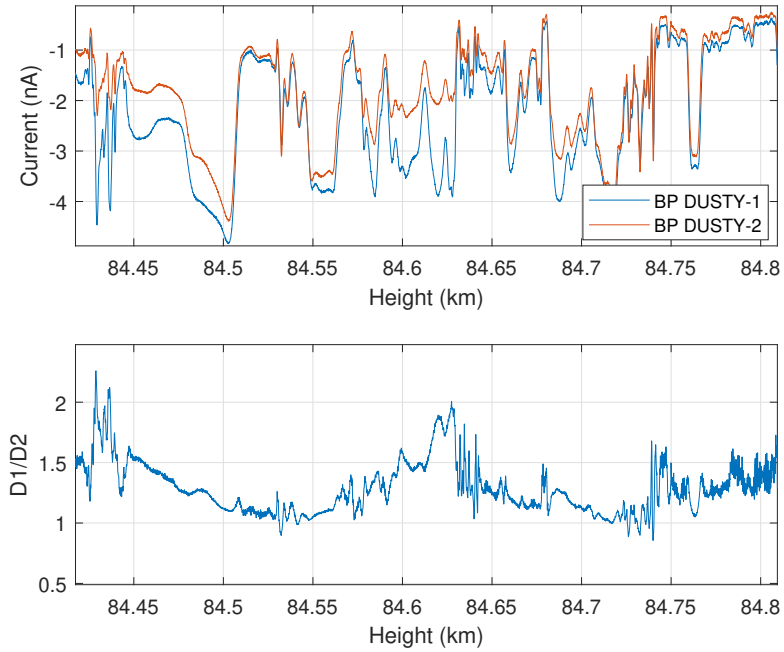

Figure 6.1: Medium scale close-up of a comparison between DUSTY 1 and DUSTY 2 on MXD-1B.The $D1/D2$-ratio is close to unity, underlining the good agreement at these scales. From Paper III.

modulated signals. The ratio of the currents display a phase shift equal to the azimuthal phase between the probes which can be interpreted as: (1) Aerodynamic modulation of (small) aerosols, or (2) A consistent difference in charge number density at the scale of the interspacing between the DUSTY probes. In Paper III we find (1) to be the most plausible explanation.

In figure 6.3 we present a comparison between electron density and DUSTY bottom plate currents in a $\sim$ 200 metre height range inside the MXD-1B cloud system. In this relatively thin slice, the correlation between the two is virtually one-to-one throughout the whole range, implying that the present ice particles absorb free electrons effectively. This is analogous to a classical bite-out in the electron population. One of the open questions addressed in Paper III, is whether or not such a bite-out is the only possible coupling between the electron and dust populations or if a postitive correlation between electrons and (negatively charged) dust can occur. This latter scenario was proposed by Lie-Svendsen et al. (2003) as a possibility during periods of sharp positive temperature gradients. For the MXD-1B flight we find that the overwhelming majority of the cloud system displays traditional bite-outs on short length scales and that positive correlations are found on longer length scales. To resolve whether or not such positive cor-

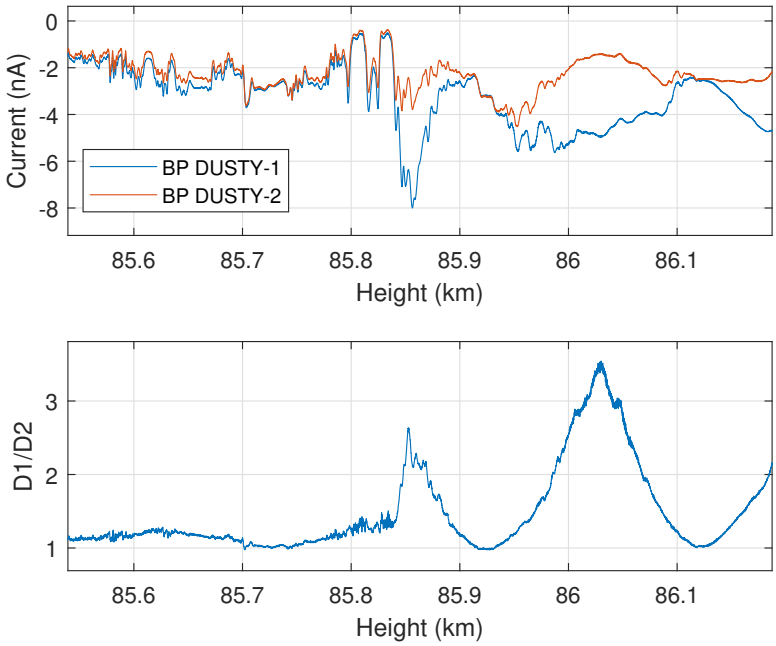

Figure 6.2: Close-up of a region where a strong disagreement between DUSTY 1 and DUSTY 2 on MXD-1B sets in. The ratio of the two DUSTY currents is modulated significantly with the spin frequency ($\sim$ 3.8 Hz). Adapted from Paper III.

relations are causal, one must also analyse the temperature and dynamics of the cloud; this is not done in Paper III.

6.2 Connection between PMSEs and Measured Plasma Parameters

There is a general consensus that charged aerosols are involved in the formation of PMSE. There have been some disscusion about the exact dependence of aerosols and/or electrons in the PMSE reflectivity (see e.g. Varney et al. (2011); Rapp et al. (2008)). For relatively low dust concentrations compared to electron density, as was the case during MXD – the application of the theory on scattering from Bragg-scales structures in a dusty plasma predict that the change in PMSE strength must depend on the square of the co-dependent dust/electron density gradient accordingly:

$$\eta \propto \bar{S}^2 \nabla \langle N_d \rangle^2 \equiv \left(\frac{Z_d N_e}{N_e + Z_i^2 N_i} \right)^2 \cdot \left(\frac{\omega_B^2 N_d}{g} - \frac{\mathrm{d}N_d}{\mathrm{d}t} - \frac{N_d}{H_n} \right)^2 \tag{6.1}$$

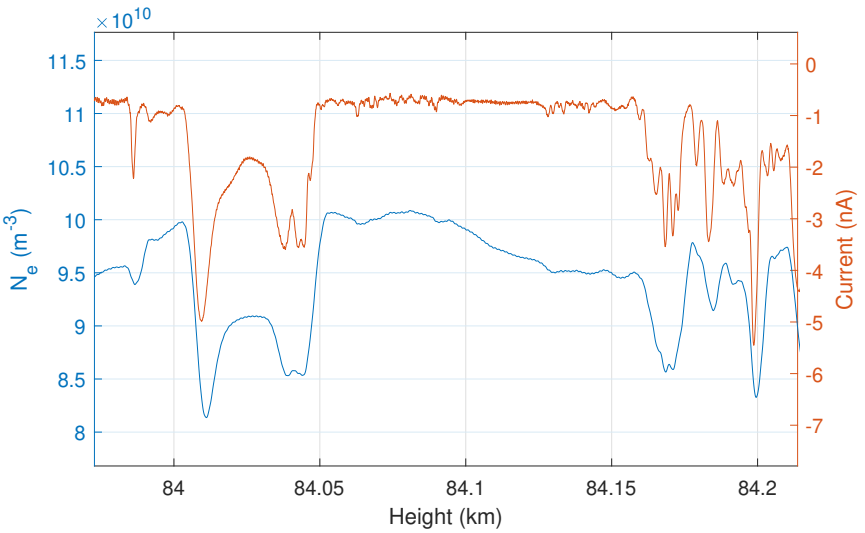

Figure 6.3: Comparison between electron density recorded by m-NLP and DUSTY current (proportional to dust charge number denstiy). The electron density height vector is shifted according to the angle between DUSTY-1 and mNLP Boom-1 ($\sim$ 20 m in height). We note a correlation on length scales $\sim$ 10 m implying anti-correlation between absolute densities. Adapted from Paper III

where $\bar{S}/Z_d$ is the mean number of Debye-sphere electrons and $\nabla\langle N_d\rangle$ is the gradient of dust density across acloud layer. In the gradient term, ω_B is the buoyancy frequency, g is the gravitational constant and H_n is the neutral scale height.

An idealized picture of the PMSE mechanism is that neutral turbulence on different length scales affect aerosols which subsequently reduce the diffusivity of electrons. Resulting gradients in the electron density, which due to the lowered diffusivity are long-lived in comparisson with thermal fluctuations, then form structures in the plasma which a radar wave can scatter from. PMSEs are thus coherent scatter from such structures on the scale of the radar Bragg-length; for the IAP MAARSY radar which was utilized during MXD, this is $\approx$ 2.8 m. A direct way to predict if fluctuations in the dusty plasma would support a PMSE, is therefore to investigate the spectral properties of the fluctuations at said Bragg scale. If the fluctuations have sufficient power, i.e. they are not attenuated in the viscous subrange, the plasma could likely support a PMSE. In figure 6.4 we show the result from a wavelet analysis done in Paper III. The wavelet power spectrum was derived from DUSTY current fluctuations, and is found to correspond reasonably well with radar SNR.

The full theoretical expression for reflectivity includes ordering parameters such as the Richardson- and Prandtl-number, in addition to microphysical parame-

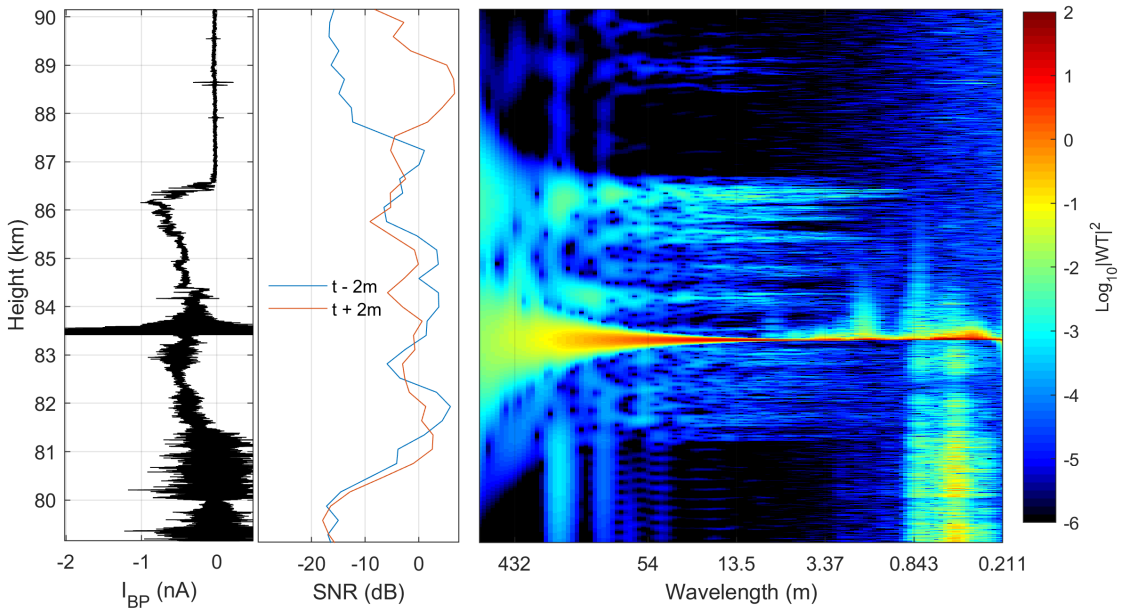

Figure 6.4: Comparison of DUSTY bottom plate current (left panel), MAARSY 53.5 MHZ radar SNR along the rocket trajectory (middle panel) and PSD from wavelet transform (right panel) – for the MXD-1 launch on the 30th of June, 2016. Conversion from frequency to spatial scales is done by using the mean rocket velocity throughout the dust cloud. Radar data courtesy of Ralph Latteck, IAP Kühlungsborn. From Paper III.

ters such as the Batchelor-scale, buoyancy frequency. Due to the complexity and impractical nature of the full expression, a few authors have suggested ordering parameters or *proxies* for PMSE formation (or strength) consisting of simple combinations of dusty plasma parameters. Paper III discusses this topic and argues that a gradient terms should probably be included in the proxy. Figure 6.5 show a comparison of four of the presumed best candidates for proxies and PMSE SNR during MXD-1B.

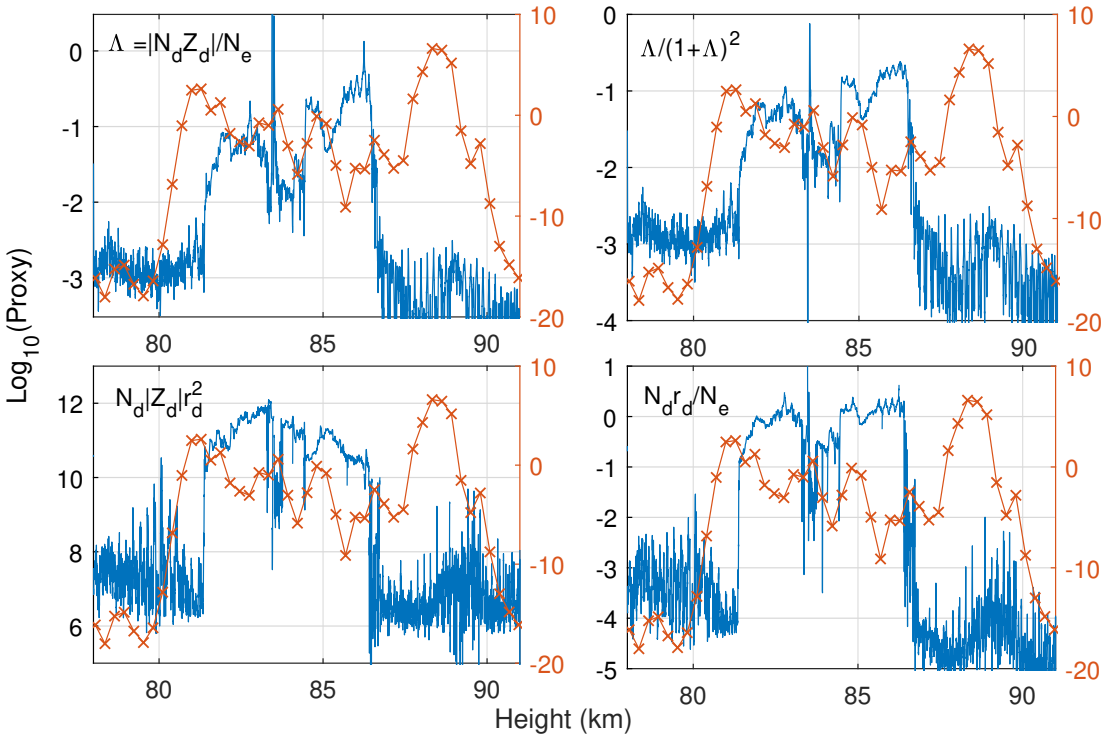

Figure 6.5: Comparison of proxies from dusty plasma parameters to PMSE SNR for the MXD-1 flight. The upper left panel is the Havnes-parameter. The upper right panel is a proxy based on the Havnes-parameter which is consistent with a one-to-one anti-correlation between electrons and charged aerosols. The proxy in the lower left panel can be recognized as the parameter utilized by Rapp et al. (2003b), while the bottom right panel is the factor used by Havnes (2004) which takes the dust radius into account. From Paper III.

Chapter 7

Future Work

The first results from the MAXIDUSTY campaign have given new insights on aerosols in the summer mesosphere. Some of the presented results in this volume pose interesting questions that warrant further investigation, but which are beyond the scope of this thesis. We shortly elaborate below on a few new ideas and ongoing endeavours that have come into being in the wake[1] of MAXIDUSTY.

7.1 In-situ observation of Meteoric Smoke Particles

As established throughout this thesis introduction, much of the recent focus for in-situ measurements in the mesosphere have been directed towards the elusive meteoric smoke particles. These particles have previously been detected in-situ, but remain the least investigated aerosol species in the upper atmosphere. From MAXIDUSTY measurement and theoretical developments during the projects, we find that Faraday cups may well be utilized to observe MSPs in their free form. We have suggested and built a new probe, SPID (see fig. 4.9 for geometry), which aims to solve the problem of adverse flow effects by using an open Faraday cup design. The Probe is to be launched on the G-Chaser Payload in January of 2019.

Figure 7.1 shows the results of a set of simulations done to determine the size threshold for detection at different altitudes for the SPID probe ('modified MUDD' in the legend) and the MUDD probe. In these simulations the composition was assumed to be a Magnesium-Silicon ferrous oxide, i.e. representable for MSPs. For MUDD at 70 km, the lowest possible detectable size is $\gtrsim 2.8$ nm, while the SPID probe can theoretically measure free MSPs smaller than 1 nm at

[1] Pun intended

the same altitude. By switching potentials in a similar manner as MUDD, it may be possible for future SPID probes to resolve a high resolution mass spectrum of *free* MSPs.

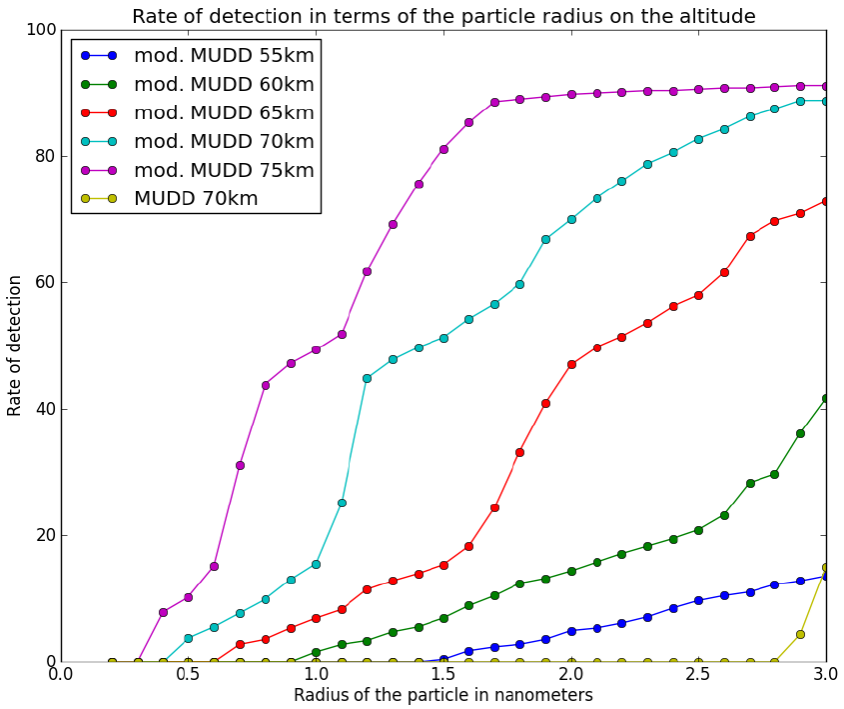

Figure 7.1: Relative detection rate in a prototype of the SPID probe (here labelled as 'modified MUDD') of neutral MSPs for different sizes at varying altitudes. The detection rate at 70 km of the original MUDD probe is also shown (yellow).

7.2 Retrieval of Meteoric Smoke Particles

In sampling and return experiments the deflection of the smallest aerosols presents a great technical challenge. As utilized in MUDD the large NLC/PMSE ice particles are more or less unaffected by the shock front of the rocket, and can be collected effectively. As described in Havnes et al. (2015), we therefore suggest a retrieval experiment (MESS = MEteoric Smoke Sampler) which collects large ice particles. A funnel will steer particles into a collection chamber with an electronic valve. The chamber will contain TEM grids to which particles will stick, and only MSPs embedded in the ice particles will be left after the ice evaporates. The TEM grids will subsequently be analysed in a clean lab. The MESS probe will have two identical sampling chambers where one stays closed during the whole flight and will eventually be compared with the real sampling chamber which is open when the clouds are passed.

Chapter 8

Conclusions

The MAXIDUSTY sounding rocket campaign was successfully completed in the summer of 2016 at the Andøya Space Centre. Two payloads contained instrumentation aimed at conducting multi-scale observation of electrons, ions and charged aerosols. In the current work, we have put special emphasis on the application of new measurement techniques using Faraday cup aerosol detectors. These efforts have yielded methods which can be used to determine intrinsic dust parameters such as charge, size, number density as well as spatial characteristics on scales of $\sim$ 10 cm.

By modelling the movement and energy balance of fragments of mesospheric ice particles inside the Faraday impact detector MUDD, we have shown that MSPs can dominate the detector current (Paper I). With this method, we used the data from two triplets of MUDD flown on the respective MAXIDUSTY payloads to derive the size distribution of embedded MSPs inside mesospheric ice particles (Paper II). The derived size distributions are sensitive to the charging probability, which we argue is proportional to r_d^k for k between 2 and 3. Moreover, the distributions were found to follow inverse power laws which are found to be slightly steeper than model predictions of free MSP size distributions. This work presents another confirmation of that MSPs are abundant in mesospheric ice particles with volume filling factors up to several percent.

This thesis supports that the secondary charging effect is important for aerosol detection with Faraday cups. In both the MUDD and DUSTY probes, this effect have been utilized to obtain information on particle characteristics. Our analysis showed that the secondary (current) yield can be estimated with good certainty by comparing MUDD and DUSTY currents. Based on this, we developed a method to calculate the sizes, charges and number densities of ice particles using DUSTY. The method shows a reasonable agreement with optical mea-

surements, but we underline that the sensitivity to electron density is relatively strong.

From the commensurate of measurements discussed in the present volume, the importance of properly characterizing effects such as flow around the payload body and electric potentials arising from payload charging becomes clear. For the MAXIDUSTY-1B flight we find a strong disagreement between aerosol currents from mechanically and electrically similar probes (Paper III). This is attributed to very small particles (of sizes $\sim$ a few nanometres) being heavily modulated in the complex aerodynamic and electric environment around the rocket payload. The question arises whether or not this is common for similar rocket sounding experiments.

We argue that Faraday cups can be instrumental in the inquiry into the exact role of aerosols in the formation of PMSEs. This relationship is difficult to reduce to a simple proxy consisting of dusty plasma parameters (Paper III), however spectral properties and simultaneous electron and aerosol measurements can be used in determining a correct reflectance expression – if the reflectance is indeed co-dependent of electrons and aerosols. Our conclusion on this topic, is that charged aerosols and electrons are in general anti-correlated even on very short scales and for very low densities (Paper III). We also report on very weak dust structures on altitudes well below the mesopause (Paper V). For these findings, it is probably necessary with a strong updraft below summer mesopause altitudes. These novel clouds in the summer mesosphere may have a mechanism which differ from PMSE

References

Adams, N. and Smith, D.: Studies of microparticle impact phenomena leading to the development of a highly sensitive micrometeoroid detector, Planetary and Space Science, 19, 195 – 204, doi: 10.1016/0032-0633(71)90199-1, 1971.

Allen, J. E., Annartone, B. M., and de Angelis, U.: On the orbital motion limited theory for a small body at floating potential in a Maxwellian plasma, Journal of Plasma Physics, 63, 299–309, 2000.

Amyx, K., Sternovsky, Z., Knappmiller, S., Robertson, S., Horanyi, M., and Gumbel, J.: In-situ measurement of smoke particles in the wintertime polar mesosphere between 80 and 85 km altitude, Journal of Atmospheric and Solar-Terrestrial Physics, 70, 61–70, 2008.

Anderson, J. G.: Rocket measurement of OH in the mesosphere, Journal of Geophysical Research, 76, 7820–7824, 1971.

Andersson, P. U., Tomsic, A., Andersson, M. B., and Petterson, J. B.: Emission of small fragments during water cluster collisions with a graphite surface, Chemical Physics Letters, 279, 100–106, doi: http://dx.doi.org/10.1016/S0009-2614(97)00990-1, 1997.

Antonsen, T. and Havnes, O.: On the detection of mesospheric meteoric smoke particles embedded in noctilucent cloud particles with rocket-borne dust probes, Review of Scientific Instruments, 86, 033 305, doi: http://dx.doi.org/10.1063/1.4914394, 2015.

Antonsen, T., Havnes, O., and Mann, I.: Estimates of the Size Distribution of Meteoric Smoke Particles From Rocket-Borne Impact Probes, Journal of Geophysical Research: Atmospheres, doi: 10.1002/2017JD027220, 2017.

Antonsen, T., Havnes, O., and Spicher, A.: Multi-scale Measurements of Mesospheric Aerosols and Electrons During the MAXIDUSTY Campaign., Atmospheric Measurement Techniques, In Review, 2018.

Asmus, H., Wilms, H., Strelnikov, B., and Rapp, M.: On the heterogeneous nucleation of mesospheric ice on meteoric smoke particles: Microphysical modeling, Journal of Atmospheric and Solar-Terrestrial Physics, 118, 180–189, 2014.

Asmus, H., Robertson, S., Dickson, S., Friedrich, M., and Megner, L.: Charge balance for the mesosphere with meteoric dust particles, Journal of Atmospheric and Solar-Terrestrial Physics, 127, 137–149, doi: 10.1016/j.jastp.2014.07.010, 2015.

Asmus, H., Staszak, T., Strelnikov, B., Lübken, F.-J., Friedrich, M., and Rapp, M.: Estimate of size distribution of charged MSPs measured in situ in winter during the WADIS-2 sounding rocket campaign, Annales Geophysicae, 35, 979–998, doi: 10.5194/angeo-35-979-2017, 2017.

Austin, J., Tourpali, K., Rozanov, E., Akiyoshi, H., Bekki, S., Bodeker, G., Brühl, C., Butchart, N., Chipperfield, M., Deushi, M., et al.: Coupled chemistry climate model simulations of the solar cycle in ozone and temperature, Journal of Geophysical Research: Atmospheres, 113, 2008.

Bailey, A.: Electrostatic phenomena during powder handling, Powder Technology, 37, 71–85, 1984.

Baines, M., Williams, I., Asebiomo, A., and Agacy, R.: Resistance to the motion of a small sphere moving through a gas, Monthly Notices of the Royal Astronomical Society, 130, 63–74, 1965.

Bardeen, C., Toon, O., Jensen, E., Marsh, D., and Harvey, V.: Numerical simulations of the three-dimensional distribution of meteoric dust in the mesosphere and upper stratosphere, Journal of Geophysical Research: Atmospheres, 113, 2008.

Baumgarten, G., Fiedler, J., and Rapp, M.: On microphysical processes of noctilucent clouds (NLC): observations and modeling of mean and width of the particle size-distribution, Atmospheric Chemistry and Physics, 10, 6661–6668, doi: 10.5194/acp-10-6661-2010, URL https://www.atmos-chem-phys.net/10/6661/2010/, 2010.

Beig, G.: Long-term trends in the temperature of the mesosphere/lower thermosphere region: 1. Anthropogenic influences, Journal of Geophysical Research: Space Physics, 116, 2011.

Bekkeng, J. K.: Prototype Development of a Low-Cost Sounding Rocket Attitude Determination System and an Electric field Instrument, Ph.D. thesis, Univeristy of Oslo, 2007.

Biebricher, A. and Havnes, O.: Non-equilibrium modeling of the PMSE Overshoot Effect revisited: A comprehensive study, Journal of Plasma Physics, 78, 303–319, 2012.

Bird, G.: The DS2V/3V program suite for DSMC calculations, in: AIP Conference Proceedings, vol. 762, pp. 541–546, AIP, 2005.

Blix, T., Thrane, E., and Andreassen, Ø.: In situ measurements of the fine-scale structure and turbulence in the mesosphere and lower thermosphere by means of electrostatic positive ion probes, Journal of Geophysical Research: Atmospheres, 95, 5533–5548, doi: 10.1029/JD095iD05p05533, 1990.

Boyd, I. D.: Predicting breakdown of the continuum equations under rarefied flow conditions, in: AIP Conference Proceedings, vol. 663, pp. 899–906, AIP, 2003.

Cho, J. Y. and Röttger, J.: An updated review of polar mesosphere summer echoes: Observation, theory, and their relationship to noctilucent clouds and subvisible aerosols, Journal of Geophysical Research: Atmospheres, 102, 2001–2020, 1997.

Cho, J. Y. N., Kelley, M. C., and Heinselman, C. J.: Enhancement of Thomson scatter by charged aerosols in the polar mesosphere: Measurements with a 1.29-GHz radar, Geophysical Research Letters, 19, 1097–1100, doi: 10.1029/92GL01155, 1992.

DeCarlo, P. F., Slowik, J. G., Worsnop, D. R., Davidovits, P., and Jimenez, J. L.: Particle morphology and density characterization by combined mobility and aerodynamic diameter measurements. Part 1: Theory, Aerosol Science and Technology, 38, 1185–1205, 2004.

Draine, B. and Sutin, B.: Collisional charging of interstellar grains, The Astrophysical Journal, 320, 803–817, 1987.

Eidhammer, T. and Havnes, O.: Size dependence of the mesospheric dust temperature and its influence on the noctilucent clouds and polar mesosphere summer echo phenomena, Journal of Geophysical Research: Space Physics, 106, 24 831–24 841, 2001.

Evans, A.: The dusty universe., Ellis Horwood, New York, NY (USA), 1993.

Fiedler, J., Baumgarten, G., Berger, U., and Luebken, F.-J.: Long-term variations of noctilucent clouds at ALOMAR, Journal of Atmospheric and Solar-Terrestrial Physics, 162, 79–89, 2017.

Fomichev, V., Blanchet, J.-P., and Turner, D.: Matrix parameterization of the 15 μm CO2 band cooling in the middle and upper atmosphere for variable CO2 concentration, Journal of Geophysical Research: Atmospheres, 103, 11 505–11 528, 1998.

Friichtenicht, J.: Micrometeroid simulation using nuclear accelerator techniques, Nuclear Instruments and Methods, 28, 70 – 78, doi: http://dx.doi.org/10.1016/0029-554X(64)90351-9, 1964.

Gelinas, L. J., Lynch, K. A., Kelley, M. C., Collins, S., Baker, S., Zhou, Q., and Friedman, J. S.: First observation of meteoritic charged dust in the tropical mesosphere, Geophysical Research Letters, 25, 4047–4050, doi: 10.1029/1998GL900089, 1998.

Goldberg, R., Pfaff, R., Holzworth, R., Schmidlin, F., Voss, H., Tuzzolino, A., Croskey, C., Mitchell, J., Friedrich, M., Murtagh, D., et al.: DROPPS: A study of the polar summer mesosphere with rocket, radar and lidar, Geophysical research letters, 28, 1407–1410, 2001.

Grams, G. and Fiocco, G.: Equilibrium temperatures of spherical ice particles in the upper atmosphere and implications for noctilucent cloud formation, Journal of Geophysical Research, 82, 961–966, 1977.

Gumbel, J. and Megner, L.: Charged meteoric smoke as ice nuclei in the mesosphere: Part 1–A review of basic concepts, Journal of Atmospheric and Solar-Terrestrial Physics, 71, 1225–1235, doi: https://doi.org/10.1016/j.jastp.2009.04.012, 2009.

Gumbel, J. and Witt, G.: Rocket-borne photometry of NLC particle populations, Advances in Space Research, 28, 1053–1058, 2001.

Havnes, O.: Polar Mesospheric Summer Echoes (PMSE) overshoot effect due to cycling of artificial electron heating, Journal of Geophysical Research: Space Physics, 109, 2004.

Havnes, O. and Kassa, M.: On the sizes and observable effects of dust particles in polar mesospheric winter echoes, Journal of Geophysical Research: Atmospheres, 114, 2009.

Havnes, O. and Næsheim, L. I.: On the secondary charging effects and structure of mesospheric dust particles impacting on rocket probes, Annales Geophysicae, 25, 623–637, doi: 10.5194/angeo-25-623-2007, 2007.

Havnes, O., Morfill, G., and Goertz, C.: Plasma potential and grain charges in a dust cloud embedded in a plasma, Journal of Geophysical Research: Space Physics, 89, 10 999–11 003, 1984.

Havnes, O., Trøim, J., Blix, T., Mortensen, W., Næsheim, L. I., Thrane, E., and Tønnesen, T.: First detection of charged dust particles in the Earth's mesosphere, Journal of Geophysical Research: Space Physics, 101, 10 839–10 847, doi: 10.1029/96JA00003, 1996.

Havnes, O., Surdal, L. H., and Philbrick, C. R.: Mesospheric dust and its secondary effects as observed by the ESPRIT payload, Annales Geophysicae, 27, 1119–1128, doi: 10.5194/angeo-27-1119-2009, 2009.

Havnes, O., Gumbel, J., Antonsen, T., Hedin, J., and Hoz, C. L.: On the size distribution of collision fragments of NLC dust particles and their relevance to meteoric smoke particles, Journal of Atmospheric and Solar-Terrestrial Physics, 118, 190–198, doi: http://dx.doi.org/10.1016/j.jastp.2014.03.008, 2014.

Havnes, O., Antonsen, T., Hartquist, T., Fredriksen, Å., and Plane, J.: The Tromsø programme of in situ and sample return studies of mesospheric nanoparticles, Journal of Atmospheric and Solar-Terrestrial Physics, 127, 129–136, 2015.

Havnes, O., Antonsen, T., Baumgarten, G., Hartquist, T., Fredriksen, Å., Friedrich, M., and Hedin, J.: A new method to inference the size, number density, and charge of mesospheric dust from its in situ collection by the DUSTY probe., Atmospheric Measurement Techniques, In Review, 2018a.

Havnes, O., Latteck, R., Hartquist, T. W., and Antonsen, T.: First simultaneous rocket and radar detections of rare low summer mesospheric clouds., Geophysical Research Letters, 45, 5727–5734, doi: 10.1029/2018GL078218, 2018b.

Hedin, J., Gumbel, J., and Rapp, M.: On the efficiency of rocket-borne particle detection in the mesosphere, Atmospheric Chemistry and Physics, 7, 3701–3711, doi: 10.5194/acp-7-3701-2007, 2007.

Hedin, J., Giovane, F., Waldemarsson, T., Gumbel, J., Blum, J., Stroud, R. M., Marlin, L., Moser, J., Siskind, D. E., Jansson, K., et al.: The MAGIC meteoric smoke particle sampler, Journal of Atmospheric and Solar-Terrestrial Physics, 118, 127–144, 2014.

Hervig, M. E., Gordley, L. L., Stevens, M. H., Russell III, J. M., Bailey, S. M., and Baumgarten, G.: Interpretation of SOFIE PMC measurements: Cloud identification and derivation of mass density, particle shape, and particle size, Journal of Atmospheric and Solar-Terrestrial Physics, 71, 316–330, 2009.

Hervig, M. E., Deaver, L. E., Bardeen, C. G., III, J. M. R., Bailey, S. M., and Gordley, L. L.: The content and composition of meteoric smoke in mesospheric ice particles from SOFIE observations, Journal of Atmospheric and Solar-Terrestrial Physics, 84-85, 1 – 6, doi: http://dx.doi.org/10.1016/j.jastp.2012.04.005, 2012.

Hervig, M. E., Bardeen, C. G., Siskind, D. E., Mills, M. J., and Stockwell, R.: Meteoric smoke and H2SO4 aerosols in the upper stratosphere and mesosphere, Geophysical Research Letters, 44, 1150–1157, 2017.

Horányi, M., Gumbel, J., Witt, G., and Robertson, S.: Simulation of rocket-borne particle measurements in the mesosphere, Geophysical Research Letters, 26, 1537–1540, 1999.

Huba, J. D.: NRL: Plasma formulary, Tech. rep., NAVAL RESEARCH LAB WASHINGTON DC BEAM PHYSICS BRANCH, 2018.

Hunten, D. M., Turco, R. P., and Toon, O. B.: Smoke and Dust Particles of Meteoric Origin in the Mesosphere and Stratosphere, Journal of the Atmospheric Sciences, 37, 1342–1357, doi: 10.1175/1520-0469(1980)037<1342:SADPOM>2.0.CO;2, 1980.

Jacobsen, K., Pedersen, A., Moen, J., and Bekkeng, T.: A new Langmuir probe concept for rapid sampling of space plasma electron density, Measurement Science and Technology, 21, 085 902, 2010.

Jacobsen, T. and Friedrich, M.: Electron density measurements in the lower D-region, Journal of Atmospheric and Terrestrial Physics, 41, 1195 – 1200, doi: http://dx.doi.org/10.1016/0021-9169(79)90022-9, 1979.

Jesse, O.: Auffallende erscheinungen am abendhimmel, Met. Zeit, 2, 311–312, 1885.

John, W., Reischl, G., and Devor, W.: Charge transfer to metal surfaces from bouncing aerosol particles, Journal of Aerosol Science, 11, 115–138, 1980.

Jones, R., Pyle, J., Harries, J., Zavody, A., Russell, J., and Gille, J.: The water vapour budget of the stratosphere studied using LIMS and SAMS satellite data, Quarterly Journal of the Royal Meteorological Society, 112, 1127–1143, 1986.

Kalashnikova, O., Horanyi, M., Thomas, G., and Toon, O.: Meteoric smoke production in the atmosphere, Geophysical research letters, 27, 3293–3296, 2000.

Kassa, M., Rapp, M., Hartquist, T., and Havnes, O.: Secondary charging effects due to icy dust particle impacts on rocket payloads, Annales Geophysicae, 30, 433–439, 2012.

Kirkwood, S., Dalin, P., and Réchou, A.: Noctilucent clouds observed from the UK and Denmark–Trends and variations over 43 years, Annales geophysicae: atmospheres, hydrospheres and space sciences, 26, 1243, 2008.

Knappmiller, S., Rapp, M., Robertson, S., and Gumbel, J.: Charging of meteoric smoke and ice particles in the mesosphere including photoemission and photodetachment rates, Journal of Atmospheric and Solar-Terrestrial Physics, 73, 2212–2220, doi: http://dx.doi.org/10.1016/j.jastp.2011.01.008, 2011.

Kuuluvainen, H., Arffman, A., Saukko, E., Virtanen, A., and Keskinen, J.: A new method for characterizing the bounce and charge transfer properties of nanoparticles, Journal of Aerosol Science, 55, 104–115, 2013.

Kuuluvainen, H., Saari, S., Mensah-Attipoe, J., Arffman, A., Pasanen, P., Reponen, T., and Keskinen, J.: Triboelectric charging of fungal spores during resuspension and rebound, Aerosol Science and Technology, 50, 187–197, 2016.

Latteck, R., Singer, W., Rapp, M., Vandepeer, B., Renkwitz, T., Zecha, M., and Stober, G.: MAARSY: The new MST radar on Andøya—System description and first results, Radio Science, 47, 2012.

Lübken, F.-J., Lautenbach, J., Höffner, J., Rapp, M., and Zecha, M.: First continuous temperature measurements within polar mesosphere summer echoes, Journal of Atmospheric and Solar-Terrestrial Physics, 71, 453 – 463, doi: 10.1016/j.jastp.2008.06.001, 2009.

Leslie, R.: Sky glows, Nature, 32, 245, 1885.

Lie-Svendsen, Ø., Blix, T., Hoppe, U.-P., and Thrane, E.: Modeling the plasma response to small-scale aerosol particle perturbations in the mesopause region, Journal of Geophysical Research: Atmospheres, 108, 2003.

Lübken, F.-J.: Thermal structure of the Arctic summer mesosphere, Journal of Geophysical Research: Atmospheres, 104, 9135–9149, 1999.

Lübken, F.-J. and Höffner, J.: Experimental evidence for ice particle interaction with metal atoms at the high latitude summer mesopause region, Geophysical research letters, 31, 2004.

Lübken, F.-J., Hillert, W., Lehmacher, G., Von Zahn, U., Bittner, M., Offermann, D., Schmidlin, F., Hauchecorne, A., Mourier, M., and Czechowsky, P.: Intercomparison of density and temperature profiles obtained by lidar, ionization gauges, falling spheres, datasondes and radiosondes during the DYANA campaign, Journal of Atmospheric and Terrestrial Physics, 56, 1969–1984, 1994.

Lübken, F.-J., Strelnikov, B., Rapp, M., Singer, W., Latteck, R., Brattli, A., Hoppe, U.-P., and Friedrich, M.: The thermal and dynamical state of the atmosphere during polar mesosphere winter echoes, Atmospheric chemistry and physics, 6, 13–24, 2006.

Lübken, F.-J., Berger, U., and Baumgarten, G.: Temperature trends in the midlatitude summer mesosphere, Journal of Geophysical Research: Atmospheres, 118, 13,347–13,360, doi: 10.1002/2013JD020576, 2013.

Markovic, N., Andersson, P. U., Någård, M. B., and Pettersson, J. B.: Scattering of water from graphite: simulations and experiments, Chemical Physics, 247, 413 – 430, doi: http://dx.doi.org/10.1016/S0301-0104(99)00233-5, 1999.

Mathews, J., Janches, D., Meisel, D., and Zhou, Q.-H.: The micrometeoroid mass flux into the upper atmosphere: Arecibo results and a comparison with prior estimates, Geophysical Research Letters, 28, 1929–1932, 2001.

Megner, L., Rapp, M., and Gumbel, J.: Distribution of meteoric smoke – sensitivity to microphysical properties and atmospheric conditions, Atmospheric Chemistry and Physics, 6, 4415–4426, doi: 10.5194/acp-6-4415-2006, 2006.

Megner, L., Siskind, D., Rapp, M., and Gumbel, J.: Global and temporal distribution of meteoric smoke: A two-dimensional simulation study, Journal of Geophysical Research: Atmospheres, 113, 2008.

Megner, L., Khaplanov, M., Baumgarten, G., Gumbel, J., Stegman, J., Strelnikov, B., and Robertson, S.: Large mesospheric ice particles at exceptionally high altitudes, Annales Geophysicae, 27, 943–951, doi: 10.5194/angeo-27-943-2009, 2009.

Meriwether, J. W. and Gerrard, A. J.: Mesosphere inversion layers and stratosphere temperature enhancements, Reviews of Geophysics, 42, 2004.

Miles, D. M., Mann, I. R., M., C., D., B., Narod, B. B., Bennes, t. J. R., Pakhoti, n. I. P., A., K., B., B., Nokes, C. D. A., C., C., Haluza-DeLay, T., Elliott, D. G., and Milling, D. K.: A miniature, low-power scientific fluxgate magnetometer: A stepping-stone to cube-satellite constellation missions, Journal of Geophysical Research: Space Physics, 121, 11,839–11,860, doi: 10.1002/2016JA023147, 2016.

Moshfegh, A., Shams, M., Ahmadi, G., and Ebrahimi, R.: A new expression for spherical aerosol drag in slip flow regime, Journal of Aerosol Science, 41, 384–400, 2010.

Murad, E., Swider, W., and Benson, S. W.: Possible role for metals in stratospheric chlorine chemistry, Nature, 289, 273–274, 1981.

Murray, B. J. and Jensen, E. J.: Homogeneous nucleation of amorphous solid water particles in the upper mesosphere, Journal of Atmospheric and Solar-Terrestrial Physics, 72, 51–61, doi: 10.1016/j.jastp.2009.10.007, 2010.

Pedersen, A., Troim, J., and Kane, J.: Rocket measurements showing removal of electrons above the mesopause in summer at high latitude, Planetary and Space Science, 18, 945–947, doi: https://doi.org/10.1016/0032-0633(70)90092-9, 1970.

Plane, J. M.: On the role of metal silicate molecules as ice nuclei, Journal of Atmospheric and Solar-Terrestrial Physics, 73, 2192–2200, 2011.

Plane, J. M.: Cosmic dust in the Earth's atmosphere, Chemical Society Reviews, 41, 6507–6518, 2012.

Plane, J. M. C.: A time-resolved model of the mesospheric Na layer: constraints on the meteor input function, Atmospheric Chemistry and Physics, 4, 627–638, doi: 10.5194/acp-4-627-2004, 2004.

Pruppacher, H. R. and Klett, J. D.: Microphysics of clouds andrecipitation, Wiley, 1997.

Rapp, M.: Charging of mesospheric aerosol particles: the role of photodetachment and photoionization from meteoric smoke and ice particles, Annales Geophysicae, 27, 2417, 2009.

Rapp, M. and Lübken, F.-J.: Polar mesosphere summer echoes (PMSE): Review of observations and current understanding, Atmospheric Chemistry and Physics, 4, 2601–2633, doi: 10.5194/acp-4-2601-2004, 2004.

Rapp, M. and Thomas, G. E.: Modeling the microphysics of mesospheric ice particles: Assessment of current capabilities and basic sensitivities, Journal of Atmospheric and Solar-Terrestrial Physics, 68, 715 – 744, 2006.

Rapp, M., Gumbel, J., and Lübken, F.-J.: Absolute density measurements in the middle atmosphere, Annales Geophysicae, 19, 571–580, 2001.

Rapp, M., Lübken, F.-J., and Blix, T.: Small scale density variations of electrons and charged particles in the vicinity of polar mesosphere summer echoes, Atmospheric Chemistry and Physics, 3, 1399–1407, 2003a.

Rapp, M., Lübken, F.-J., Hoffmann, P., Latteck, R., Baumgarten, G., and Blix, T. A.: PMSE dependence on aerosol charge number density and aerosol size, Journal of Geophysical Research: Atmospheres, 108, 2003b.

Rapp, M., Strelnikova, I., and Gumbel, J.: Meteoric smoke particles: Evidence from rocket and radar techniques, Advances in Space Research, 40, 809–817, 2007a.

Rapp, M., Thomas, G. E., and Baumgarten, G.: Spectral properties of mesospheric ice clouds: Evidence for nonspherical particles, Journal of Geophysical Research: Atmospheres, 112, 2007b.

Rapp, M., Strelnikova, I., Latteck, R., Hoffmann, P., Hoppe, U.-P., Häggström, I., and Rietveld, M. T.: Polar mesosphere summer echoes (PMSE) studied at Bragg wavelengths of 2.8 m, 67 cm, and 16 cm, Journal of Atmospheric and Solar-Terrestrial Physics, 70, 947–961, 2008.

Rapp, M., Strelnikova, I., Strelnikov, B., Friedrich, M., Gumbel, J., Hoppe, U.-P., Blix, T., Havnes, O., Bracikowski, P., Lynch, K., and Knappmiller, S.: Microphysical Properties of Mesospheric Aerosols: An Overview of In Situ-Results from the ECOMA Project, in: Aeronomy of the Earth's Atmosphere and Ionosphere, chap. 4, pp. 67–74, Springer Netherlands, Dordrecht, 2011.

Rizk, B., Hunten, D., and Engel, S.: Effects of size-dependent emissivity on maximum temperatures during micrometeorite entry, Journal of Geophysical Research: Space Physics, 96, 1303–1314, 1991.

Robertson, S., Horanyi, M., Knappmiller, S., Sternovsky, Z., Holzworth, R., Shimogawa, M., Friedrich, M., Torkar, K., Gumbel, J., Megner, L., Baumgarten, G., Latteck, R., Rapp, M., Hoppe, U.-P., and Hervig, M. E.: Mass analysis of charged aerosol particles in NLC and PMSE during the ECOMA/MASS campaign, Annales Geophysicae, 27, 1213–1232, doi: 10.5194/angeo-27-1213-2009, 2009.

Rosinski, J. and Snow, R.: Secondary particulate matter from meteor vapors, Journal of Meteorology, 18, 736–745, 1961.

Saunders, R., Möhler, O., Schnaiter, M., Benz, S., Wagner, R., Saathoff, H., Connolly, P., Burgess, R., Murray, B., Gallagher, M., et al.: An aerosol chamber investigation of the heterogeneous ice nucleating potential of refractory nanoparticles., Atmospheric Chemistry & Physics, 10, 2010.

Saunders, R. W. and Plane, J. M.: A laboratory study of meteor smoke analogues: Composition, optical properties and growth kinetics, Journal of Atmospheric and Solar-Terrestrial Physics, 68, 2182–2202, 2006.

Schröder, W.: Were noctilucent clouds caused by the Krakatoa eruption? A case study of the research problems before 1885, Bulletin of the American Meteorological Society, 80, 2081–2086, 1999.

Schulte, P. and Arnold, F.: Detection of upper atmospheric negatively charged microclusters by a rocket-borne mass spectrometer, Geophysical research letters, 19, 2297–2300, 1992.

Seibert, G. and Battrick, B. T.: The history of sounding rockets and their contribution to European space research, ESA Publications division, 2006.

She, C., Williams, B., Hoffmann, P., Latteck, R., Baumgarten, G., Vance, J., Fiedler, J., Acott, P., Fritts, D., and Lübken, F.-J.: Simultaneous observation of sodium atoms, NLC and PMSE in the summer mesopause region above ALOMAR, Norway (69°N, 12°E), Journal of Atmospheric and Solar-Terrestrial Physics, 68, 93 – 101, doi: https://doi.org/10.1016/j.jastp.2005.08.014, phenomena of the Summertime Mesosphere, 2006.

Smirnov, R., Pigarov, A. Y., Rosenberg, M., Krasheninnikov, S., and Mendis, D.: Modelling of dynamics and transport of carbon dust particles in tokamaks, Plasma Physics and Controlled Fusion, 49, 347, 2007.

Solomon, S.: Stratospheric ozone depletion: A review of concepts and history, Reviews of Geophysics, 37, 275–316, 1999.

Strelnikov, B., Rapp, M., Strelnikova, I., Engler, N., and Latteck, R.: Small-scale structures in neutrals and charged aerosol particles as observed during the ECOMA/MASS rocket campaign, Annales Geophysicae, 27, 1449–1456, 2009.

Stroud, W., Nordberg, W., Bandeen, W., Bartman, F., and Titus, P.: Rocket-grenade measurements of temperatures and winds in the mesosphere over Churchill, Canada, Journal of Geophysical Research, 65, 2307–2323, 1960.

Thomas, G. and Olivero, J.: Noctilucent clouds as possible indicators of global change in the mesosphere, Advances in Space Research, 28, 937–946, 2001.

Thomas, G. E., Olivero, J. J., Jensen, E. J., Schroeder, W., and Toon, O. B.: Relation between increasing methane and the presence of ice clouds at the mesopause, Nature, 338, 490, 1989.

Tomsic, A.: Collisions between water clusters and surfaces, Ph.D. thesis, Göteborg University, 2001.

Tomsic, A., Marković, N., and Pettersson, J. B.: Direct scattering and trapping–desorption of large water clusters from graphite, Chemical Physics Letters, 329, 200 – 206, doi: http://dx.doi.org/10.1016/S0009-2614(00)01002-2, 2000.

Tomsic, A., Andersson, P. U., Markovic, N., Piskorz, W., Svanberg, M., and Pettersson, J. B. C.: Molecular dynamics simulations of cluster-surface collisions: Emission of large fragments, The Journal of Chemical Physics, 115, 10 509–10 517, doi: http://dx.doi.org/10.1063/1.1413740, 2001.

Tomsic, A., Schröder, H., Kompa, K.-L., and Gebhardt, C. R.: Impact dynamics of molecular clusters on surfaces: Fragmentation patterns and anisotropic effects, The Journal of Chemical Physics, 119, 6314–6323, doi: http://dx.doi.org/10.1063/1.1603213, 2003.

Varney, R. H., Kelley, M. C., Nicolls, M. J., Heinselman, C. J., and Collins, R. L.: The electron density dependence of polar mesospheric summer echoes, Journal of Atmospheric and Solar-Terrestrial Physics, 73, 2153–2165, 2011.

Voigt, C., Schlager, H., Luo, B., Dörnbrack, A., Roiger, A., Stock, P., Curtius, J., Vössing, H., Borrmann, S., Davies, S., et al.: Nitric acid trihydrate (NAT) formation at low NAT supersaturation in polar stratospheric clouds (PSCs), Atmospheric chemistry and physics, 5, 1371–1380, 2005.

Von Cossart, G., Fiedler, J., and Von Zahn, U.: Size distributions of NLC particles as determined from 3-color observations of NLC by ground-based lidar, Geophysical Research Letters, 26, 1513–1516, 1999.

Von Zahn, U. and Berger, U.: Persistent ice cloud in the midsummer upper mesosphere at high latitudes: Three-dimensional modeling and cloud interactions with ambient water vapor, Journal of Geophysical Research: Atmospheres, 108, 2003.

Von Zahn, U., Von Cossart, G., Fiedler, J., Fricke, K., Nelke, G., Baumgarten, G., Rees, D., Hauchecorne, A., and Adolfsen, K.: The ALOMAR Rayleigh/Mie/Raman lidar: objectives, configuration, and performance, Annales Geophysicae, 18, 815–833, 2000.

Vostrikov, A. and Dubov, D. Y.: Surface induced ionization of neutral water clusters, Zeitschrift für Physik D Atoms, Molecules and Clusters, 20, 61–63, 1991.

Wegener, A.: Die Erforschung der obersten Atmosphärenschichten, Zeitschrift für anorganische Chemie, 75, 107–131, 1912.

Woodman, R. F. and Guillen, A.: Radar observations of winds and turbulence in the stratosphere and mesosphere, Journal of the Atmospheric Sciences, 31, 493–505, 1974.

Zahn, U.: Are noctilucent clouds a "Miner's Canary" for global change?, EOS, Transactions American Geophysical Union, 84, 261–264, 2003.

Zasetsky, A., Petelina, S. V., and Svishchev, I.: Thermodynamics of homogeneous nucleation of ice particles in the polar summer mesosphere, Atmospheric Chemistry and Physics, 9, 965–971, 2009.

Zuppardi, G., Morsa, L., Savino, R., Sippel, M., and Schwanekamp, T.: Rarefied aerodynamic characteristics of aero-space-planes: a comparative study of two gas–surface interaction models, European Journal of Mechanics-B/Fluids, 53, 37–47, 2015.

PAPER I

Antonsen, T. and Havnes, O.: On the detection of mesospheric meteoric smoke particles embedded in noctilucent cloud particles with rocket-borne dust probes, Review of Scientific Instruments, 86, 033 305, doi: http://dx.doi.org/10.1063/1.4914394, 2015

PAPER II

Antonsen, T., Havnes, O., and Mann, I.: Estimates of the Size Distribution of Meteoric Smoke Particles From Rocket-Borne Impact Probes, Journal of Geophysical Research: Atmospheres, doi: 10.1002/2017JD027220, 2017

PAPER III

Antonsen, T., Havnes, O., and Spicher, A.: Multi-scale Measurements of Mesospheric Aerosols and Electrons During the MAXIDUSTY Campaign., Atmospheric Measurement Techniques, In Review, 2018

PAPER IV

Havnes, O., Antonsen, T., Baumgarten, G., Hartquist, T., Fredriksen, Å., Friedrich, M., and Hedin, J.: A new method to inference the size, number density, and charge of mesospheric dust from its in situ collection by the DUSTY probe., Atmospheric Measurement Techniques, In Review, 2018a

PAPER V

Havnes, O., Latteck, R., Hartquist, T. W., and Antonsen, T.: First simultaneous rocket and radar detections of rare low summer mesospheric clouds., Geophysical Research Letters, 45, 5727–5734, doi: 10.1029/2018GL078218, 2018b

Geophysical Research Letters

RESEARCH LETTER
10.1029/2018GL078218

Key Points:
- The first simultaneous radar and rocket observations of weak, low, and rare polar mesospheric summer clouds were obtained
- The majority of the dust particles appear to be neutral but with a net positive dust charge density
- Size sorting of dust must take place

Correspondence to:
O. Havnes,
ove.havnes@uit.no

Citation:
Havnes, O., Latteck, R., Hartquist, T. W., & Antonsen, T. (2018). First simultaneous rocket and radar detections of rare low summer mesospheric clouds. *Geophysical Research Letters*, *45*, 5727–5734. https://doi.org/10.1029/2018GL078218

Received 5 APR 2018
Accepted 24 MAY 2018
Accepted article online 30 MAY 2018
Published online 10 JUN 2018

First Simultaneous Rocket and Radar Detections of Rare Low Summer Mesospheric Clouds

O. Havnes[1], R. Latteck[2], T. W. Hartquist[3], and T. Antonsen[1]

[1]Institute of Physics and Technology, Arctic University of Norway, Tromsø, Norway, [2]Institute of Atmospheric Physics, Kühlungsborn, Germany, [3]School of Physics and Astronomy, University of Leeds, Leeds, UK

Abstract On 30 June 2016 a layer of dust, possibly meteoric smoke particles (MSPs), was observed with a rocket borne probe at 69.29°N, 16.02°E and altitudes of ~74 km where patchy thin cloud layers, detected with the Middle Atmosphere Alomar Radar System, were present. The rocket traversed a layer with a net positive dust charge density of ~10^7 unit charges per cubic meters and a number density of neutral dust particles with sizes ≥4 nm of ~10^8 m^{-3}. The positive charge density may require that elements that lower the photoelectric work function coat MSPs. The presence of this relatively large dust is consistent with smaller MSPs being swept out of the low mesospheric cloud region during the summer, while larger MSPs remain where their fall velocities equals the circulation updraught velocities. Large MSPs initially embedded in icy particles that subsequently sublimate may also fall until their fall velocities match the updraught velocities.

Plain Language Summary A rocket and radar campaign was conducted in the summer of 2016 to investigate the clouds in the Earth's polar middle atmosphere and the role of meteoric smoke particles. They are produced by meteorites entering the atmosphere at high velocities, where they are heated by friction and ablate. We lack knowledge of the cloud transition phases from winter to summer conditions in late May and back in late August. Recent radar observations show that contrary to the belief a few years back, weak and low clouds are not totally absent in the summer season. One of the rockets flew through a very weak and low cloud, which also was observed by radar. The probability for this to happen is very low. Analysis shows that the cloud consists of 4- to 5-nm-sized meteoric smoke particles of number density a few times 10^8 particles m^{-3} with a low positive dust charge density of ~10^7 m^{-3}. Our findings are consistent with size sorting being active and important in the low cloud region especially during the transition phases. The positive charge density apparently requires that the photoelectric properties of the smoke particles are affected by coating with or absorption of gases.

1. Introduction

The various clouds in the Earth's mesosphere have traditionally been classified as either summer clouds or winter clouds. With clouds we mean (mesospheric) dust clouds. The only visually observable clouds are the noctilucent clouds at altitudes of ~80 to ~90 km. They consist of icy particles with sizes up to ~100 nm (Von Cossart et al., 1999). Other clouds that are detected with radars are called polar mesospheric summer echoes (PMSEs; Ecklund & Balsley, 1981) and polar mesospheric winter echoes (PMWEs; Czechowsky et al., 1979). Mesospheric radar echoes, probably formed by turbulence linked to Kelvin-Helmholtz instabilities, are observed at sites close to the equator (Lehmacher et al., 2007).

The NLC/PMSE season starts when the mesopause temperature changes from a winter temperature around 200–220 K to a summer temperature as low as 110–130 K (Lübken, 1999; Von Zahn & Meyer, 1989). The change arises from seasonal variations in the global atmospheric circulation pattern, with the onset of a polar updraught and associated adiabatic cooling. Water vapor then condenses, most likely on meteoric smoke particles (MSPs) (Hervig et al., 2012; Rapp & Thomas, 2006; Rosinski & Snow, 1961).

The PMWEs are much weaker than the PMSEs and occur less frequently. Observed with standard MST radars they disappear in late May and reappear at the beginning of September (Zeller et al., 2006). Since 2011 a new MST radar MAARSY has been in operation at Andøya Rocket Range, Norway. MAARSY has 20 times the power and ~half the beam width of the ALOMAR Wind radar (ALWIN) it replaced (Latteck et al., 2012). The MAARSY observations give significantly different statistics for the PMWEs. One difference is that although the PMWEs become rarer toward the end of the standard PMWE season in May, weak radar scattering layers are occasionally observed with MAARSY during the summer months, at altitudes well below the main NLC/PMSE altitudes (Latteck & Strelnikova, 2015). The temperatures at these lower altitudes are high enough to remove icy particles.

In the following we will call these weak summer echoes rare low summer echoes (RLSEs). This to emphasize that they are different from the much stronger NLC/PMSE, which in summer are nearly always present above the RLSE heights, and further that they differ from the PMWE by being weaker with a much lower occurrence frequency. If dust particles are present in and active in creating the PMWEs, and also the RLSEs, they must be nonvolatile and differ from the icy particles of the NLC/PMSE clouds. MSPs are obvious candidates.

Support for the conjecture that MSPs are involved in creating the PMWEs comes from observations of the radar overshoot effect (Havnes, 2004). The overshoot is produced by the use of artificial periodic RF heating of electrons (Rietveld et al., 1993). The overshoot effect, first observed for NLC/PMSE clouds (Havnes et al., 2003), has also been observed for PMWEs with the European Incoherent Scatter scientific association 224-MHz radar (Belova et al., 2008; Kavanagh et al., 2006; Kero et al., 2008) and the Mobile Radar and Rocket Observatory (MORRO) 56-MHz radar (Havnes et al., 2011; La Hoz & Havnes, 2008). The weak RLSEs that are detected occasionally with MAARSY have not been detected with either of these other radars, which are collocated with the European Incoherent Scatter Heating Facility.

There is no heating facility at the MAARSY site. Consequently, the radar overshoot effect cannot be studied with MAARSY, which has left open several questions about the RLSE clouds. Are they, like the NLC/PMSE and PMWE clouds, controlled by dust particles? If so, are the RLSE particles those remnants of PMWE dust that have not been swept out of the lower mesosphere by the summer updraught? Are they related to the particles in the higher NLC/PMSE clouds? Is it possible that the NLC/PMSE icy particles, when sublimating as they sink to warmer altitudes, release a sufficient number of large MSPs that can overcome the updraught, fall below the NLC/PMSE clouds, and become important charge carriers in RLSE clouds? These are among the many questions requiring answers for an understanding of the transport and role of MSPs, from their creation in the upper mesosphere until they are deposited on the Earth's surface (Plane, 2012), to emerge.

The first step, which can be achieved with rocket borne probes, is to establish whether dust exists in RLSE clouds. However, the rarity of RLSEs presents a challenge.

Below we present, and provide an analysis of data for a RLSE layer that is the first to be detected simultaneously with radar and a rocket borne probe. In section 2 we provide the data. In section 3 we report on the analysis of the data obtained with the probe to find the RLSE dust density and dust charge density, and section 4 contains a discussion and conclusions.

2. The MAXIDUSTY Campaign

During the MXD-1 payload launch on 30 June 2016 at $09^h\,43^m\,18^s$ UT, a weak RLSE layer was detected with a DUSTY probe and the MAARSY radar. Though it is always small, the probability for RLSEs to be detectable with MAARSY is largest at the beginning of the NLC/PMSE season and falls significantly by the end of June (Latteck & Strelnikova, 2015). Usually, hardly any detectable RLSEs would be expected when MXD-1 was launched.

Disturbed magnetospheric conditions increase the electron density and the fraction of negatively charged dust and are normally required for PMWEs to be detectable with standard MST radars (Zeller et al., 2006). However, the sensitivity of MAARSY is 17 dB greater than that of ALWIN, a typical MST radar operated at Andøya until 2008. This enabled the detection of RLSEs during quiet magnetospheric, but sunlit, conditions obtained during the MXD-1 flight.

We focus on the DUSTY and MAARSY measurements in the height region below the NLC/PMSE altitudes. The MXD-1 DUSTY probe (Havnes et al., 1996, 2015) is bucket shaped with three grids and a bottom impact plate (BP). Only the currents I_{G2} to the lowest grid G2 and I_{BP} to BP are used since they, being screened from the ambient plasma, are the grids with significant dust impact currents. Figure 1a shows I_{G2} and Figure 1d I_{BP} for the upward trajectory. The main NLC/PMSE are easily identified at altitudes from approximately 81 to 86 km, but there are no clear indications of any RLSEs below these main clouds. However, zooming in on I_{BP} and I_{G2} in the region from 66 to 78 km, as shown in Figures 1b and 1c, we see small changes in the currents up to ~5 pA. This is less than ~1% of the current changes when the NLC/PMSE clouds were traversed.

Near the time t_{74}, MAARSY detected thin patchy RLSEs in the altitude region around 74 km. Figure 2 shows results for four MAARSY beams at 0°, 4°, 8°, and 12° from the vertical toward the azimuth of the rocket trajectory. All beams contained one relatively strong RLSE layer (which was not traversed by the rocket), which

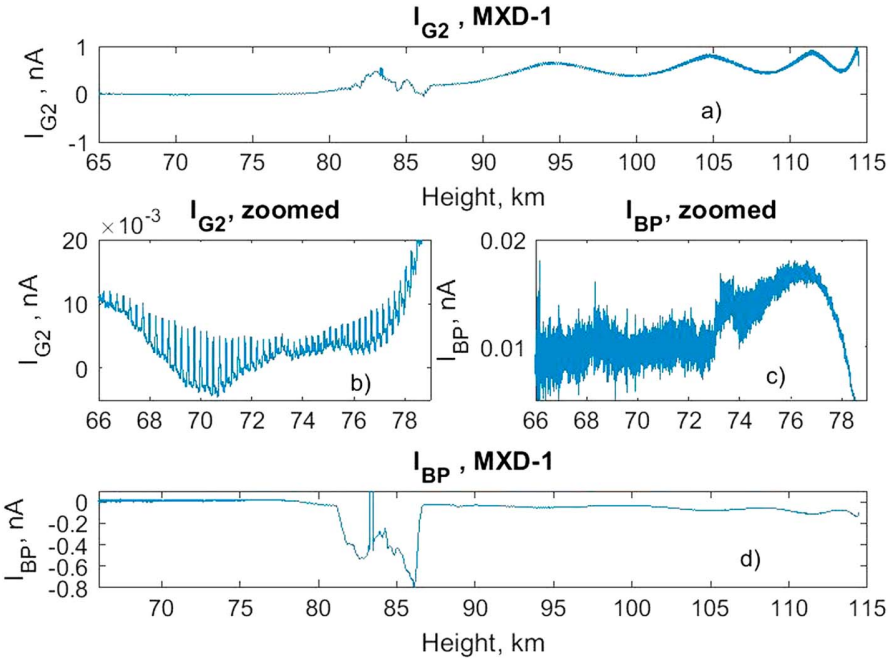

Figure 1. (a and d) The observed current I_{G2} and I_{BP} for altitudes up to apogee. (b and c) Zoom in on the altitude range of the rare low summer echo layer. The disturbance in Figures 1a and 1d at ~83 km is due to the firing of a squib for another instrument.

moved to the north-west and descended. In the MAARSY 12° beam at t_{74}, we see another weaker and more complex RLSE, which was traversed by and detected by rocket instrumentation.

The raw data shown in Figures 1 and 3 contain electronic noise and payload rotation effects. In addition to this we see in the upper heights of Figure 1a, the effect rocket precession with a period ~19.5 s.

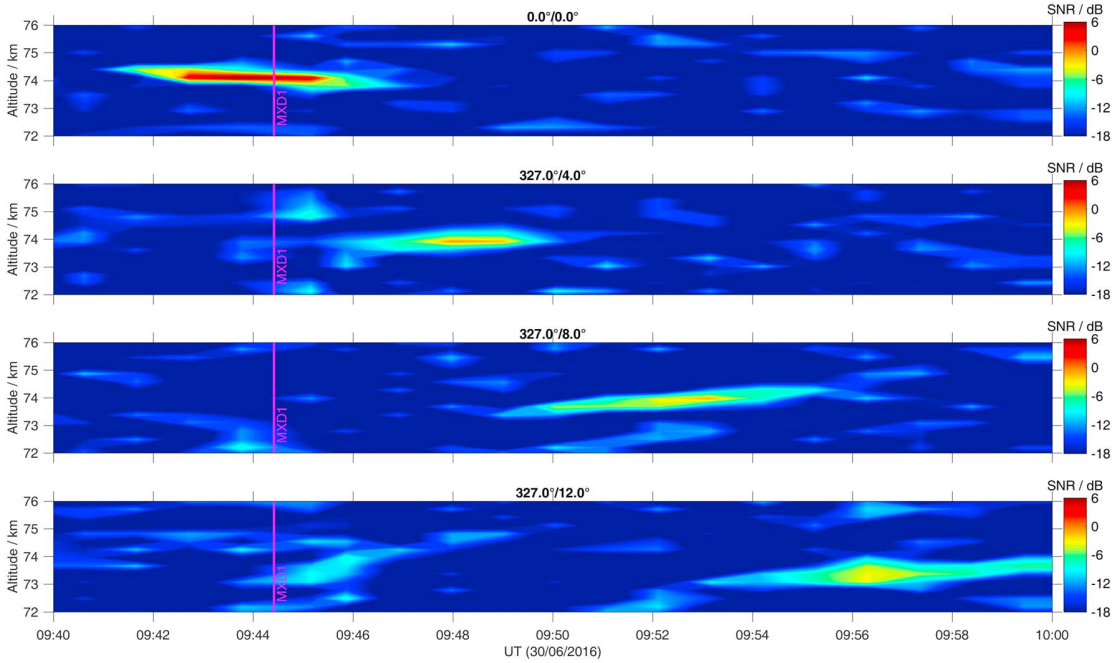

Figure 2. This figure shows results for MAARSY beams in the vertical direction and in directions toward the azimuth of the rocket trajectory at angles of 4°, 8°, and 12° from the vertical. The 12° beam was closest to the rocket trajectory, which passed 74-km height at the time $t_{74} = 09^{h}\ 44^{m}\ 25^{s}$, as indicated by the vertical line. SNR = signal-to-noise ratio.

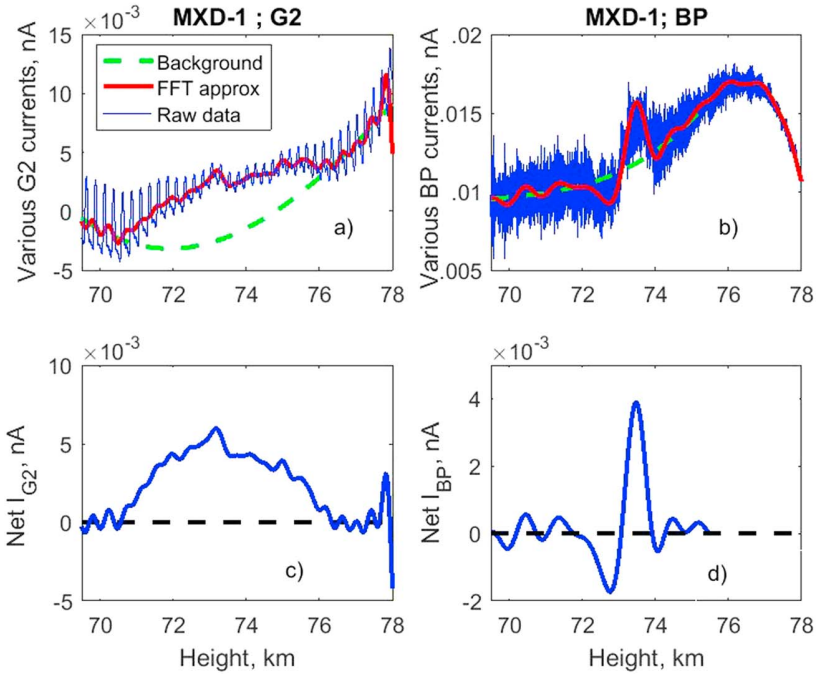

Figure 3. (a and b) The raw current to G2 and bottom impact plate (BP), respectively, the fast Fourier transform (FFT) approximations to the currents and the assumed background currents. (c and d) The net currents to G2 and BP.

Extrapolating this backward in time we find that there should be a minimum effect of the precession at height ~72 km. Without dust we would expect a mean current as shown by the background (green line) in Figure 3a. The actual observations in this height region show that there must have been dust impacts on G2 creating positive currents to it by direct deposition or by rubbing off electrons. To find the net currents to G2 and BP in the RLSE, we used fast Fourier transform (FFT) on the raw currents and an inverse FFT with a cutoff in frequency to remove payload spin effects at ~ 4.5 rps and higher frequency noise. The inverse FFT curves, representing the observations, are shown in Figures 3a and 3b as are the adopted background currents, which we found by interpolating with a third-degree polynomial fitted to altitude regions below (69–70.6 km) and above (76.2–77.5 km) the observed RLSE layer. In Figures 3c and 3d we show the final net currents I_{G2} and I_{BP} where the background has been subtracted.

3. Analysis of the RLSE Observations

The currents I_{BP} and I_{G2} measured with the DUSTY probe are due to impacts of charged and neutral dust particles. We suppose that in RLSEs, as in PMWEs, the particles are probably MSPs with charge number Z distributed between -1, 0, and +1. Photodetachment (Havnes & Kassa, 2009; Rapp, 2009; Weingartner & Draine, 2001) can at sunlit conditions cause the majority of dust particles to be neutral. Though photoionization may produce a significant number of positively charged dust (Asmus et al., 2015; Havnes et al., 1990; Rapp, 2009; Robertson et al., 2009), the number density of neutral dust particles can be much higher than that of the charged dust particles. In such cases the neutral dust particles can play a major role in determining I_{BP} and I_{G2} by rubbing off negative charge when impacting the grid wires of G2 at glancing angles (Havnes & Næsheim, 2007; Tomsic, 2001). The extraction of negative charges from G2 produces a positive current to G2 and a negative current to BP when they impact it.

A distribution of MSPs sizes can extend to sizes below 0.5 nm (Hunten et al., 1980; Rapp & Thomas, 2006). If a full MSP size distribution had been present in the RLSE cloud, DUSTY would have detected only a fraction of the ambient cloud particles because MSPs below a certain size would be swept away from the DUSTY probe by the airstream around the payload. Hedin et al. (2007) calculated the fraction of impacting dust, which were swept away from DUSTY-like probes at various atmospheric conditions. From their results one can conclude that at ~74 km, the fraction γ of particles with radii of 3, 4, and 5 nm that entered DUSTY was 0, 0.4, and 0.7,

respectively. At 74 km the real RLSE particle size distribution will probably differ substantially from the full MSP size distribution because the summer updraught will, within a few weeks after its onset, sweep away the smallest MSPs, while the larger MSPs linger at altitudes at which their fall velocities are comparable to the local updraught velocities (Havnes & Kassa, 2009). MAARSY observations (Latteck & Strelnikova, 2015, Figure 5) showing that RLSEs are found at altitudes from ~60 to ~80 km in the early phases of the NLC/PMSE season but that the lower altitude limit gradually increases with time provide evidence that this is the case. This is consistent with Rapp et al. (2010) not detecting MSPs in the lower RLSE region during the last part of the summer. We attribute this behavior to the lower regions, where fall velocities are smallest, being swept nearly clean of dust first.

Thus, for our analysis we assume that the MSPs can have three different charge states $Z = +1$, 0, and -1 (Asmus et al., 2015). We also assume that at the launch of MXD-1 all of the small particles had been swept out of the RLSE altitude region, while particles with sizes of several nanometers remained present in the upper parts of the RLSE region. Some large MSPs may also have fallen into the upper RLSE regions when sublimating NLC/PMSE particles released their embedded MSPs. In the following we will take the RLSE particle size lower limit to be large enough that the DUSTY probe registered the impact of a major fraction of the charged RLSE particles. Observations for which the dust capture efficiency is lower than 100% would mimic observations with a smaller cross section than that of the real DUSTY.

The flux of positively charged dust in front of G2 is $\Gamma(+)$, that of neutral dust is $\Gamma(0)$, and that of negatively charged dust is $\Gamma(-)$. The current I_{G2} is given by

$$I_{G2} = e\,[\Gamma(+) - \Gamma(-)]\sigma_2 + e\,[\Gamma(+) + \Gamma(0) + \Gamma(-)]\eta\sigma_{2,s} \tag{1}$$

The DUSTY probe is closed to ambient electrons and ions, which do not contribute to I_{G2} or I_{BP}. The first term on the right-hand side of equation (1) is due to positively and negatively charged dust colliding with G2. The second term describes the secondary charging effect due to high impact angle collisions of particles near the edges of the G2 grid wires rubbing off electrons and creating a positive current to G2. The G2 wire thickness and grid density is such that the G2 grid, if projected on to the bottom plate of DUSTY, covers a fraction $\sigma_2 = 0.235$ of it. Glancing impacts that produce secondary charges, occur according to our model (Havnes & Næsheim, 2007) on ~28% of the G2 cross section and $\sigma_{2,s} = 0.28\sigma_2$ is therefore the fraction of the DUSTY cross section that produces secondary charges. The secondary charge production efficiency η, which is proportional to the cross section of the impacting dust particle (see equation (6)), is the average number of unit charges that are rubbed off by dust particles impacting near the G2 wire edges.

The current I_{BP} is given by

$$I_{BP} = e\,[\Gamma(+) - \Gamma(-)](1 - \sigma_2) - e\,[\Gamma(+) + \Gamma(0) + \Gamma(-)]\eta\sigma_{2,s} \tag{2}$$

The first term on the right-hand side is due to the direct dust charge deposition on BP. The second term is caused by electrons that were rubbed off G2 being deposited as a negative current to BP.

The sum of equations (1) and (2) gives the net flux of charged dust in front of G2 as

$$\Gamma\,(\mathrm{Ch}) = \Gamma(+) - \Gamma(-) = (I_{G2} + I_{BP})/e \tag{3}$$

Considering the currents shown in Figures 3c and 3d, we see that Γ (Ch) must be positive. This rules out the ambient electron number density being large compared to the MSP number density since in such circumstances the majority of the MSPs would have $Z = -1$. We ignore this possibility and take the majority of the MSPs to be neutral and moderate fractions of MSPs to have $Z = -1$ and +1. Neglecting $\Gamma(+)$ and $\Gamma(-)$ in comparison with $\Gamma(0)$ in the last term of each of equations (1) and (2) and inserting equation (3) into equation (2) we find that

$$\Gamma(0) = [(1 - \sigma_2)\, I_{G2} - \sigma_2\, I_{BP}]/e\eta\sigma_{2,s} \tag{4}$$

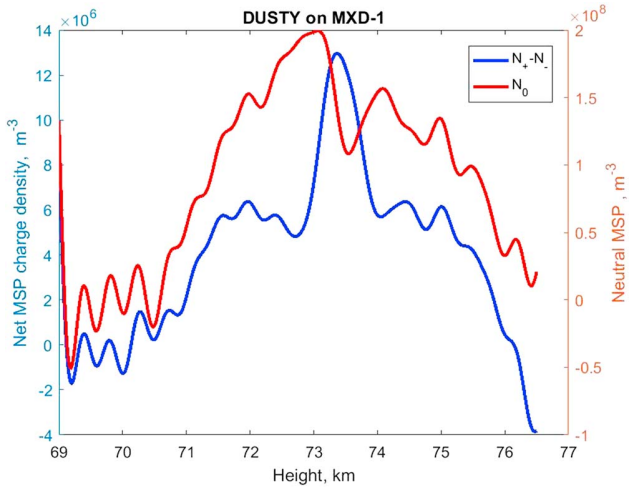

Figure 4. The dust charge density and the total number density $N(0)$ of neutral particles are shown. $N(0)$ is inversely proportional to the secondary charge production factor η. For this figure $\eta = 0.5$. MSP = meteoric smoke particle.

The secondary charge production efficiency is given by

$$\eta = \eta_{\text{ref}} \left(r_D/50\right)^2 \tag{5}$$

Here r_D is the radius of the impacting dust in nanometers. Modeling of rocket observations (Havnes & Næsheim, 2007; Kassa et al., 2012) implies that the reference value η_{ref} is in the range of ~50 to ~100 secondary unit charges produced per impact by a 50-nm-sized NLC/PMSE particle. This is several magnitudes larger than for impacts of pure ice particles (Andersson & Pettersson, 1998; Dubov & Vostrikov, 1991; Tomsic, 2001). This difference can be due to the large number of MSPs embedded in NLC/PMSE particles (Havnes & Næsheim, 2007; Hervig et al., 2012) because when a NLC/PMSE particle collides near the edge of, for example, a grid wire, it fragments and releases embedded MSPs. Pure ice particles smaller than ~7 nm attach to the impact surface and melt (Tomsic, 2001), but nonvolatile MSPs released in the collision do not. Using equation (5) we find that η may be in the range 0.3 to 1 unit charge per impact if we vary η_{ref} from 50 to 100 and the dust radius from 4 to 5 nm.

The ambient number density of the neutral dust $N(0)$ and net ambient dust charge number density, N (Ch) = $N(+) - N(-)$, are

$$N\left(X\right) = \Gamma\left(X\right)/\pi R^2 V_R \left(1-\sigma_1\right)^2 \tag{6}$$

where $X = 0$ or $X =$ Ch and $R = 0.04$ m is the DUSTY probe radius, V_R is the rocket speed (~910 m/s at altitude 74 km) and $\sigma_1 = 0.045$ is the fraction of the DUSTY cross section covered by the two screening grids G1 and G0 at the top of DUSTY. Equation (6) is based on the assumption that none of the RLSE dust particles are deflected away from the probe. Using Γ (Ch) and $\Gamma(0)$ from equations (3) and (4) with $\eta = 0.5$, we find the number densities $N(0)$ and N (Ch) throughout the cloud shown in Figure 4.

We see from a comparison between the radar observations in the 12° beam in Figure 2 and the DUST charge density in Figure 4 that the charged dust layer extends from ~71.5 to 75 km, which is roughly the height range of the radar echo when the payload is at 74-km height. The local maximum in dust charge density at slightly above 73 km also fits well with a local radar echo maximum.

Equations (3) and (4) show that N (Ch) is independent of η and that $N(0)$ is inversely proportional to η. If the effective cross section of DUSTY is smaller than the geometric cross section πR^2 by a factor γ then both N (Ch) and $N(0)$ increase by a factor $1/\gamma$.

4. Discussion and Conclusions

This paper reports the first simultaneous radar and rocket summer observations of the weak and low mesospheric dust clouds (Latteck & Strelnikova, 2015). The observed layer was found to have a net positive dust charge density ~10^7 unit charges per cubic meters and a neutral dust density ~10 times above this. We find that the dust sizes have to be of the order of 4 to 5 nm both to be detectable by the DUSTY probe and to balance the expected updraught. A rough comparison between dust fall velocity (Havnes & Kassa, 2009) and zonal mean upward vertical velocity (Crane et al., 1980) indicates that 4- to 5-nm particles are lifted by the updraught at altitudes below ~70 km but that their fall velocity may balance the updraught velocity at the altitude of the observed RLSE layer. If so, such particles accumulate there. Large MSPs released by sublimating NLC/PMSE icy particles may provide a source of particles in RLSE layers above about 70 km but should not fall much lower.

As mentioned above, the results of Hedin et al. (2007) indicate that at ~74 km all particles with sizes less than ~3 nm would have been deflected away from DUSTY by the airstream around the payload. However, for the particles that updraughts should leave to remain at ~74 km, γ is in the range of 0.4 to 0.7 indicating that the number densities in Figure 4 might be a factor of about 2 too small.

Since many particles in the RLSE layer are charged positively, photodetachment and photoionization must be important. This is consistent with the sunlit conditions during the MXD-1 flight and the finding of Havnes

et al. (2011) that photodetachment was the dominant mechanism returning the dust charges back to equilibrium in PMWE overshoot experiments.

For the photoionization to be effective, the dust work function has to be low. Havnes et al. (1990) suggested that a thin coating of other elements, or trace contaminations on NLC/PMSE dust particles, could lower the work function, as what happens on other substances. For example, Na and NH_3, when codeposited on thin films, result in a work function of only 0.9 eV (Qiu et al., 1989). Small dust particles can also have a much lower work function than the bulk material (Burtscher et al., 1984; Schmidt-Ott et al., 1980). The relevant observational breakthrough is due to Robertson et al. (2014) who, using a new dust mass spectrometer MASS (Knappmiller et al., 2008) launched in October 2011, found coexisting small positive and negative MSPs at altitudes from 60 to 70 km. The possibility that coatings reduce the work function of mesospheric NLC/PMSE particles had previously been discarded with respect to Na contamination because there is not enough contaminating material (Vondrak et al., 2006). However, our RLSE has a total particle surface area per atmospheric volume that is more than 2 orders of magnitude smaller than that in a moderately strong NLC/PMSE cloud, which may lead to a much more complete surface coating and a stronger contamination in the RLSE clouds.

In summary, we find that the following issues are raised by our observations:

1. Size sorting should occur when the updraught starts at the beginning of the summer NLC/PMSE season. How effective is this for MSPs and at what altitudes, as functions of time from the onset of the updraught, are the various particles deposited?
2. The charged particles in the RLSE that we observed are mainly positively charged, which we attribute to a comparatively low electron density and efficient photodetachment and photoionization. In order to gain further insight into RLSE formation, one should aim to launch probes early in the NLC/PMSE season through RLSEs, which are much more common then. We predict that normally a net positive dust charge density will be found in RLSEs when quiet magnetospheric conditions obtain since then the electron density will be low.
3. During high magnetospheric activity the electron density should normally be larger and in such a case we would expect the net dust charge density in a RLSE to be negative.
4. There should be intermediate conditions for which the net dust charge density is small. In such cases we would expect the radar backscatter on RLSEs to be particularly weak. In a plot of RLSE radar strength against magnetospheric activity a local minimum in RLSE strength and occurrence rate may be found between extremely quiet activity and strong activity.

Acknowledgments
The rocket campaign and the construction of the rocket instrumentation was supported by grants from the Norwegian Space Centre (VIT.04.14.7; VIT.02.14.1; VIT.03.15.7; VIT.03.16.7), the Research Council of Norway (240065), and by the Arctic University of Norway. Rocket and radar data for replication of results are available through the UiT Open Research Repository through the DOI https://doi.org/10.18710/PRJW7B.

References

Andersson, P. U., & Pettersson, J. B. (1998). Water cluster collisions with graphite surfaces: Angular-resolved emission of large cluster ions. *The Journal of Physical Chemistry B*, *102*(38), 7428–7433. https://doi.org/10.1021/jp981889x

Asmus, H., Robertson, S., Dickson, S., Friedrich, M., & Megner, L. (2015). Charge balance for the mesosphere with meteoric dust particles. *Journal of Atmospheric and Solar-Terrestrial Physics*, *127*, 137–149. https://doi.org/10.1016/j.jastp.2014.07.010

Belova, E., Smirnova, M., Rietveld, M. T., Isham, B., Kirkwood, S., & Sergienko, T. (2008). First observation of the overshoot effect for polar mesosphere winter echoes during radiowave electron temperature modulation. *Geophysical Research Letters*, *35*, L03110. https://doi.org/10.1029/2007GL032457

Burtscher, H., Schmidt-Ott, A., & Siegmann, H. C. (1984). Photoelectron yield of small silver and gold particles suspended in gas up to a photon energy of 10 eV. *Zeitschrift fur Physik B: Condensed Matter*, *56*(3), 197–199. https://doi.org/10.1007/BF01304172

Crane, A. J., Haigh, J. D., Pyle, J. A., & Rogers, C. F. (1980). Mean meridional circulations of the stratosphere and mesosphere. *Pure and Applied Geophysics*, *118*(1), 307–328. https://doi.org/10.1007/BF01586456

Czechowsky, P., Rüster, R., & Schmidt, G. (1979). Variations of mesospheric structures in different seasons. *Geophysical Research Letters*, *6*(6), 459–462. https://doi.org/10.1029/GL006i006p00459

Dubov, D. Y., & Vostrikov, A. A. (1991). Collision induced electrification of large water clusters. *Journal of Aerosol Science*, *22*, S245–S248. https://doi.org/10.1016/S0021-8502(05)80081-3

Ecklund, W. L., & Balsley, B. B. (1981). Long-term observations of the Arctic mesosphere with the MST radar at poker flat, Alaska. *Journal of Geophysical Research*, *86*(A9), 7775–7780. https://doi.org/10.1029/JA086iA09p07775

Havnes, O. (2004). Polar mesospheric summer echoes (PMSE) overshoot effect due to cycling of artificial electron heating. *Journal of Geophysical Research*, *109*, A02309. https://doi.org/10.1029/2003JA010159

Havnes, O., Antonsen, T., Hartquist, T. W., Fredriksen, Å., & Plane, J. M. C. (2015). The Tromsø programme of in situ and sample return studies of mesospheric nanoparticles. *Journal of Atmospheric and Solar-Terrestrial Physics*, *127*, 129–136. https://doi.org/10.1016/j.jastp.2014.09.010

Havnes, O., de Angelis, U., Bingham, R., Goertz, C. K., Morfill, G. E., & Tsytovich, V. (1990). On the role of dust in the summer mesopause. *Journal of Atmospheric and Terrestrial Physics*, *52*, 637.

Havnes, O., & Kassa, M. (2009). On the sizes and observable effects of dust particles in polar mesospheric winter echoes. *Journal of Geophysical Research*, *114*, D09209. https://doi.org/10.1029/2008JD011276

Havnes, O., La Hoz, C., Næsheim, L. I., & Rietveld, M. T. (2003). First observations of the PMSE overshoot effect and its use for investigating the conditions in the summer mesosphere. *Geophysical Research Letters*, *30*(23), 2229. https://doi.org/10.1029/2003GL018429

Havnes, O., La Hoz, C., Rietveld, M. T., Kassa, M., Baroni, G., & Biebricher, A. (2011). Dust charging and density conditions deduced from observations of PMWE modulated by artificial electron heating. *Journal of Geophysical Research*, *116*, D24203. https://doi.org/10.1029/2011JD016411

Havnes, O., & Næsheim, L. I. (2007). On the secondary charging effects and structure of mesospheric dust particles impacting on rocket probes. *Annales Geophysicae*, *25*, 623–637. https://doi.org/10.5194/angeo-25-623-2007

Havnes, O., Trøim, J., Blix, T., Mortensen, W., Næsheim, L. I., Thrane, E., & Tønnesen, T. (1996). First detection of charged dust particles in the Earth's mesosphere. *Journal of Geophysical Research*, *101*(A5), 10,839–10,847. https://doi.org/10.1029/96JA00003

Hedin, J., Gumbel, J., & Rapp, M. (2007). On the efficiency of rocket-borne particle detection in the mesosphere. *Atmospheric Chemistry and Physics*, *7*(14), 3701–3711. https://doi.org/10.5194/acp-7-3701-2007

Hervig, M. E., Deaver, L. E., Bardeen, C. G., Russell, J. M. III, Bailey, S. M., & Gordley, L. L. (2012). The content and composition of meteoric smoke in mesospheric ice particles from SOFIE observations. *Journal of Atmospheric and Solar-Terrestrial Physics*, *84-85*, 1–6. https://doi.org/10.1016/j.jastp.2012.04.005

Hunten, D. M., Turco, R. P., & Toon, O. B. (1980). Smoke and dust particles of meteoric origin in the mesosphere and stratosphere. *Journal of the Atmospheric Sciences*, *37*(6), 1342–1357. https://doi.org/10.1175/1520-0469(1980)037%3C1342:SADPOM%3E2.0.CO;2

Kassa, M., Rapp, M., Hartquist, T. W., & Havnes, O. (2012, March). Secondary charging effects due to icy dust particle impacts on rocket payloads. *Annales Geophysicae*, *30*(3), 433–439. https://doi.org/10.5194/angeo-30-433-2012

Kavanagh, A. J., Honary, F., Rietveld, M. T., & Senior, A. (2006). First observations of the artificial modulation of polar mesospheric winter echoes. *Geophysical Research Letters*, *33*, L19801. https://doi.org/10.1029/2006GL027565

Kero, A., Enell, C. F., Kavanagh, A. J., Vierinen, J., Virtanen, I., & Turunen, E. (2008). Could negative ion production explain the polar mesosphere winter echo (PMWE) modulation in active HF heating experiments? *Geophysical Research Letters*, *35*, L23102. https://doi.org/10.1029/2008GL035798

Knappmiller, S., Robertson, S., Sternovsky, Z., & Friedrich, M. (2008). A rocket-borne mass analyzer for charged aerosol particles in the mesosphere. *Review of Scientific Instruments*, *79*(10), 104502. https://doi.org/10.1063/1.2999580

La Hoz, C., & Havnes, O. (2008). Artificial modification of polar mesospheric winter echoes with an RF heater: Do charged dust particles play an active role? *Journal of Geophysical Research*, *113*, D19205. https://doi.org/10.1029/2008JD010460

Latteck, R., Singer, W., Rapp, M., Vandepeer, B., Renkwitz, T., Zecha, M., & Stober, G. (2012). MAARSY: The new MST radar on Andøya—System description and first results. *Radio Science*, *47*, RS1006. https://doi.org/10.1029/2011RS004775

Latteck, R., & Strelnikova, I. (2015). Extended observations of polar mesosphere winter echoes over Andøya (69°N) using MAARSY. *Journal of Geophysical Research: Atmospheres*, *120*, 8216–8226. https://doi.org/10.1002/2015JD023291

Lehmacher, G. A., Guo, L., Kudeki, E., Reyes, P. M., Akgiray, A., & Chau, J. L. (2007). High-resolution observations of mesospheric layers with the Jicamarca VHF radar. *Advances in Space Research*, *40*(6), 734–743. https://doi.org/10.1016/j.asr.2007.05.059

Lübken, F. J. (1999). Thermal structure of the Arctic summer mesosphere. *Journal of Geophysical Research*, *104*(D22), 27,803–27,810. https://doi.org/10.1029/1999JD900076

Plane, J. M. C. (2012). Cosmic dust in the Earth's atmosphere. *Chemical Society Reviews*, *41*(19), 6507–6518. https://doi.org/10.1039/C2CS35132C

Qiu, S. L., Lin, C. L., Jiang, L. Q., & Strongin, M. (1989). Photoemission studies of the metal-nonmetal transition of sodium on solid ammonia. *Physical Review B*, *39*(3), 1958–1961. https://doi.org/10.1103/PhysRevB.39.1958

Rapp, M. (2009). Charging of mesospheric aerosol particles: The role of photodetachment and photoionization from meteoric smoke and ice particles. *Annales Geophysicae*, *27*(6), 2417–2422. https://doi.org/10.5194/angeo-27-2417-2009

Rapp, M., Strelnikova, I., Strelnikov, B., Hoffmann, P., Friedrich, M., Gumbel, J., et al. (2010). Rocket-borne in situ measurements of meteor smoke: Charging properties and implications for seasonal variation. *Journal of Geophysical Research*, *115*, D00I16. https://doi.org/10.1029/2009JD012725

Rapp, M., & Thomas, G. E. (2006). Modeling the microphysics of mesospheric ice particles: Assessment of current capabilities and basic sensitivities. *Journal of Atmospheric and Solar-Terrestrial Physics*, *68*(7), 715–744. https://doi.org/10.1016/j.jastp.2005.10.015

Rietveld, M. T., Kohl, H., Kopka, H., & Stubbe, P. (1993). Introduction to ionospheric heating at Tromsø—I. Experimental overview. *Journal of Atmospheric and Terrestrial Physics*, *55*(4–5), 577–599. https://doi.org/10.1016/0021-9169(93)90007-L

Robertson, S., Dickson, S., Horányi, M., Sternovsky, Z., Friedrich, M., Janches, D., et al. (2014). Detection of meteoric smoke particles in the mesosphere by a rocket-borne mass spectrometer. *Journal of Atmospheric and Solar-Terrestrial Physics*, *118*, 161–179.

Robertson, S., Horányi, M., Knappmiller, S., Sternovsky, Z., Holzworth, R., Shimogawa, M., et al. (2009). Mass analysis of charged aerosol particles in NLC and PMSE during the ECOMA/MASS campaign. *Annales Geophysicae*, *27*, 1213–1232. https://doi.org/10.5194/angeo-27-1213-2009

Rosinski, J., & Snow, R. H. (1961). Secondary particulate matter from meteor vapors. *Journal of Meteorology*, *18*(6), 736–745. https://doi.org/10.1175/1520-0469(1961)018%3C0736:SPMFMV%3E2.0.CO;2

Schmidt-Ott, A. P. H. C., Schurtenberger, P., & Siegmann, H. C. (1980). Enormous yield of photoelectrons from small particles. *Physical Review Letters*, *45*(15), 1284. https://doi.org/10.1103/PhysRevLett.45.1284

Tomsic, A. (2001). Collisions between water clusters and surfaces, PhD thesis, Gothenburg University.

Von Cossart, G., Fiedler, J., & Von Zahn, U. (1999). Size distributions of NLC particles as determined from 3-color observations of NLC by ground-based lidar. *Geophysical Research Letters*, *26*(11), 1513–1516. https://doi.org/10.1029/1999GL900226

Von Zahn, U., & Meyer, W. (1989). Mesopause temperatures in polar summer. *Journal of Geophysical Research*, *94*(D12), 14,647–14,651. https://doi.org/10.1029/JD094iD12p14647

Vondrak, T., Plane, J. M. C., & Meech, S. R. (2006). Photoemission from sodium on ice: A mechanism for positive and negative charge coexistence in the mesosphere. *The Journal of Physical Chemistry B*, *110*(9), 3860–3863. https://doi.org/10.1021/jp0571630

Weingartner, J. C., & Draine, B. T. (2001). Electron-ion recombination on grains and polycyclic aromatic hydrocarbons. *The Astrophysical Journal*, *563*(2), 842. https://doi.org/10.1086/324035–852

Zeller, O., Zecha, M., Bremer, J., Latteck, R., & Singer, W. (2006). Mean characteristics of mesosphere winter echoes at mid- and high-latitudes. *Journal of Atmospheric and Solar-Terrestrial Physics*, *68*(10), 1087–1104. https://doi.org/10.1016/j.jastp.2006.02.015

Appendices

Appendix A

Abbreviations

AMU	Atomic Mass Units
CARMA	Community Aerosol and Radiation Model for Atmospheres
DROPPS	Distribution and Role of Particles in the Polar Summer Mesosphere
DUSTY	DUSTY is not an acronym
ECOMA	Existence and Charge state Of Meteoric smoke particles in the middle Atmosphere
ICON	Identification of the COntent of Noctilucent cloud particles
IDP	Interplanetary Dust Particle input
MAARSY	Middle Atmosphere Alomar Radar System
MaCWAVE	Mountain and Convective Waves Ascending Vertically
MESS	Meteoric Smoke Sampler
MIDAS	Middle Atmosphere Dynamics and Structure
mNLP	multi-Needle Langmuir Probe
MSP	Meteoric Smoke Particles
MUDD	MUltiple Dust Detector
MXD	MAXIDUSTY
NLC	Noctilucent Clouds

OML	Orbital Motion Limited
PHOCUS	Particles, Hydrogen and Oxygen Chemistry in the Upper Summer mesosphere
PMSE	Polar Mesospheric Summer Echoes
PMWE	Polar Mesospherivc Winter Echoes
RLSE	Rare Low Summer Echoes
RGA	Residual Gas Analyser
RMR	Raman-Mie-Rayleigh (scattering; as utilized in LIDAR)
SNR	Signal-to-Noise Ratio
SOFIE	Solar Occulatation For Ice
SPID	Smoke Particle Impact Probe
UHF	Ultra High Frequency
UHV	Ultra High Vacuum
VHF	Very High Frequency
WACCM	Whole Atmosphere Comunity Climate Model